THE HONG KONG
POLYTECHNIC UNIVERSITY
香港理工大學
Pao Yue-kong Library
包玉剛圖書館

Copyright Undertaking

This thesis is protected by copyright, with all rights reserved.

By reading and using the thesis, the reader understands and agrees to the following terms:

1. The reader will abide by the rules and legal ordinances governing copyright regarding the use of the thesis.

2. The reader will use the thesis for the purpose of research or private study only and not for distribution or further reproduction or any other purpose.

3. The reader agrees to indemnify and hold the University harmless from and against any loss, damage, cost, liability or expenses arising from copyright infringement or unauthorized usage.

IMPORTANT

If you have reasons to believe that any materials in this thesis are deemed not suitable to be distributed in this form, or a copyright owner having difficulty with the material being included in our database, please contact lbsys@polyu.edu.hk providing details. The Library will look into your claim and consider taking remedial action upon receipt of the written requests.

Optical Performances of Group-10 Transition Metal Dichalcogenides Materials

WANG Xinyu

PhD

The Hong Kong Polytechnic University

2020

The Hong Kong Polytechnic University

Department of Applied Physics

OPTICAL PERFORMANCES OF GROUP-10

TRANSITION METAL DICHALCOGENIDES MATERIALS

WANG Xinyu

A thesis submitted in partial fulfillment of the requirements

for the degree of Doctor of Philosophy

August 2019

CERTIFICATE OF ORIGINALITY

I hereby declare that this thesis is my own work and that, to the best of my knowledge and belief, it reproduces no material previously published or written nor material which has been accepted for the award of any other degree or diploma, except where due acknowledgement has been made in the text.

_____ (Signed)

WANG Xinyu_____ (Name of student)

ABSTRACT

Two-dimensional (2D) layered transitional metal dichalcogenides (TMDs) materials have shown considerable potential in various optical performances. Among them, platinum disulfide (PtS_2), which is newly developed group-10 2D layered TMDs materials, offers great potential for the laser photonic applications owing to its high carrier mobility, broadly tunable natural bandgap energy, and stability. Numerous studies have been conducted to explore the performance of 2D layered nano-materials based saturable absorber (SA) for pulsed laser applications, recently. The study of pulsed laser performance based on the SA prepared by layered materials with bulk-micro sizes have gained a great attention due to the simple preparation process, low energy consumption and simple expertise. Hence, in the first part of this study, the first passively Q-switched Erbium doped fiber laser is demonstrated with an operational wavelength of 1568.8 nm by using PtS_2 microflakes SA, fabricated by a simple liquid exfoliation in N-Methyl-2-pyrrolidone (NMP) and then incorporated into polyvinyl alcohol polymer thin film. A stable Q-switched laser operation is achieved by using this PtS_2-SA within a fiber laser ring cavity. The maximum average output power is obtained as 1.1 mW, corresponding to the repetition rate of 24.6 kHz, pulse duration of 4.2 µs, and single pulse energy of 45.6 nJ.

The achievement in Q-switched application arouses my interest in further exploration on other optical potential of PtS_2. It is reported that photoluminescence (PL)

behaviour of PtS_2 still remains obscure. Inspired by other works on TMDs quantum dots (QDs), which are believed having the capability to enhance PL property compared to the bulky or layered structure owing to their quantum confinement effects, the fabrication of PtS_2 QDs suspension via a low-cost liquid exfoliation technique is demonstrated in this work. The PtS_2 QDs with an average diameter of 3.9 nm and average thickness of 2.9 nm are observed, respectively. For the first time, the PL spectra of PtS_2 QDs suspension are successfully obtained and monitored over time. The PL spectra display an excitation-dependent luminescence. The maximum emission peak is observed at 407.2 nm for the excitation wavelength of 330 nm. This PtS_2 QDs also shows a decent long-term stability.

The next part of this study moves to expand the PL research from PtS_2 to other group-10 TMDs materials, so far whose PL natures of QDs structure still remain to be revealed. In this study, 3 typical types of group-10 TMDs materials (PtS_2, PdS_2, and $PdSe_2$) QDs are fabricated via liquid exfoliation using NMP solvent. The absorption and PL spectra of these QDs solutions are studied, exhibiting excitation wavelength-dependent behavior and large stokes shifts. Furthermore, the quantum yield and decay lifetime are also investigated and analyzed. The obtained results suggest promising optical performances of group-10 TMDs materials and indicate their prospective applications in the future.

LIST OF PUBLICATIONS

Journal Publications

[1]   **X. Wang**, P. K. Cheng, C. Y. Tang, H. Long, H. Yuan, L. Zeng, S. Ma, W. Qarony, and Y. H. Tsang, "Laser Q-switching with PtS_2 microflakes saturable absorber," *Opt. Express*, vol. 26, no. 10, pp. 13055–13060, 2018.

[2]   **X. Wang**, H. Long, W. Qarony, C. Y. Tang, H. Yuan, and Y. H. Tsang, "Fabrication of luminescent PtS_2 quantum dots," *J. Lumin.*, vol. 211, pp. 227–232, 2019.

[3]   **X. Wang**, W. Qarony, P. K. Cheng, M. Ismail, and Y. H. Tsang, "Photoluminescence of group-10 transitional metal dichalcogenides (PtS_2, PdS_2, and $PdSe_2$) Quantum Dots", *RSC. Adv.*, under review.

[4]   S. Ma, H. Yuan, L. Cai, **X. Wang**, H. Long, Y. Chai, and Y. H. Tsang, "One step synthesis of $Fe_{4.4}Ni_{17.6}Se_{16}$ coupled NiSe foam as self-supported, highly efficient and durable oxygen evolution electrode," *Mater. Today Chem.*, vol. 9, pp. 133–139, 2018.

[5]   H. Long, C. Y. Tang, P. K. Cheng, **X. Wang**, W. Qarony, and Y. H. Tsang, "Ultrafast laser pulses generation by using 2D layered PtS_2 as a saturable absorber," *J. Light. Technol.*, vol. 37, no. 4, pp. 1174–1179, 2019.

[6]   H. Yuan, S. Ma, **X. Wang**, H. Long, X. Zhao, D. Yang, W. H. Lo, and Y. H. Tsang, "Ultra-high adsorption of cationic methylene blue on two dimensional titanate nanosheets," *RSC Adv.*, vol. 9, no. 11, pp. 5891-5894, 2019.

 [7]   P. K. Cheng, C. Y. Tang, **X. Wang**, S. Ma, H. Long, and Y. H. Tsang, "Passively Q-switched ytterbium-doped fiber laser based on broadband multilayer platinum ditelluride ($PtTe_2$) saturable absorber," *Sci. Rep.*, vol. 9, no. 1, pp. 10106, 2019.

Presentations in international conferences

1. **X. Wang**, P. K. Cheng, C. Y. Tang, W. Qarony, and Y. H. Tsang, (2018). "Passively Q-switched erbium doped fiber laser using PtS_2 saturable absorber", *Nanophotonics and Micro/Nano Optics International Conference* (NANOP 2018), Oct. 1-3, Rome, Italy

2. **X. Wang**, H. Long, W. Qarony, C. Y. Tang, and Y. H. Tsang, (2019) "Fabrication of luminescent PtS_2 quantum dots", *The 9th International Multidisciplinary Conference on Optofluidics* (IMCO 2019), Jun. 14-17, Hong Kong

ACKNOWLEDGEMENTS

I would like to express my appreciation to my supervisor Dr. Y. H. Tsang, for his excellent guidance and constant encouragement throughout the period of my Ph. D study. I started my Ph. D carrier from a taught master program. He shows me how to think as a researcher and stimulates my enthusiasm of doing research works. His high requirement and inspired discussions greatly contribute to improving the quality of my doctorial research.

I would also like to thank Prof. Shu Ping Lau, Prof. Jianhua Hao, Dr. Kin Hung Fung and Dr. Yang Chai for their assistance on my doctorial research.

I would like to give my thanks to my research group members Dr. Hui Long, Mr. Wayesh Qarony, Miss. Sainan Ma, Mr. Chun Yin Tang, Mr. Longhui Zeng, Mr. Mohammad Ismail, and Mr. Ping Kwong Cheng, for their help for my research. Thanks are also due to my friends and colleagues, Mr. Xin Chen, Mr. Xiaowen Bi, Mr. QingmingChen, Miss Yujiao Zhu, Mr. Shuoguo Yuan, Dr. Huiyu Yuan, Dr. Wei Lu, and Dr. Ngai Yui Chan.

My special gratitude is sent to my wife, Ms. Xueying Wang, for her immeasurable love and support.

Last but not least, I would like to thank my parents for their support on my study and life.

TABLE OF CONTENTS

LIST OF FIGURE CAPTIONS

THE HONG KONG
POLYTECHNIC UNIVERSITY
香港理工大學

DEPARTMENT OF
APPLIED PHYSICS
應用物理學系

LIST OF TABLE CAPTIONS

Chapter 1 Introduction

1.1 Motivations

In recent years, group-10 transitional metal dichalcogens (TMDs) drew substantial attentions as novel semiconducting materials due to their unique properties such as superconductivity, high carrier mobility, broad tunable band gap, and stability in the air. Advanced optoelectronics applications, for examples, photocatalyst, field-effect transistors (FET), logical junction, thermal electricity, and photodetectors have received promising improvements with the aid of group-10 TMDs materials. Increasingly, they have grown more appealing to further applications. Though several achievements have been obtained with their few-layer to monolayer structures, the fabrication techniques and properties of group-10 TMDs quantum dots (QDs) still remains to be revealed.

1.1.1 PtS$_2$ based saturable absorber for passively Q-switched laser

Attribute to the low repetition rate and corresponding high pulse energy and peak power [1], Q-switched laser is one of the most popular types of laser, which is widely being applied in laser materials processing, microfabrication, remote sensing, range finding, skin treatment, tattoos removal, pumping source for nonlinear frequency conversion devices, and medical surgery [2], [3]. Drifted by the strong commercial interests, the Q-switched laser has gained a considerable attention within the modern industry and science communities. Unlike the costly, complex, and bulkiness of active electro- or acousto- optic modulators which can be utilized within the laser

cavity to generate Q-switched laser pulses [4]. The passive Q-switching technique with saturable absorber (SA) offers a simple, low cost, compact and reliable alternative way to produce Q-switching pulses. Furthermore, the low energy consumption and lightweight properties have made it more suitable for the practical applications of some portable devices e.g. range finder.

Usually, doped crystal, e.g. Co:MALO [5], Cr:YAG [6] etc. are used for the fabrication of commercially produced passive Q-switching systems. However, these crystal-based Q-switchers require expensive crystal growth process and doping techniques [7]. Hence, simple fabrication methods with novel saturable absorber materials are quite encouraging. In the past decade, numerous studies have been carried out implementing carbon-based nano-materials e.g. graphene [8], [9], graphene oxide [10], [11], and carbon nanotube [12] SA to generate Q-switching pulses. Graphene-based SA exhibits zero or small bandgap energy, offering a broad response wavelength ranging from UV to mid-infrared. However, the weak layer absorption significantly limits the light modulation ability [7]. Recently, the research interest of graphene has been extended to other two-dimensional (2D) layered materials with nature bandgap, stronger layer absorption, and modulation depth. Black phosphorus (BP) has shown strong layer dependent bandgap energy [13], which has also been used to fabricate SA for Q-switching pulse generation [14]. TMDs compounds, a different type of 2D layered materials, have demonstrated excellent properties based on the atomic ratio [15] and d-electron number of the transition metal [16]. TMDs has the stoichiometry of MX_2. Each layer is composed of

THE HONG KONG
POLYTECHNIC UNIVERSITY
香港理工大學

DEPARTMENT OF
APPLIED PHYSICS
應用物理學系

a single plane hexagonally arranged with groups 4−10 transition metal atoms sandwiched between two of chalcogen atoms (S, Se, or Te) [7]. The demonstration of group-6 TMDs materials as SA e.g. MoS_2 [17], [18], $MoSe_2$ [19], WS_2 [20]–[22], and WSe_2 [21] for Q-switching or mode locking laser systems have also recently been achieved. These 2D materials have gained huge interest due to their unique electrical and optical properties, which can be further tailored for the laser pulse generation and according to the application needs.

The newly discovered group-10 TMDs layered materials such as platinum diselenide ($PtSe_2$) and platinum disulfide (PtS_2) have recently attracted great attention, which have been demonstrated to be capable of enabling high performance optoelectronic devices due to their high carrier mobility and broadband light absorption [23]–[25]. In a typical octahedral unit cell structure of group-10 TMD material, one transition metal atom is surrounded by 6 chalcogen atoms [26], [27]. Their potential applications have already been demonstrated in photocatalyst [23] and field-effect transistors [24], [28]. Under the ambient temperature, PtS_2 exhibits a considerable electrical conductivity of 1107 cm^2 V^{-1} s^{-1}, which is comparable to that of black phosphorus [29], [30]. PtS_2 exhibits a layer dependent tunable and indirect bandgap behavior ranging from 1.6 eV for monolayer to a bandgap of 0.25 eV for bulk materials [27]. Such a broad bandgap range of the material allows to utilize it as a SA from mid to near infrared region of the wavelength spectrum. Hence, the inherent properties of noble PtS_2 material system open up new doors to study the nonlinear absorption properties. So far, chemical vapor deposition (CVD) [27] and molecular

beam epitaxy (MBE) [23], [24] techniques have been used for fabricating few layered group-10 TMDs materials. However, the costly and complicated preparation process of CVD and MBE techniques prevent the realization of making PtS_2 films. Nevertheless, the use of micro-size bulk-structured WTe_2 has been demonstrated as a promising approach to fabricate SA in generating ultrafast mode locking pulses in a fiber laser cavity [31]. The approach has also gained a lot of attention as a cost-effective technique for mass production of bulk-like materials by crashing the materials mechanically or exfoliated with the help of ultrasound in liquid. In this study, the possibility to use the microflakes of the novel PtS_2 2D material in Q-switching laser application will be explored [31]. A low-cost ultrasound liquid exfoliation method will be employed to produce micro-size PtS_2, which is used for fabricating saturable absorber. The fabricated PtS_2 based saturable absorber will be used to study a passively Q-switched Erbium (Er)-doped fiber laser operating at 1569 nm.

1.1.2 PtS_2 quantum dots and its photoluminescent behaviour

In the past decade, layered materials have gained considerable attention in the optoelectronics materials and devices [32]–[34]. The optical and electrical properties of layered materials can be tailored by precisely controlling the size and dimension according to the applications needs, which could as a consequence significantly enhance the performance along with the expansion of their applications. Due to the excellent electrical properties and low Johnson noise of graphene after scaling down from bulk graphite to two-dimensional (2D) structure, it has become a competitive candidate for the channel of field effect transistor [32]. Similar to graphene, layered

TMDs materials such as MoS_2 or WS_2 outperform in a wide range of applications including but not limited to catalysis, energy storage, electronics devices, and bio-pharmacy [33]–[35]. Unlike the conventional transition metal sulfides such as PbS or CdS, TMD materials are arranged in 2D layered structures and their bandgaps exhibit layer-dependent property [34]. Many of the research efforts are focused on the optimization of the fabrication process of low dimension of these layered nanomaterials as it benefits in a wide range of research fields ranging from material science to the novel device applications [34], [36].

Quantum dot (QD) was explored by further reducing dimensions of 2D layered materials to ideally zero dimension. This novel structure of material exhibits strong quantum confinement and boundary effect leading to unique and excellent electrical or optical properties that exceed its few- or mono-layer counterpart [37]. For instance, carbon QDs, generally defined as carbon that smaller than twice the size of its exciton Bohr radius, resulting in quantum confinement, exhibits distinguished optical properties of tunable fluorescence emissions and up-conversion fluorescence compared to the bulky graphite or graphene sheet [38]. The QDs materials also exhibit larger transition energy in comparison to the layer structure due to quantum confinement effects that are capable to obtain enhanced photoluminescence (PL) in certain spectra [37]–[40]. QDs have played prominent roles for a wide range of novel applications including non-linear optics [41], [42], photo-catalysis [43], [44], photovoltaics [45], and bio-imaging [46]. The fabrication of quantum dots with the novel 2D materials is currently considered to be a crucial and demanding research

field due to exclusive characteristics and wide applied areas.

In the previous work, the Q-switched performance of PtS_2 has been demonstrated and motivate me to explore the other optical performances of this novel materials. It encounters a confinement that the PL signals exhibited by PtS_2 at a scale from bulk to monolayer are too weak to be detected [26]. This issue aroused our interest to further investigate its PL behaviors.

Quantum dots are reported to exhibit larger transition energy in comparison to the layer structure due to quantum confinement effects that are capable to obtain enhanced PL in certain spectra [37], [39], [40]. Inspired by quantum confinement effect, the current study is focused on the fabrication of PtS_2 QDs suspension to enhance its PL performance and obtain the emission spectra. Expensive techniques such as Chemical Vapor Transport (CVT) [26], [27] and Molecular Beam Epitaxy (MBE) [23], [24] are generally utilized to produce few-layer group-10 TMDs materials. The synthesize methods and characteristics of PtS_2 QDs are rarely reported so far. In this work, PtS_2 QDs suspension is successfully obtained by a low-cost liquid exfoliation method. The emission spectra of PtS_2 QDs are successfully confirmed and firstly demonstrated in this work. The characterizations of PtS_2 QDs and their PL behaviors reveal the potentiality of this material in the field of luminescence related applications such as imaging, light-emitting diode, or bio-sensor.

1.1.3 Typical group-10 TMDs (PtS_2, PdS_2, and $PdSe_2$) Quantum dots and their photoluminescent behaviours

Even though PtS$_2$ QDs exhibit potentials in optical applications, the PL behaviors of majority of group-10 TMDs QDs are rarely being investigated yet. Unlike to the traditional TMDs materials these advanced TMDs materials again exhibit several unique material properties, such as superconductivity, high carrier mobility, broad tunable band gap, and stability in the air [24], [26], [27], [47], [48]. The application of such materials in optoelectronic devices is also wide with remarkable performances. For instance, PtS$_2$ with (0.25 (bulk) to 1.6 eV (monolayer)) indirect band gap [26], [27] has been applied in field-effect transistor (FET) [26], and catalysis [49]. PtSe$_2$, with a tunable indirect band gap from 0 (bulk) to 1.2 eV (monolayer), has also been used in SA [50] and broadband photodetectors [51], [52]. Then electronic, optical, and catalytic properties with bandgap tunability have also been studied in PdS$_2$ under tensile strain, exhibiting semi-metallic characteristic even for the bilayer structure [53]. Furthermore, the indirect bandgap with 1.0 eV is found to appear in PdS$_2$ when it reaches monolayer thickness, whereas the metallic characteristics are exhibited for its bulk counterpart [53]. A PdS$_2$ logical junction has also recently been reported with 2.5 nm channel length and a gate voltage dependent I-V characteristic [54]. Additionally, indirect bandgap PdSe$_2$ with a bandgap of 1.31 eV has been exhibited for its monolayer structure and metallic for the bulk counterpart [47]. The applications of PdSe$_2$ based thermal electricity [55], FET [56], and photodetector [57] suggest its exceptional optoelectronics properties. In the beginning, the PtS$_2$ was anticipated and experimentally demonstrated as that the PL signal is "too weak to be detected" owing to its indirect bandgap, even for the case of its monolayer structure [27]. Nonetheless, the PL behavior of PtS$_2$ has successfully observed via

scaling down to QDs in the previous work mentioned above [58]. However, the PL behaviors of PdS_2 and $PdSe_2$ are still remained obscure. Since PdS_2 and $PdSe_2$ exhibit similar crystal structure with PtS_2, including the indirect bandgap, such group-10 TMDs materials arouse our interest for the investigation of PL performance.

In a previous study, I successfully fabricated luminescent PtS_2 QDs via low cost liquid exfoliation with water [58]. Herein, 3 typical group-10 TMDs materials (PtS_2, PdS_2, and $PdSe_2$) QDs are fabricated with the aid of similar liquid exfoliation technique, while NMP is selected as solvent for its better compatibility of surface energy as compared to the water. To my knowledge, this is the first experimental demonstration of optical characteristics of PdS_2 and $PdSe_2$ QDs, where the UV-Vis spectra, PL spectra and the decay lifetimes of PtS_2 QDs, PdS_2 QDs, and $PdSe_2$ QDs are monitored and analyzed by comparing with each other.

1.2 Thesis outline

In this study, the layered PtS_2 microflakes based saturable absorber is fabricated and its performance in q-switching laser cavity is studied. Then, the size of PtS_2 is further shrunk into QDs in order to obtain and investigate its PL property. Furthermore, the discover of this PL behavior arouse my interest to explore the other group-10 TMDs, such as PdS_2 and $PdSe_2$, QDs fabrication techniques and optical performance. For the sake of coherent understanding, the thesis is divided into five parts. A summary and an outlook follow straight after the main body.

Chapter 2 "Backgrounds, Principles, and Characterizations"

Chapter 2 reviews the general background from the beginning of the 2D materials to the advancing group-10 materials which are investigated in this study. The fundamental principles of laser Q-switching and photoluminescence are introduced for better explaining the novelties of my study in the following parts. The characterization techniques used for my study are presented in this part as well.

Chapter 3 "Q-switched Laser with PtS$_2$ microflakes saturable absorber"

Chapter 3 introduces the novel newly discovered group-10 TMDs, PtS$_2$, can be used as saturable absorber for generating Q-switched laser pulses. The achieved pulse energy is comparable to those reported Q-switched Er-doped fiber lasers by using other 2D TMDs-SA such as WS$_2$ and MoS$_2$. Moreover, the materials used for this study is microflake that can be mass produced easily and cost effectively by simple liquid exfoliation method. The study could open up a gateway to develop the micro-size PtS$_2$ nonlinear optical materials.

Chapter 4 "Fabrication of Luminescent PtS$_2$ Quantum Dots"

Chapter 4 demonstrats the first fabrication technique of PtS$_2$ QDs, that obtained via a low-cost liquid phase exfoliation method with DI water as solvent. The PL spectra of PtS$_2$ QDs are observed for the first time, while the PL signal is reported too weak to be detected for the multi- and single-layer PtS$_2$ nanosheet. The PL behaviors under 6 months was monitored confirming the long-term stability of PtS$_2$ QDs. The findings of PtS$_2$ QDs' PL behaviors indicate the promising future for luminescence

applications and the study could open up a gateway to develop other group-10 TMDs 2D materials-based QDs for a wide range of applications.

Chapter 5 "Photoluminescence of Group-10 Transitional Metal Dichalcogenides (PtS$_2$, PdS$_2$, and PdSe$_2$) Quantum Dots"

Chapter 5 profoundly describes the PL properties of group-10 TMDs materials, PtS$_2$, PdS$_2$, and PdSe$_2$ QDs have been fabricated via a low-cost liquid phase exfoliation method. The PL spectra of their QDs were observed and analyzed by comparing to each other. To our knowledge, so far this is the first demonstration of fabrication techniques and PL behaviors for PdS$_2$, and PdSe$_2$ QDs. The findings of these three typical QDs' PL behaviors indicate the promising future for luminescence applications and the study could open up a gateway to develop other 2D group-10 TMDs-based QDs for a wide range of applications.

Chapter 6 "Summary and future work"

Chapter 6 summarizes the above 5 chapters from the PtS$_2$ based saturable absorber to group-10 TMDs QDs and their PL behaviors. Additionally, this chapter also includes a brief explanation on some relevant future works.

Chapter 2 Backgrounds, Principles, and Characterizations

2.1 Backgrounds

2.1.1 Nanomaterials

Nanomaterials extensively attracted attentions of materials research field in recent years. Nanomaterial can be delineated when at least one of its dimension reaches nanometer scale, leading to many alterations in fundamental characteristics. Size-effects, exclusively observable in various nanomaterials, can give rise to several brand new features, for example, surface plasmon resonance in metal nanoparticles; quantum confinement in semiconductor nanomaterials; and superparamagnetism in magnetic nanomateirlas. Nanomaterials can be generally defined as two-dimensional (2D) materials when single dimension is confined; one-dimensional (1D) materials when two dimensions under limitations; or zero-dimensional (0D) materials for three of their dimensions are structured at nanometers scales.

2.1.2 Two-dimensional materials

Therefore, characteristics of the materials can be determined not only by the sizes, but also by the dimensions as an essential factor. Carbon materials with sp2 hybridization in Figure 1 can well illustrate such perspective by observing diverse properties in their fullerences structure in 0D form, nanotubes structure in 1D form, graphene structure in 2D form, and graphite structure in 3D form. Carbon materials
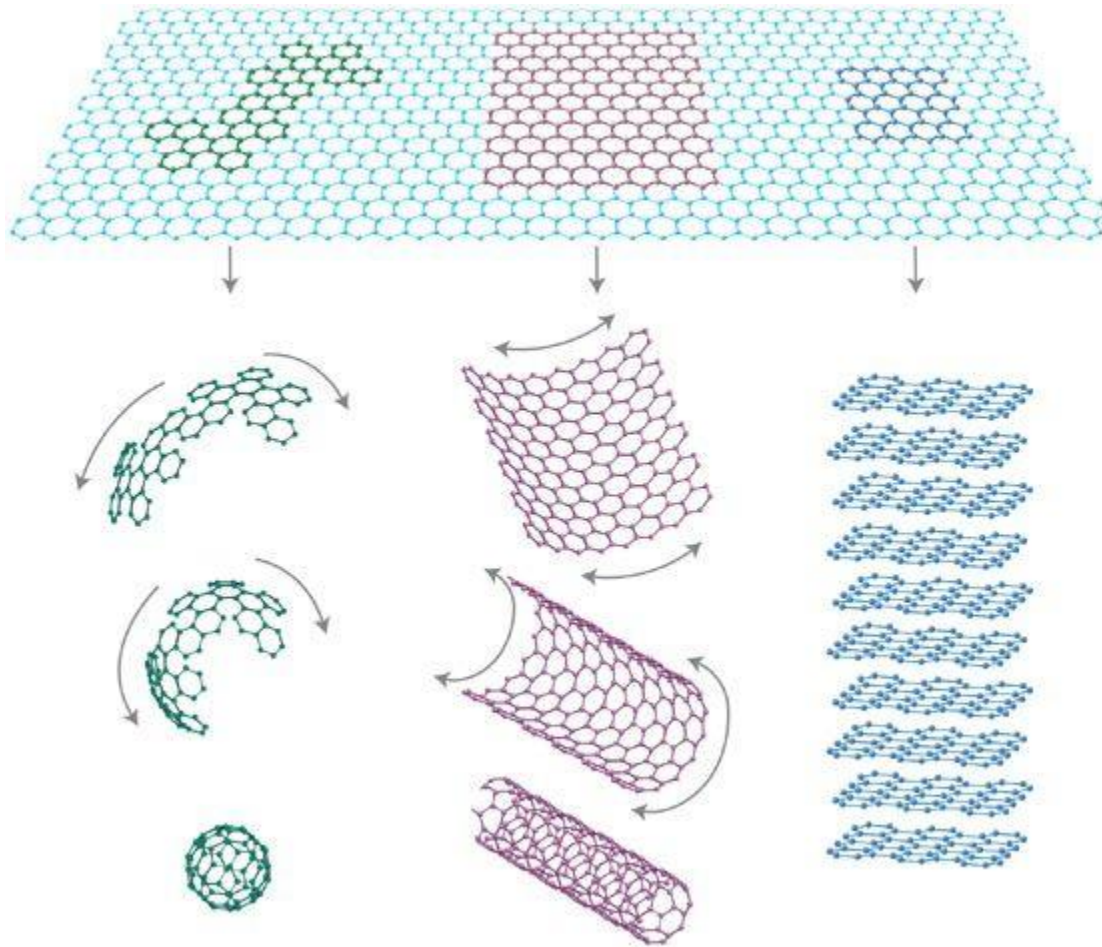
Figure 1 0D fullerenes, 1D carbon nanotubes, or 3D graphite can be constructed by using 2D graphene as standard model [32].

are generally taken as a case to study the chronicles of development of materials dimensions. Graphite was put into widespread use in 16th century for steel production, dry lubricating agent, or serving as brake lining in several devices. Allotropes of carbon were not brought to forefront until the discover of fullerences in the year of 1985 [59]. Following with fullerences, carbon nanotube, as 1D structure of graphite, was then firstly revealed in 1991 [60]. Despite the theoretical study in graphite, fullerences, or nanotubes took single layer graphite as fundamental model,

it was successfully isolated from the nature and defined as monolayer graphene until 2004 [61]. In the same year, carbon QDs, a 0D structure carbon nanoparticles in atomic scale, was firstly obtained during purification of single-walled carbon nanotubes, exhibiting strong and unique fluorescent property [62]. Begin with graphene, considerable 2D layered materials such as hBN [63], black phosphorus [13], [14], transition-metal dichalcogenides (TMDs) [64], and group-10 TMDs [24], [27], [49], [57] with distinct features are broadly discovered and developed over time. The layered structure of 2D materials promote many promised characteristics, e.g. oriented heat conduction, electric conduction, and tunable band gap, proving their attractive features in the field of fundamental materials research, and their potentials for applications in novel techniques. 2D materials receive high expectations in many prospective applications, including but not limited to support membranes, gas storage, catalysis, sensors, inert coatings, optoelectronics devices, and biomedicine.

Graphene is the first monolayer 2D material separated from the nature, displaying as a single layer graphite. Researchers endeavor to obtain single layer graphite during the past 5 decades, in order to verify the theoretical model of carbon materials consisting of tight bonding sp2 hybridization structure with single atomic thickness. Most traditional fabrication methods are failed to produce such structure in the past. The majority of researches are devoted to graphite intercalation compound in 1960s, which contains some host molecules sandwiched between graphite layers, leading to weaken the interlayers Van der Waals forces. A ductile graphite, which can extend its volume over 1,000 times by rapidly raising the temperature, was considered as

the most potential compound, ending up at 10 – 50 layers' thickness. Even with the development of fabrication techniques in the following decades, only few of cases can are able to obtain graphite with 10 layers' thickness.

Monolayer graphene holding atomic thickness and macroscopic size is attained for the first time by Andre Geim's group in the year of 2004 [65]. They applied mechanical cleavage to highly oriented pyrolytic graphite, yielding graphite flakes with an average thickness of 10 layers, and, surprisingly, single layer structure graphene as well. The monolayer characterization techniques stand equally vital comparing to the fabrication method. Even though monolayer graphene is transparent, it is still discernable when attaching to oxidized silicon substrate. Thanks to phase contrast effect, monolayer 2D material is thick enough to obstruct the light paths comparing to bare substrate. The yield of monolayer structure is yet too low to satisfy the mass production in industrial techniques, however, such cleaving method is sufficient for fundamental research supply [32]. The monolayer graphene was proved to be highly crystallized and continuous in visible scales, resulting in opening a brand new research field of 2D materials and their fabrication methods.

Graphene was successfully obtained with several advanced fabrication methods later on. Deposit hydrocarbon on the surface of appropriate metal crystal, e.g. Pt, Ir, and Ru, via CVD technique, following by the growth of graphene assisted with catalysis [66], [67]. Graphene was also reported grown on SiC substrate via graphitization techniques under ultrahigh temperature and pressure [68]. Both fabrication methods encounter limitations due to requirement of rigorous

environment and certain substrates. Self-assemble was proposed convert organic precursors into graphene via cyclodehydrogenations reaction, yielding so-called nanographenes with the largest diameter of only 3.1 nm [69]. Due to existence of many confinements, scientists never cease to pursue the simple, efficient, large-scale, and low-cost fabrication method of graphene.

Solvent-soluble graphene was achieved by using extensive graphite as starting materials following by chemical reaction [70]. The removal of accompanying coating of organic molecules unfortunately causes aggression of graphene. Finding a certain solvent may improve the dispersibility of graphene in order to avoiding further aggression. Though colloidal graphene suspension was obtained via ultrasonic exfoliation of graphite using organic solvent NMP as solvent [70], the issues of low concentration and yield still remain to be resolved.

Taking graphite oxide as starting material is considered as a promising solution to solubility issue of graphene [71]. Yet controversy remains in chemical composition of graphite oxide [72], [73], its structural composition is well known as formation of multiple graphene oxide (GO) layers stacking together. Such structure contains complex carbon network, where majority of carbon atoms attach with hydroxyl groups or play as a part of epoxide groups. The appearance of those function groups weaken the interplanar forces and affect the hydrophilia, sequentially leading to isolation of graphite with less assistance of stir and ultrasonic energies and higher yield of monolayer graphene. GO acts as a promising insulator comparing to graphene thanks to the interference of aromaticity in graphite. Recovering from GO

to graphene for the excellent conductivity is craved due to numerous demanding from advanced applications. Deoxygenation is considered as the most efficient approach to retrieve conductivity. Removing oxygen atoms essentially plays a role in recovering the aromatic carbon network, resulting in improvement of conductivity of GO. Many progressive achievements promoted the conductivity of exfoliated graphene in recent years via such reduction approach [74]. The reduced GO thin film drew significant attentions as a better electrode material for solar cell comparing to metal oxides, owing to its high transparency and conductivity [75], [76].

2.1.3 The development of Transition-metal dichalcogenides

A sort of 2D materials exhibit wide spectrum comparing to graphene. The band gap structure of such materials dramatically differ when scaling down close to monolayer comparing to their thicker counterparts [77]. These so-called transition metal dichalcogenides (TMDs) showed many prospective optical and electrical properties outmatching graphene. They were also regarded as advanced 2D semiconductor materials attracting attentions from research community as shown in Figure 2 and development of optoelectronics applications [78].

TMDs materials gather of over 40 species of 2D layered materials structured in MX_2 formula, where M represents group 4 to group 7 transition metals in general, X symbolizes one type of chalcogen, such as S, Se, or Te. Common TMDs materials, e.g. MoS_2, WS_2, or WTe_2, exhibit semiconducting characteristics thanks to their band gap which absence in graphene. Bulky TMDs materials are studied for many decades for their prospect of representing compounds with various electronic

structure in specific formulation. The bulky TMDs formed by piling up several single layers via Van der Waals force. Each single layer TMDs material structured M and X atomics by strong atomic bonding in a specific geometric configuration, where M atom is sandwiched between two X atoms. The layered structure allows external energies, such as exfoliation or CVD, to detach it into monolayer. The decreasing of
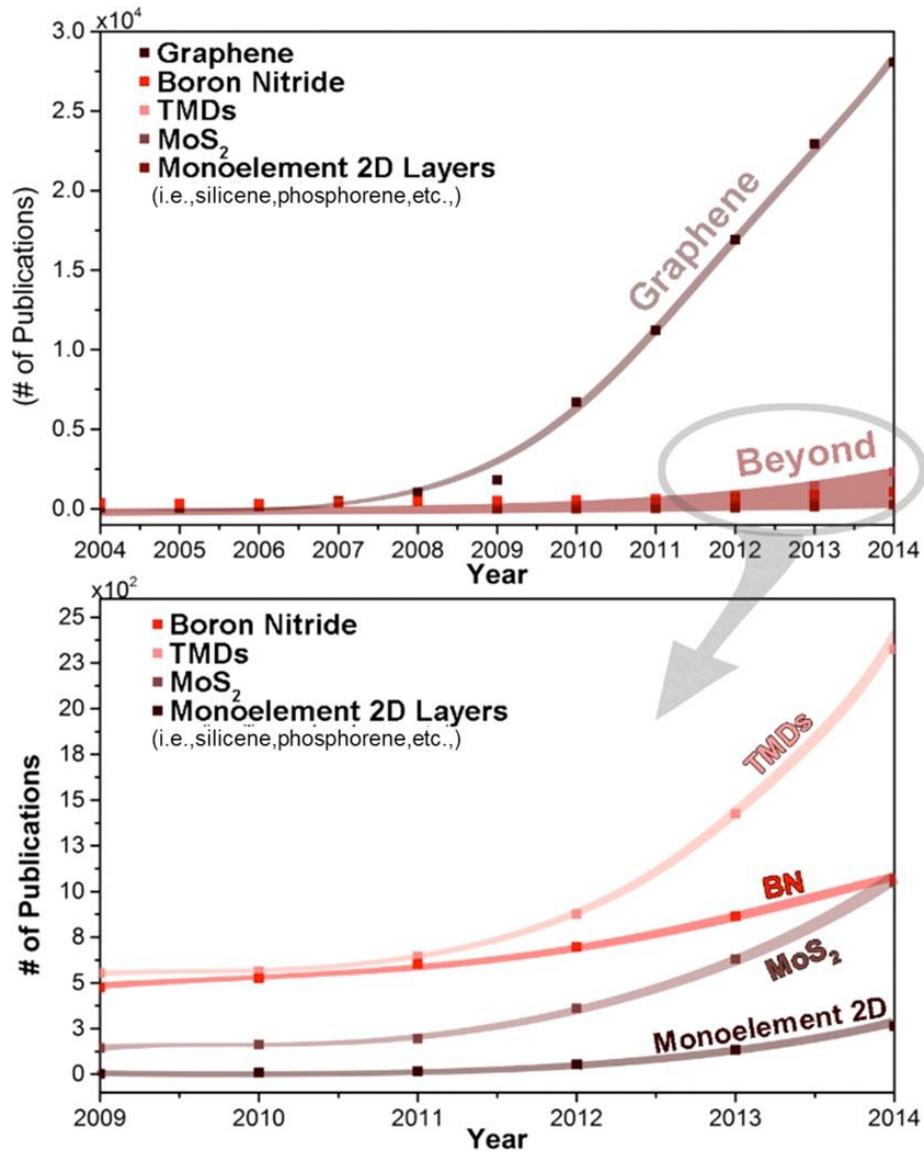
Figure 2 Publication trends in 2D materials beyond graphene [79].

thickness confines charge carriers in directions of 2D spaces, giving rise to many unique properties due to lack of interactions and reactions in z-direction. Comparing to their bulky counterparts, monolayer 2D materials thus exhibit some distinguishable characteristics bringing promising future to widespread applications, for example, optoelectronic devices, catalysis, and biomedicine.

A lot of issues forthcoming remain to be resolved in order to reveal the potentials of 2D layered TMDs materials. Devoting to the fundamental experiments and theories of their electronic structure and oscillation characteristics, researchers discovered novel properties and opportunity in realistic applications. Fabrication of TMDs in mass production with high quality and scalability has become a popular interest of research. Developing the fabrication methods by tailoring them to specific applications drew considerable attentions in recent years.

The mainstreams of fabrication techniques of 2D TMDs materials are including wet-chemical reactions, vapor-chemical reactions, and liquid exfoliations [16], [80], [81]. Vapor deposition is the most extensive technique for growth of TMDs materials due to its high scalability and precise control of morphology. The vaporized precursors contain the metal atoms, e.g. WO_3, MoO_3, or $(NH_4)_2MoS_4$ [81], contacting with chalcogen elements on the surface of substrate. The 2D TMDs materials emerge when vapor-solid phases reaction take place. Confined by growth condition of vaporized reactants, such approach produce 2D TMDs with flaws in uniformity and morphologies. Aiming at resolving the issues mentioned above, vapor phase chalcogen, such as hydrogen sulfide, was adopted as reactant substituting solid

phase chalcogen [82]. Besides, thickness controllable 2D MoS_2 nanocrystal was synthesized in centimeter scale via sulfuration of molybdenum chloride [83]. The scalability is enhanced later by precisely controlling the pressure balance of vaporized MoS_2 [84]. Large-scale 2D TMDs production with morphology control is successfully achieved by implementing reactions between vapor phase chalcogen
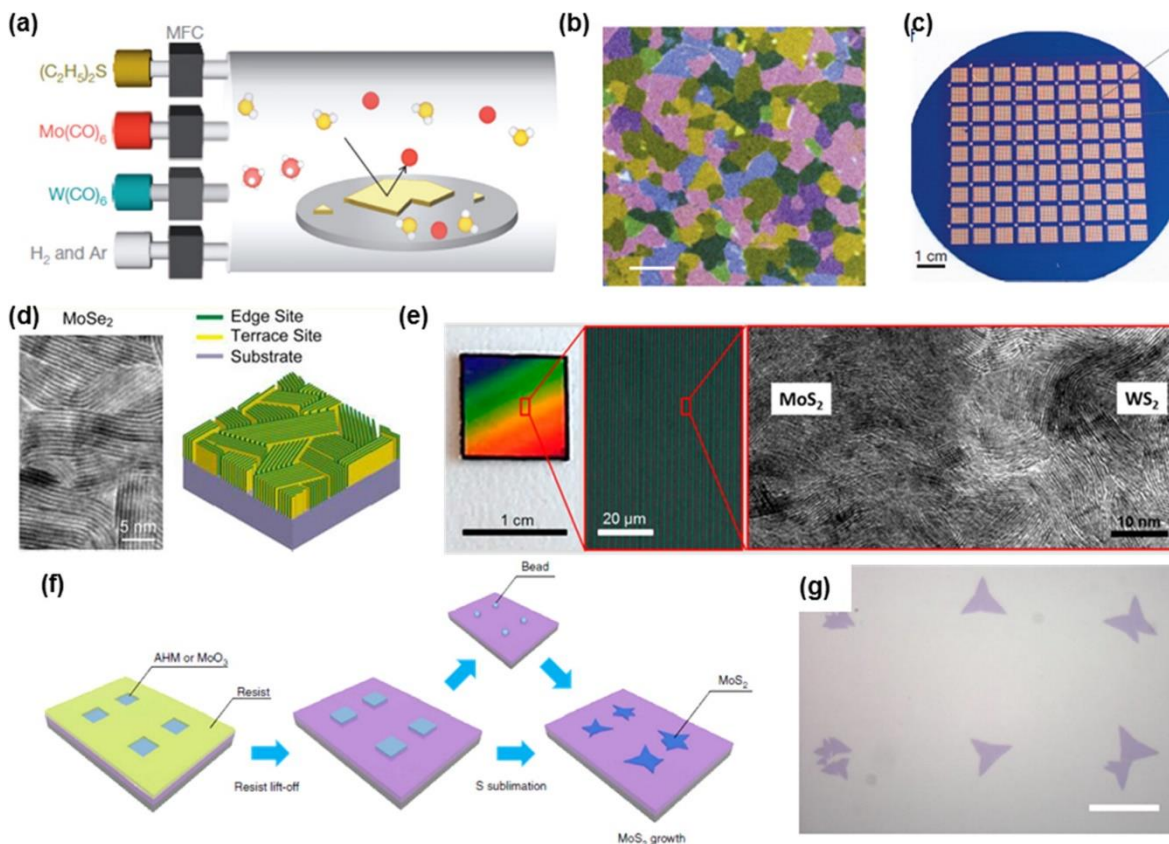
Figure 3 Fabrication techniques of various 2D TMDs [79]. (a) illustration of MOCVD technique. (b) Continuity of 2D monolayer MoS_2 shown by TEM image. (c) photograph of 2D monolayer MoS_2 grown upon 4-inches wafer. (d) Vertically oriented growth of 2D $MoSe_2$. (e) Large-scale fabrication of Vertically oriented growth of 2D MoS_2/WS_2 (f) Schematics of CVD techniques of and (g) 2D MoS_2 grown at selective position.

and substrate deposited with metals [85]–[92]. The seed-promoting molecule, such as perylene-3,4,9,10-tetracarboxylic acid tetra-potassium salt (PTAS), is proved to benefit uniformity enhancement of the growth of 2D TMDs. Thanks to the favorable solubility of PTAS, the seed solution is able to homogeneously scatter on the hydrophilic surface of substrate [93], [94].

Molecular beam epitaxy (MBE) is favored in growing 2D TMDs materials with high quality and electronic scale precision thanks to the in situ characterizations during the fabrication process [95]–[100]. Recently, large-scale and monolayer 2D MoS_2 is continuously grown on the surface of 100 mm wafer via metal-organic CVD based on vapor phase precursors as shown in Figure 3(a) to 3(c) [101]–[103]. Growth orientation, number of layers, chemical compositions, and positions are the essential keys to the controllable growth. Vertically and horizontally orientated 2D layered structure are capable growing controllably based on the thickness of metallic seed layers via thermal evaporation CVD technique, shown in Figure 3(d) and 3(e) [87], [104], [105]. By controlling reactions between multiple metallic precursors and vapor phase cholcogens, the chemical composition of 2D TMDs materials can be tuned and thus their properties can be affected. For example, 2D monolayer $MoW_{2-x}S_2$ [106], [107] and 2D monolayer MoS_xSe_{2-x} [108]–[110], can be fabricated via controlling the ratio of each elements leading to tunable band gap energies. The tuning of stoichiometry of MoS_2 could give rise to various electrical and optical properties [111]–[113]. Apart from adjusting stoichiometric ratio during the fabrication process, conversion of chemical composition afterwards the growth of 2D

TMDs drew considerable attentions. The 2D $MoSe_2$ can be converted from 2D MoS_2 through ion-exchange reaction, resulting in enhancement of the optoelectrical properties [114], [115]. The selective growth of 2D TMDs materials may benefit the applications with special requirements. The 2D MoS_2 could be fabricated out of specific morphology and pattern, shown in Figure 3(f) and 3(g), under guidance of the lithographic techniques on the substrate following by spin-coating ammonium heptamolybate [116]. Certain surface treatment such as plasma etching is capable to strictly control the thickness and positions of 2D monolayered MoS_2 grown based on SiO_2 substrate [117]. In spite of those encouraging achievement mentioned above, the electrical properties of large-scale 2D TMDs are still insufficient for the requirement of realistic applications. For instance, 4 inches 2D MoS_2 based field-effect-transistor (FET) with uniformed thickness exhibits only 30 $cm^2V^{-1}s^{-1}$ [102] mobility, which is ten times lower than the devices crafted via mechanical exfoliation. The primary factor is the nature defects induced during chemical synthesis, such as vacancies known as intrinsic defects in 2D grains and grain boundaries known as interfacial defects. Major fabrication techniques of 2D TMDs materials are summarized in

Table 1 [79].

Table 1 Table showing various fabrication techniques of 2D TMDs materials.

Techniques	MBE	MOCVD	Powder Vaporozation	Mechanical exfoliation (and CVT)	Liquid Exfoliation
Single phase TMDs	2H $MoSe_2$ 2H Wse_2 1T $PtSe_2$	1T MoX_2 WX_2	1T, 2H MoX_2 1T, 2H WX_2	1T, 2H MoX_2 1T, 2H WX_2	1T, 2H MoX_2 1T, 2H WX_2
TMDs Alloy	-	-	MoS_xSe_{2-x} MoW_xS_{2-x}	$MoxW_{2-x}S_2$ $MoxW_{2-x}Se_2$	-
Doped TMDs	-	-	Mn-doped MoS_2 Co-doped MoS_2	Au-doped MoS_2 Re-doped MoS_2 Nb-doped MoS_2	-

Techniques	MBE	MOCVD	Powder Vaporozation	Mechanical exfoliation (and CVT)	Liquid Exfoliation
Vertical hetero-structures	$MoSe_2$-graphene	MoS_2-WS_2-graphene	$1T\ MoX_2$-$2H\ MoX_2$ $2H\ MoX_2$-$2H\ WX_2$ $2H\ MoS_2$-BP $2H\ MoX_2$-graphene $2H\ WX_2$-graphene $2H\ MoS_2$-$2H\ WSe_2$-graphene $2H\ WS_2$-hBN $2H\ MoS_2$-$SnSe_2$	$2H(MoS_2$-$WS_2)$ $2H(MoS_2$-$WSe_2)$ $2H\ MoS_2$-graphene $2H\ WS_2$-graphene $2H\ MoX_2$-hBN $2H\ WX_2$-hBN $2H\ WSe_2$-$1T\ SnSe_2$ $2H\ MoS_2$-BP	-
Lateral hetero-structures	-	-	-	$1T\ MoS_2$-$2H\ MoS_2$ $2H\ MoX_2$-$2H\ MoX_2$ $2H\ WX_2$-$2H\ WX_2$	-
Achieve-ments	High scalability	High scalability	High scalability	High crystallinity	High scalability

Techniques	MBE	MOCVD	Powder Vaporozation	Mechanical exfoliation (and CVT)	Liquid Exfoliation
Challenges	Defect control, domain size	Defect control	Defect control, uniformity, stoichiometry control	Thickness control, yield, not scalable	Small crystallites, thickness control, yield

*BP stands for Black Phosphorous

2.1.4 Electronical and optical properties of TMDs

2D TMDs materials is considered as a promising candidate for next generation FET for its capability to significantly reduce the size of device by serving as channel materials with atomic thickness. The main confinement of 2D TMDs materials comes from the contact issue of source and drain [118]–[122]. In traditional silicon based FET devices, the doping scheme was utilized to control the contact resistance and adjust the carrier type. Nonetheless, the lack of sufficient doping scheme in 2D TMDs materials leads to the requirement of metals with various work functions in order to fulfill the tasks. Since Schottky barriers will be engendered when forming the contacts between metal and 2D TMDs materials, the improvement of the transmissions of carriers will contingent on choice of appropriate materials with similar Fermi level, e.g. contacts between n-type MoS_2 and Sc [121], and between p-type MoS_2 and MoO_x [120]. Graphene, as mentioned before, holding a tunable Fermi level based on gate bias, usually forms contact with WSe_2 [118], [121]. Apart

THE HONG KONG
POLYTECHNIC UNIVERSITY
香港理工大學

DEPARTMENT OF
APPLIED PHYSICS
應用物理學系

from playing with work functions, doping is an alternative to control the properties of FET. Inducing metallic 1T phase in the contact between source and drain was reported with an enhancement of performance of MoS_2 FET [122], [123]. MoS_2 and $MoSe_2$ based FET were known as electrons transmissions dominated devices, whereas the ambipolar of WS_2 and WSe_2 affect the FET devices with both electrons and holes transmissions. With such unique property, the Fermi level of metal materials can be fixed at a certain value having no concern with its own work function [124]. In MoX_2 based FET the value can be maintained close to conduction band, while it can be kept in the middle of band gap in WX_2 based FET. The applications with SnS_2, $HfSe_2$, GaS, In_2Se_3 were benefited from such property as well [125]–[128].

The criterion of carrier mobility reveals weaker capability of carrier transportation in TMDs materials comparing to graphene, as shown in Figure 4(a) [129]. The high intensity of energy levels concentrating in the center of band gap may attribute to the disarrangement [130], originated from dislocations, vacancies, disvacancies, adsorbate or bonding between metal and chalcogen elements [131]–[133], impacting carrier mobility of TMDs materials. Fortunately, the mobility did not limit the development of 2D TMDs FETs based IC applications, such as signal generator [134], and digital inverters [135], as shown in Figure 4(b) and Figure 5(a), respectively. 2D TMDs materials exhibit encouraging potential on applications of thin film transistor (TFT) thanks to their vdW epitaxy and atomic thickness resulting in flexibility and transparent nature [129]. WSe_2 based TFTs were fabricated with promising performances shown in Figure 5(b) [121]. TMDs were regarded as ideal

candidate for sensor and detector due to their high specific area. MoS_2 and WS_2 based FET have been implemented in sensing of toxic, pH value of protein, and biologic molecules with unknown constituents as shown in Figure 5(c) [136]–[138]. TMDs also drew significant attentions in the field of energy storage because of their promising light absorption and conductivity [139].
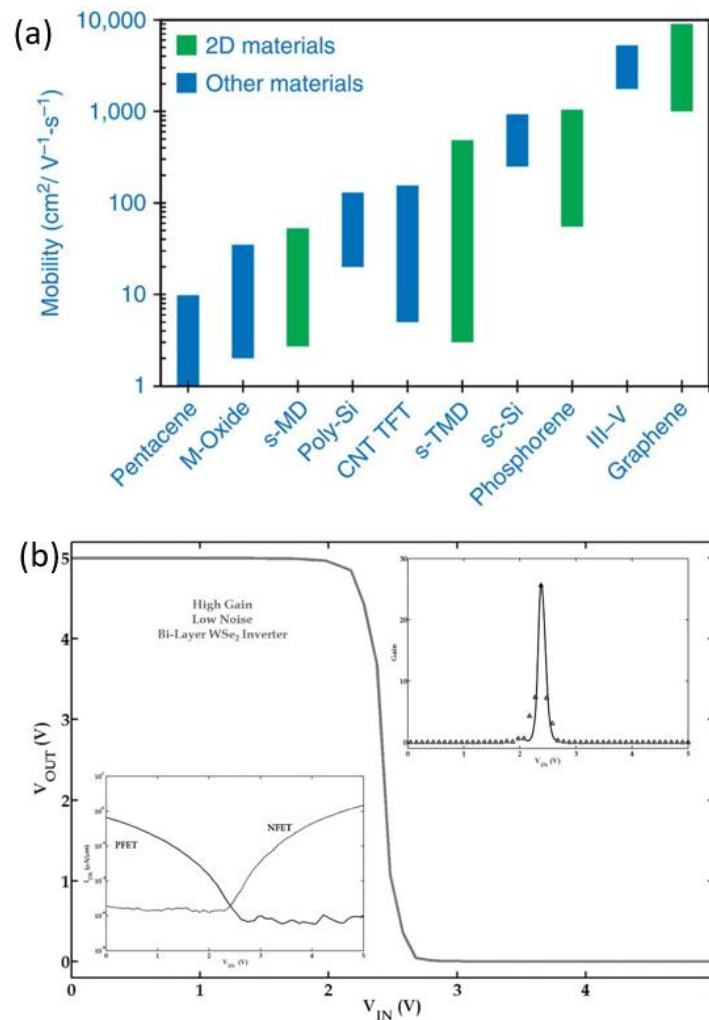
Figure 4 (a) Carrier mobility of various semiconducting materials [129]. (b) Signal generator based on graphene/MoS_2 heterojunction [134].
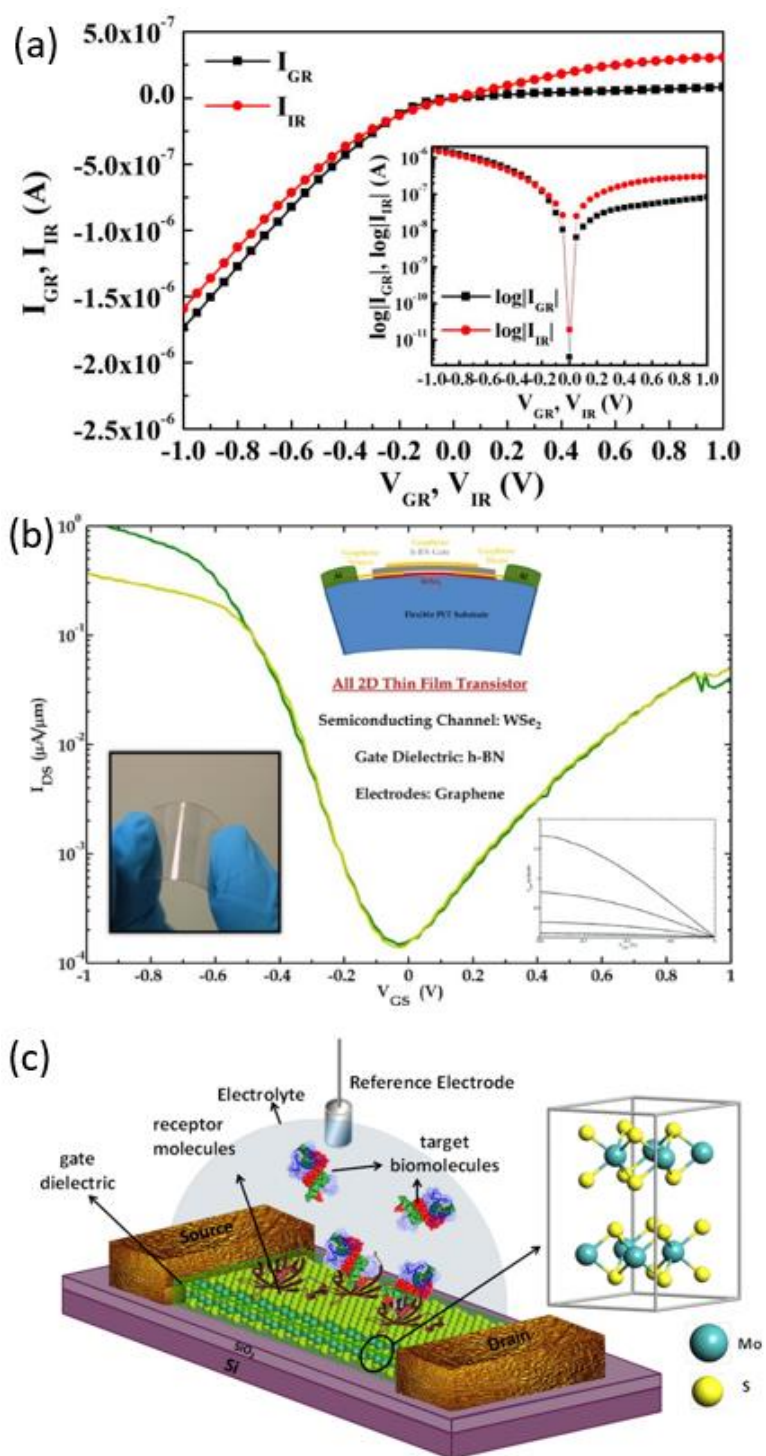
Figure 5 (a) Digital inverter based on WSe$_2$ [135]. (b) WSe$_2$ based thin film transistor (TFT) for flexible electronic [121]. (c) A MoS$_2$ FET based biosensor [137].

2D TMDs were implemented into thin film devices to study the principles of light absorption and emissions, offering opportunities in exploring advancing optoelectronic devices, such as light emitting diodes (LEDs), photodetectors, lasers, optical cavities, and so on [140]–[146]. Even limited by contact resistance, the first generation 2D phototransistors showed a high photoresponsivity with 120 mA/W [144]. The contact resistance was received a reduction by applying single layer WSe_2 as active layer, obtaining 1.8×10^5 A/W photoresponsivity [146]. Later on, the photoresponsivity was enhanced up to 5×10^8 A/W by combining graphene which holds excellent carrier mobility and MoS_2 into graphene-MoS_2 hybrid phototransistor [140]. Photodetectors were also benefited from two local bottom gates in 2D TMDs, exhibiting efficiency of 320 mA/W with WSe_2 p-n photodiodes. The 2D TMDs are regarding as a candidate to replace Silicon based photodetectors [141].

2D TMDs also stimulate the development of other optical applications. Generally, the light absorbent film in atomic scale is critical to solar cells or photodetectors. The common structure is based on Salisbury screen. A cavity is formed by depositing an absorbent layer at the position of 1/4 wavelength from reflecting bottom layer. Such structure enhances absorption of atomic layer thin film, however, confines the light wavelength due to Fabry-Perot resonance [147]. Solutions to broaden the absorptive light wavelength are suggested to took considerations of light anisotropy which originated from principles of electromagnetics. Therefore, layered structure materials are failed to accord with many photonic structures due to their exclusive absorption for electric field parallel to the plane [148]. Techniques such as plasmonic techniques

[149], and structures of dielectric gap-mode [150], are able to significantly increase the electric field perpendicular to the plane [151]. Similar anisotropy was observed in photoluminescence (PL) of MoS_2 [152]. The photonic structures require taking consider of anisotropy at the stage of experiment design in order to enhance the light emission [153], [154].

2.1.5 Group-10 TMDs

Group-10 TMDs materials started to receive attentions from the works of PdS_2/$PdSe_2$ and PtS_2/$PtSe_2$ reported by Grønvold and Kjekshus's group, respectively [155]–[157]. There was a debate on-going in 1970 about the electronic structure of Platinum chalcogens, with or without semiconducting properties [158]. The fabrication and application of those materials was at period of infancy due to the cost of noble metals. As the development of fabrication and exfoliation techniques, achieving the few-layer or monolayer of group-10 TMDs becomes capable with a relatively low cost. The price no longer serves as the confinement to their fundamental researches and applications.

Similar to other 1T-TMDs members, such as MoS_2 and WS_2, group-10 TMDs consist of a group-10 noble metal sandwiched by 6 chalcogen atoms, forming an octahedral structure [16]. Because group-10 noble metals hold binding energies of their valence d-orbitals which are very similar to that of valence p-orbitals in chalcogen elements, the electronic structures of group-10 TMDs materials drew significant attentions in recent years [159], [160]. Exceeding of various hybridizations are drew forth owing

to this similarity comparing to traditional 4-9 groups TMDs materials [161], giving rise to advancing electronic structures and properties remains to be discovered.

Platinum disulfide (PtS$_2$) recently was reported exhibiting 1107 cm^{2}V^{-1}s^{-1} of phonon-limited mobility under room temperature [23], [162], [163]. Apart from the promising conductivity, group-10 TMDs show outstanding performances in superconductivity, broad tunable band gap, and stability. PtS$_2$ was applied on and considered as a candidate for novel optoelectronic devices, such as Q-switched laser [164], field-effect transitor (FET) [26], and catalysis [49], thanks to its tunable indirect band gap from 0.25 eV of bulky structure to 1.6 eV of monolayer structure [26], [27]. PdS$_2$ was revealed to be semiconductor with 1.00 eV of indirect band gap only when it reached monolayer thickness [53]. Researchers recently focused to study its performances on catalysis, optical, electrical applications [54]. PdSe$_2$ holds similar electronic properties to PdS$_2$, showing metallic to a 1.31 eV indirect band gap of semiconducting characteristic when the thickness scaled down from bulk to its monolayer counterpart [47]. Its promising optoelectronic properties benefit the development of novel semiconducting devices such as FET [56], photodetector [57], and thermal electricity [55].

2.1.6 2D TMDs Quantum Dots

Quantum Dots (QDs) were widely implemented into advancing research fields such as imaging, sensing, or labeling, for their exceptional optical properties [165]–[169]. QDs are defined as the size of material reaches nanoscale, specifically smaller than their bohr radius, resulting in unique properties that attribute to edge and quantum

confinement effects [170]. For TMDs family, MoS_2, WS_2, $MoSe_2$ QDs were extensively investigated over years due to their atomic scale sizes, considerable specific surface area, active edge sites and direct band gap semiconducting characteristics [171]. For example, WS_2 QDs exhibit a strong florescence thanks to the 3.16 eV direct band gap. WS_2 QDs are also considered as promising materials for spintronics applications for their huge spin-valley coupling [37]. TMDs QDs exhibit competitive performance as electrocatalysts for hydrogen evolution reaction (HER) thanks to their similar hydrogen absorption energy to Platinum [40], [170]. Even though TMDs QDs received many attentions from the society, the understand and applications in this field are still in the babyhood. For now, majority of researchers are focusing on the nanosheet structure of TMDs materials. The QDs counterpart still requires further explorations on the synthesis, principles, and application-related aspects.

2.1.7 Synthesis of TMDs QDs

Owing to weak Van der Waals force between adjacent layers, TMDs materials are capable separated by expanding the interlayer spacing. This opens up the gate for fabricating TMDs QDs. Several fabrication techniques of TMDs QDs have been developed, such as mechanical exfoliation, chopping, chemical vapor deposition (CVD), intercalation, laser pulse ablation [170], [172], and hydrothermal reactions, and summarized in

Table 2.

Table 2 Fabrication techniques for TMDs QDs, where N/A means not applicable.

Techniques	TMDs QDs	Process	Yield	Ref.
Mechanical exfoliation and chopping	MoS_2	Ultrasonication in DMF	N/A	[173]
	MoS_2	Ultrasonication in NMP	N/A	[174]
	MoS_2	Ultrasonication in TBA	N/A	[175]
	MoS_2 /WS_2	Mechanical exfoliation in DMF	N/A	[176]
	MoS_2/WSe_2/WS_2	Ultrasonication in PVP	N/A	[177]
	WS_2	Vigorous stirring in NMP	N/A	[178]
	WS_2	Mechanical exfoliation in non-ionic pluronic surfactant	N/A	[179]
	$MoSe_2$	Probe ultrasonication in NMP	5.2–8.1%	[180]
	$MoSe_2$	Ultrasonication in DMF and alkali metal ions	4.84%	[181]
Intercalation-assisted exfoliation	WS_2	Heating followed by ultrasonic vibrator in $EtOH/H_2O$	4%	[182]
	WS_2	Exfoliated by electric field in propylene carbonate with 0.1 wt% $LiClO_4$	5%	[183]
	WSe_2	Vigorous stirring in dimethylsulfoxide	N/A	[184]

Techniques	TMDs QDs	Process	Yield	Ref.
	MoS_2	Ultrasonication in water	11%	[178]
	MoS_2	Vigorous stirring in DMF	2.28%	[185]
	MoS_2	Ultrasonication in H_2SO_4	9.65%	[186]
Free radical etching	MoS_2	Etching by electro-Fenton reaction in electrolytic cell	N/A	[187]
	WS_2	Work as electrode by mixing with acetylene black and poly(vinylidene fluoride) (PVDF) in NMP	N/A	[188]
Hydrothermal reaction	WS_2	Ultrasonication-hydrothermal	1.8%	[189]
	MoS_2	Ultrasonication in DMF and heating in oil bath	5.6%	[190]
	MoS_2	Ultrasonication-hydrothermal	3.2%	[191]
	MoS_2/WS_2	Exfoliation in DMF followed by stirring and heating	N/A	[40]
	MoS_2	Hydrothermal in autoclave	10.3%	[192]
Other synthesis methods	MoS_2	$MoCl_5$, L-cysteine and OLA precursors heated in three-neck round bottom flask at 60 °C for 1 h under Ar	N/A	[193]

THE HONG KONG
POLYTECHNIC UNIVERSITY
香港理工大學

DEPARTMENT OF
APPLIED PHYSICS
應用物理學系

Techniques	TMDs QDs	Process	Yield	Ref.
	MoS_2	$(NH_4)_2MoS_4$, oleic acid, OLA and 1-octadecene precursors heated at 120 °C under vacuum followed by heating under 250 °C with nitrogen atmosphere	4.4%	[194]
	MoS_2	Implementing bulk MoS_2 in temporally shaped femtosecond laser ablation	N/A	[195]
	WS_2	Using WS_2 powder and diethylenetriamine (DETA) as dopant to conduct pulse with laser ablation	15.2%	[196]

In general, mechanical exfoliation represents for a category of approaches weaken the interlayer interactions via external influences, for instance, grinding, ultrasonic vibration, cutting, or other mechanical energies. Mechanical exfoliation is considered as a convenient and environment friendly technique for mass-production of TMDs QDs.

Intercalation-assisted exfoliation enhances efficiency for achieving TMDs QDs. The inserted atoms, ions, or molecules expand the interlayer spacing and weaken the Van der Waals interaction between adjacent layers. Combining intercalation with liquid exfoliation becomes a convenient and low-cost technique to produce TMDs QDs. Assisted via the grinding, electrochemical process, and ultrasonic vibrations, the alkali materials or other small molecules are easily inserted into layers. Such

efficient technique also encounters limitation of ion pollutions, which induce various types of atoms, ions, or molecules into the final product, resulting in engendering some unexpected consequence on the performance. For example, alkali metals, such as butyl lithium [197], may cause phase transition in QDs and absence of semiconducting properties.

Hydrothermal reaction has been developed extensively to fabricate TMDs QDs. The fabrication process generally includes 2 steps: implementing liquid exfoliation to disassemble bulk TMDs materials into nanosheet counterpart; obtaining QDs via a top-down hydrothermal reaction. QDs achieved by such technique usually display promising dispersion ability, low toxicity to organism, small size, and high compatibility to various biology environment.

Apart from techniques mentioned above, the fabrication methods of TMDs QDs are investigated over time. Several techniques, e.g. CVD and laser pulse ablation, are capable to produce high quality TMDs QDs as well. Han's group reported fabrication methods to obtain MoS_2 QDs via insulating copolymer patterning and oxygen plasma etching [198]. An environment friendly alternative to fabricate MoS_2 QDs were also developed by Li's group via conducting ablation to bulk materials in water with femtosecond laser [195]. Functionalized TMDs QDs were successfully obtained via continuous femtosecond laser treatment, that reduced TMDs bulk to nanoscale thanks to Coulomb explosion and destroyed bonding between 2D materials and solvent molecule, resulting in a simultaneous functionalization and fabrication of TMDs QDs.

2.2 Principles

2.2.1 Q-switching

The peak power of laser is dominated by two factors: the pulse duration and the pulse energy. The shorter pulse duration is, the energy is higher, and the peak power then becomes higher. Another parameter that plays important role in pulse generation is the resonator quality factor Q, which is defined as the ratio of the energy stored in cavity to the energy dissipated during each cycle. The higher the factor Q, the higher will be the energy in the cavity, or the lower will be the energy loss per radian of oscillation. Manually switching the value of Q will generate laser pulse of enforcement. Q-switching laser is therefore named. Once the Q-switching activation condition is fulfilled, the stored energy will be released in the form of a single pulse. The energy in the cavity is originated from population inversion via pumping. Resonator is used to store the energy for controlling the Q factor and process of Q-switching lasing. Even though the stored energy exceeds the threshold of lasing, the cavity gives no energy output due to the low Q state which is controlled by resonator. The loss is set to be too high for generating laser. In such statues, the population inversion process is accumulating, and the energy stored in high energy level is not capable to relax to ground state. When the resonator sets the cavity in high Q factor, the Q-switching takes place. In other words, the laser is generated in a very short single pulse with releasing all the energy stored before. The procedures of Q-switch pulse are shown in Figure 6 [199]. Since the peak power of Q-switching

laser is extremely high, this technique usually is applied on microstructuring, remote sensing, generating pumping source, and so on.

In general, Q-switching includes active and passive Q-switching technique. For active Q-switching, the factor Q is dominated by an active modulator, for example, an acousto-optic or electro-optic modulator. The pulse generation can be mandatory conducted by electrical signal. Mechanical modulators such as spinning mirrors are used for Q-switching as well. The gain medium plays vital role in controlling the pulse energy and pulse duration.
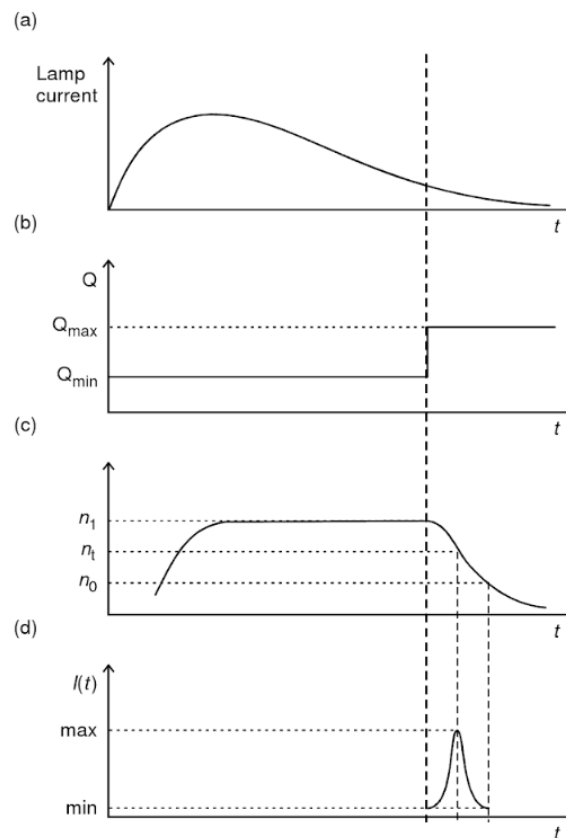
Figure 6 Mechanism of Q-switched pulse: (a) pumping, (b) quality factor Q switching process, (c) energy stored in the system, (d) the generation of the pulse [199].

Passive Q-switching usually controls the losses via adding a component name saturable absorber (SA). When the energy stored in SA accumulated to certain intensity, the pulse then will be generated. The pulse energy and pulse duration generally are not affected by changing pump power, except for pulse repetition rate. The common materials for passive Q-switching include: Cr^{4+}:YAG for 1-μm YAG lasers, Co^{2+}:$MgAl_2O_4$ for 1.5-μm erbium lasers, V^{3+}:YAG crystals for 1.3-μm region and so on. Passive Q-switching is usually considered a better solution due to the simple fabrication, low cost, and reliable operation.

2.2.2 Saturable absorber

It is known that two important factors of Q-switching are controllable resonator quality factor Q, and rapid switch between low and high value of Q. In passive Q-switching, SA is introduced in the cavity for the solution. The passively Q-switched lasing generally occurs spontaneously in SA when the activation condition is once fulfilled. SA normally experience an unsaturated loss process during receiving energy from pumping. The molecules are excited to upper level and the energy are accumulating until the depletion of ground state. Once SA is saturated, a single pulse with entire stored energy will be released. The higher unsaturated losses may enlarge the delay between pumping and pulse generation, leading to higher energy stored before release. As a consequence, the pulse will be generated with higher pulse energy and shorter pulse duration. Nevertheless, the exorbitant unsaturated losses may eliminate the lasing process.

2.2.3 Photoluminescence

Photoluminescence performances are generally expressed as a diagram of fluorescence emission spectra where photoluminescence intensity (Y-axis) versus to wavelength or wavenumber (X-axis). As two typical emission spectra shown in Figure 7, perylene, a very traditional fluorephore, holds individual vibrational energy level, where quinine exhibits emission spectra independent to vibrational structure [200]. Different chemical composition and solvent may engender profound difference in photoluminescence performance.
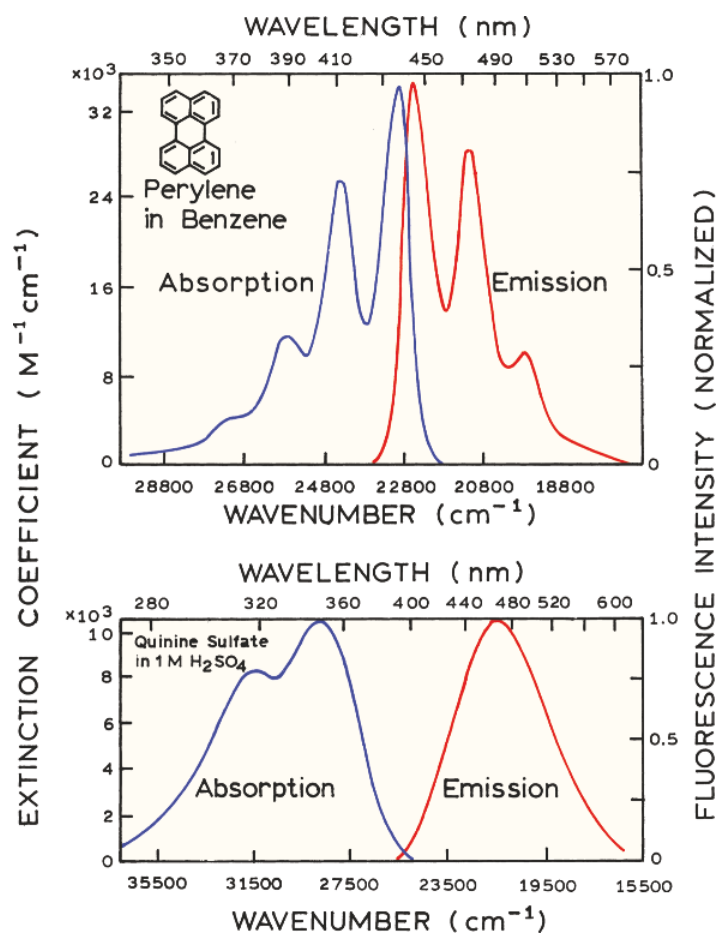
Figure 7 Absorption and fluorescence emission spectra of perylene and quinine [200].

The relationship between absorption and emission is generally depicted in Jablonski diagram as shown in Figure 8. Various processes can be explained as transitions in excited states, where singlet ground state, 1st and 2nd electronic states can be represented as S0, S1, and S2. Every electronic energy state includes several vibrational energy levels, such as 0, 1, and 2 vibrational energy level shown in S0 states. The transitional within the energy levels or states are shown as arrows signals, illustrating the instantaneous processes (within 10^{-15}s) of absorptions or emissions of natural optical energy. Such rapid processes are commonly too short for taking place of nuclei displacement.
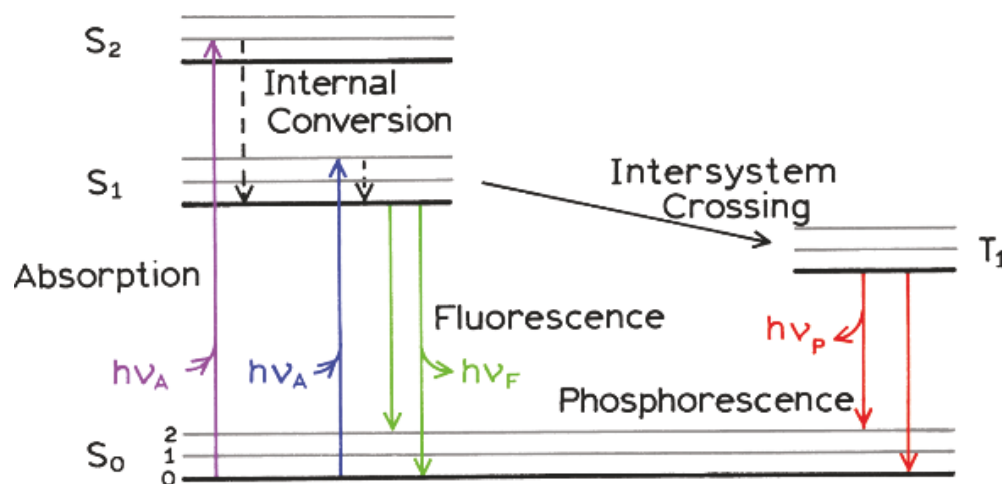
Figure 8 A typical Jablonski diagram [200].

The vibrational energy levels can be individually told from spacing of energy peaks appearing in perylene's emission spectrum, as shown in Figure 7. The absorption and emission process usually give rise to molecules with the lowest vibrational energy. Under room temperature, the heat energy is not sufficient for transition between excited and ground vibrational states. In other words, the significant

difference between S0 and S1 can only be overcome by light induction rather than heat energy. Several processes will be caused after light absorption. Few of molecules in condensed phase will follow internal conversion rule via dropping to the lowest vibrational level in S1. This sudden process usually takes place in 10^{-12}s which is much shorter than an average 10^{-8}s for fluorescence. Due to internal conversion, the PL emission generally is a transition process taking place from thermally equilibrated excited state, in other words, the lowest vibrational energy level in S1, to S0 energy states.

Molecules will return to an excited vibrational energy level after relaxation from higher energy state to lower energy state. Another 10^{-12} s are required to achieve thermal equilibrium. The typical vibrational structure of emission spectrum of perylene shown in Figure 7 is attribute to this relaxation when molecule return to an excited vibrational level of S0 state. The absorption spectrum normally illustrates a mirror structure with emission spectrum due to nuclear geometry which is remaining unaffected during excitation process. Therefore, the vibrational energy levels in higher energy state (S1 or S2) are similar to the ground energy state (S0), resulting in mirror spectra of absorption and emission process.

The molecule under excited energy state may undergo a spin conversion and therefore relax on first triplet state (T1). The emission generated from T1 is known as phosphorescence, which generally decay to longer wavelengths. The transition which is so called intersystem crossing from S1 to T1 is nonreversing. The

phosphorescence normally exhibits rate constants far smaller than that of fluorescence.

2.2.4 Stokes shift

Jablonski diagram shown in Figure 8 illustrates a phenomenon that the energy of emission is always less than that of excitation [200]. In other words, the emission usually occurs at longer wavelength comparing to excitation wavelength. This fact was firstly discovered by Sir. G. G. Stokes in 1852 [201]. Such energy loss between excitation and emission is then widely observed in several fluorescence materials. The differential of excitation wavelength and emission wavelength is defined as stokes shifts. Its origin is generally considered as the presence of energy loss during internal conversion process. Additionally, the emission process normally decays to an excited energy level in S0 state, giving rise to thermalization process for relaxing extra vibrational energy to ground energy level. Apart from transition process, several factors may also take part in stokes shifts, for example, solvent reaction, chemical composition, energy transfer, or excited-state reactions.

2.2.5 PL properties of TMD QDs

TMDs QDs display promising optical properties. Thanks to quantum confinement effect, QDs structure significantly enhances PL intensity comparing to their bulk TMDs and nanosheet counterparts. MoS_2 is affirmed to exhibit layer-dependent band gap according to Heinz's study. Its indirect band gap for bulk structure can be transform into direct band gap nature when the thickness is reduced to few layers.

The PL Quantum Yield (QY) is capable to be enhanced along with the decrease of thickness. However, QY of few-layered MoS_2 exhibit a value of around 10^{-5}–10^{-6}. Likewise, its monolayer counterpart shows only 4×10^{-3} of QY. Such poor QY leads to undetectable PL intensities by instruments, resulting in limitation in optical applications. Fabrication of TMDs QDs becomes a solution to enhance the QY. In order to tailor the QDs into practical applications, it is critical to understand the fundamental PL nature of TMDs QDs.

Size plays a decisive role to influence the PL behavior of TMDs QDs. Size-controllable single layer WSe_2 QDs is successfully achieved by Jin's group [184]. They announced that PL spectra of colloidal WSe_2 QDs blue-shift along with the decrease of radius of QDs, indicating the exist of quantum confinement effect. An exitonic PL related to single-layer WSe_2 nanosheet has been detected, implying presence of defect emissions or heterogeneous broadenings. The PL and PL excitation (PLE) spectra of single WSe_2 QD are investigated to understand the principles of emission, as shown in Figure 9. Other than colloidal solution, single QD exhibit a distinct excitation independent property. Such unique behavior may be due to the uniform size distribution and enhanced vibronic coupling. Hence, owing to size-dependent optical band gap, stokes shift and spectra width increase with the decrease of QDs sizes.

Size effect is capable to determine the PL behavior. Luan reports that the PL behaviors at ultraviolet and visible range are dominated by different principles according to the study of $MoSe_2$ QDs [180].PL emission in ultraviolet range is
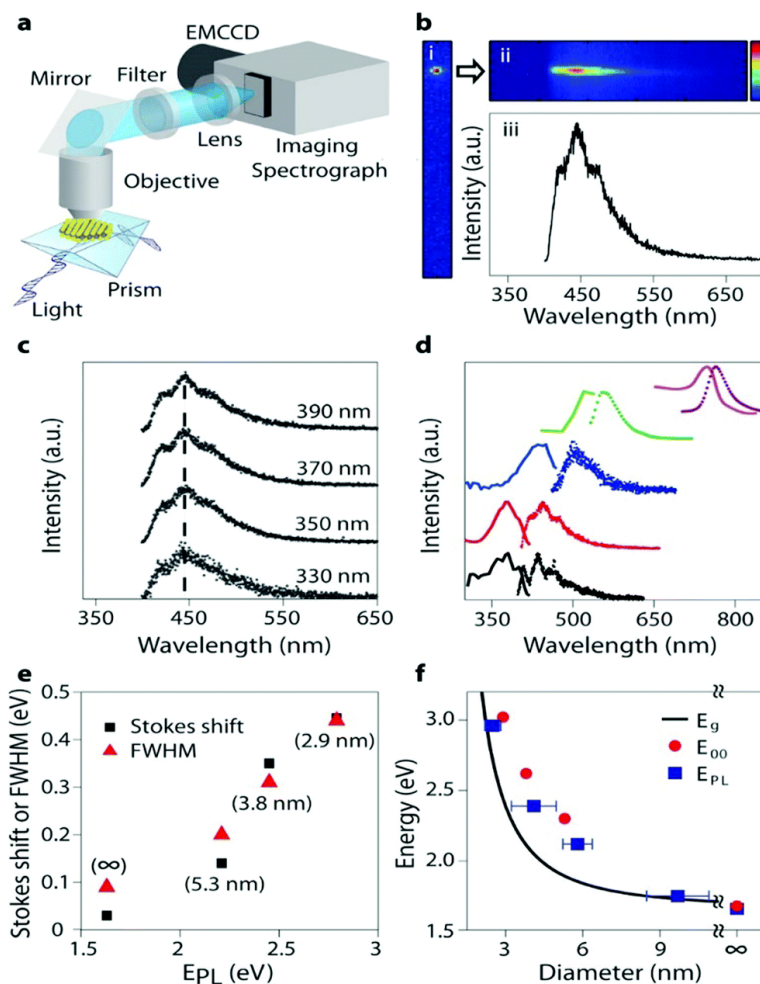
Figure 9 WSe$_2$ QDs PL and PLE behaviors [202]. (a) Schematic diagram of the setup for the instruments for PL and PLE measurement. (b) Charge-coupled device (CCD) image and PL spectrum of a single WSe$_2$ QD. (c) Excitation-wavelength-independent PL behaviors for a single WSe$_2$ QD. (d) PL (dotted) and PLE (solid) spectra of different single WSe$_2$ QDs. (e) PL width (FWHM) or stokes shift versus peak energy of PL, where ∞ sign represents for the 2D exciton in single-layer WSe$_2$ sheets. (f) The 0–0 energy (E$_{00}$) of single WSe$_2$ QDs (red dot); E$_{PL}$ of diameter-dependent WSe$_2$ QD solution (blue square); and the estimated bandgap (Eg) energy according to the effective mass approximation as a function of diameter [184].

resulted from transitions between valence band and the conduction band. The red-shifts or blue-shifts of the emission signal due to quantum confinement effect. PL emission in visible spectrum range may attribute to nonradiative recombination which is owing to surface defect. The decrease of size will enlarge the band gap according to Gan's study of MoS_2 QDs [203]. When the size shrinks from bulk to nanoscale, four typical excitonic absorption bands will vanish and the spectra will undergo a blue-shift. Along with the agglomeration of QDs, red-shift phenomenon can be observed which agrees with quantum confinement effect. Gopalakrishnan successfully fabrications MoS_2 QDs in ionic liquid solution via electrochemical process [204]. He announces that the PL of MoS_2 QDs arises from recombination occurring at uncompensated electron or hole traps. A red-shift stems from reduces of size contradicting to quantum confinement effect was observed, attributing to the formation of deeper traps. Specific surface area will rise when the size of QD decrease, accompanying with increase of traps states due to increase of uncompensated metal ions or sulfions.

2.2.6 Excitation-dependent PL behavior

Excitation-dependent PL behaviors can be observed in the majority of TMDs QDs [180], [204]–[208]. The emission generates at longer wavelength with the red-shift of excitation wavelength. As Gopalakrishnan reports, red-shift may be triggered by deeper trap states. The principles of excitation-dependence in TMDs QDs yet remain to be revealed, however, several possibilities are under concerned. The main factors are taken for (1) polydispersity of QDs; (2) various discretions of energy states in

QDs; (3) trap states; (4) hot PL affected by K point of Brillouin zone; (5) inhomogeneous ground states [178], [209]. For instance, the recombination process arising at surface of quantum-confined MoS_2 QDs gives rise to PL emission peak at 570 nm under 500 nm excitation wavelength [174]. The bottom-up synthesis technique is reported by Wand and Ni. The excitation-dependent PL ascribes to polydispersity of MoS_2 QDs and hot PL at K point of Brillouin zone [206]. The outstanding excitation-dependent PL performance of $MoSe_2$ QDs may be due to the polydispersity as well [208]. WS_2 QDs fabricated by electrochemical technique exhibit excitation-dependent PL, attributing to oxygen moieties adsorbed at the edge of QDs [183]. The defect states and edge site introduced during fabrication process are as well fulfilling important roles to dominate the excitation-dependent behaviors of TMDs QDs [175], [210].

Excitation-independent properties are observed in TMDs QDs. Zhang's group reports MoS_2 QDs fabricated via sulfuric acid-assisted ultrasonic exfoliation with absence of excitation-dependent behavior [186]. MoS_2 QDs obtained via wet grinding-assisted co-solvent sonication exhibit high uniformity, resulting in a distinct PL emission wavelength at 448 nm under various excitation wavelength [191]. Cheon's group discovered excitation-independent PL behavior from colloidal and single-particle WSe_2 QDs [184]. They explain such behavior may ascribe to homogeneous size distribution, which is agreed with Zhu's study for MoS_2 QDs [211].

2.3 Characterizations

In my PhD study period, I am mainly working on the optical performances, such as laser Q-switch and photoluminescences, of novel group-10 TMDs materials. In order to understand the relationships between their optical performances and the features of materials, several characterization techniques are engaged in this study. For identifying materials chemical composition and structure, the characterization techniques include field emission scanning electron microscopy, transmission electron microscopy, atomic force microscopy, X-ray photoelectron spectroscopy. The optical properties are measured by ultraviolet–visible absorption spectroscopy, photoluminescence spectroscopy. Details can be found in the relevant section in the following chapters.

2.3.1 Scanning Electron Microscopy

Scanning electron microscopy is a universal approach to study the materials in microcosmic due to its capability in producing images with information about surface morphology and structure in high resolution. Images of SEM are generated by interaction of high-energy beam of electrons. After electrons hitting the sample, secondary electrons (SE), reflected or back-scattered electrons (BSE), characteristic Cathodoluminescence (CL), absorbed current (specimen current) and transmitted electrons are produced. Certain images are then produced after signals collected by detectors. This technique is considered to be non-destructive due to no volume dissipated during the test. The morphology of PtS_2 microflakes presented in this thesis is shot by S-4800 SEM as shown in Figure 10.

Figure 10 S-4800 Scanning Electron Microscopy.

2.3.2 Transmission Electron Microscopy

Transmission electron microscopy (TEM) is an advanced instrument to produce high-resolution image by a beam of electrons that pass through a grid attached with samples. An image is then formed by magnification and focusing on an imaging screen. Such image holds extremely high resolution which is able to capture the crystal details of single atoms due to the small de Broglie wavelength of electron. The TEM images of group-10 TMDs microflakes and QDs in this study are achieved by Jeol JEM-2100F as shown in Figure 11.

THE HONG KONG
POLYTECHNIC UNIVERSITY
香港理工大學

DEPARTMENT OF
APPLIED PHYSICS
應用物理學系

Figure 11 Jeol JEM-2100F Transmission Electron Microscopy.

2.3.3 Atomic Force Microscopy

Atomic Force Microscopy (AFM) is kin to scanning probe microscopy. The measurement is analogous to "touching" or "feeling" the surface by a probe. The probe is raster-scanned over the surface of samples with assistance of precise

movement owing to piezoelectric elements. The topography image is then produced

with accurate feedbacks from the probe. AFM measurement is friendly to both

conductive or non-conductive samples thanks to its principle of tip-sample interaction.

The AFM mapping images of group-10 TMDs microflakes and QDs in this work are

obtained by Bruker Nanoscope 8 as shown in Figure 12.
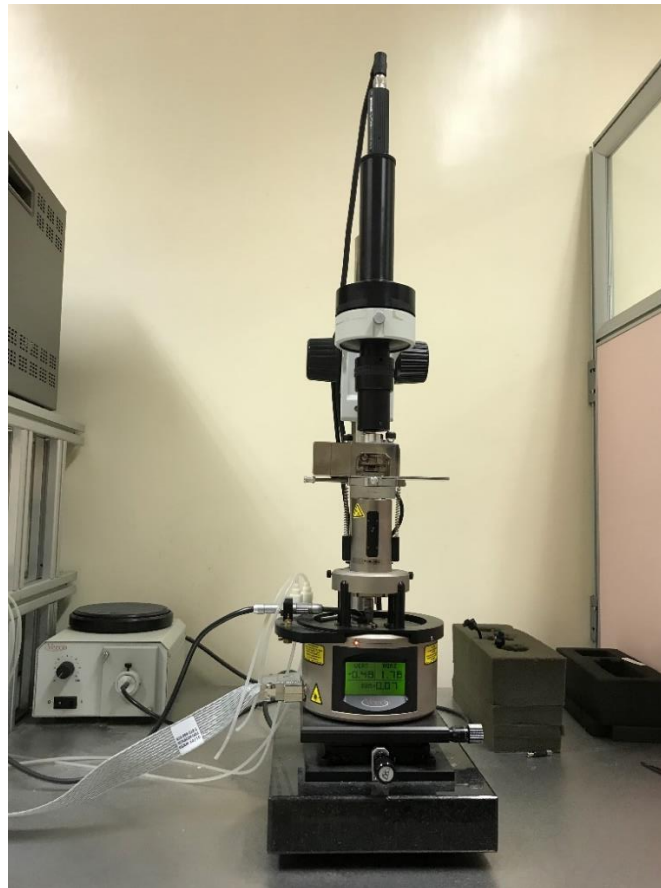
Figure 12 Bruker Nanoscope 8 Atomic Force Microscopy.

2.3.4 X-ray photoelectron spectroscopy

X-ray photoelectron spectroscopy (XPS) is an advanced analyzation technique for

elemental composition, empirical formula, chemical state and electronic state of

materials. The mechanism is irradiating a beam of X-rays to the sample and simultaneously analyze the kinetic energy of electrons that emitted from the surface of sample. The ejected electrons are counted according to a range of electron kinetic energy. The energy and intensity of photoelectron peaks is capable to be identified and qualified. The XPS spectrums of group-10 TMDs materials in this works are obtained from ESCALAB 250Xi with achromatic 200W Al Kα as the X-ray source and the resolution of 0.10 eV as shown in Figure 13.

Figure 13 ESCALAB 250Xi X-ray photoelectron spectroscopy.

2.3.5 Ultraviolet–visible absorption spectroscopy

Ultraviolet–visible absorption spectroscopy (UV–Vis) is used to analyze the light that affected by chemicals in visible and adjacent ultraviolet range. In such electromagnetic spectrum, the electronic transitions from the ground state to the excited state are able to be recorded with typical characteristic waveforms, which is complementary to photoluminescence spectroscopy. The UV-Vis spectra of group-10 TMDs QDs in this study are recorded by Shimadzu UV-2550 as shown in Figure 14.

Figure 14 Shimadzu UV-2550 Ultraviolet–visible absorption spectroscopy.

2.3.6 Photoluminescence spectroscopy

Photoluminescence spectroscopy is a contactless, non-destructive technique to reveal the electronic structure of samples. Excitation and emission spectra of group-10 TMDs QDs were obtained using an Edinburgh CD920, shown in Figure 15, conducting under room temperature with Xenon lamp as excitation source. Time-Resolved measurements were monitored by HORIBA Fluorolog-3 spectrometer for ultrafast studies and time-correlated single-photon counting (TCSPC) accessory for lifetime determinations.

Figure 15 Edinburgh CD920 Photoluminescence spectroscopy.

Chapter 3 Q-switched Laser with PtS$_2$ microflakes saturable absorber

3.1 Introduction

TMDs exhibit potentials as an alternative to traditional doped crystal for saturable absorber (SA), due to its stability and economical fabrication. Few layer MoS$_2$ exhibits Q-switching ability that generates 2.88 μs pulses at 74 kHz repetition rate, with 100 nJ pulse energy [17]. The Q-switched signals are successfully achieved in ytterbium-, erbium- and thulium-doped fiber lasers using MoSe$_2$ as SA [19]. Wu reports a WS$_2$ based SA producing Q-switching laser with tunable repetition rate from 90 kHz to 125 kHz and pulse energy with tens of nJ [20]. Later, Q-switching pulse generated by WSe$_2$ SA is developed with similar performance with WS$_2$ based SA.

The traditional TMDs based SAs show encouraging Q-switching behavior with low-cost, simple fabrication process. This stimulates me to explore more uncharted candidates for SA development. Novel group-10 TMDs start achieving attentions due to their tunable bandgap, high electrical properties, and air stability. In this work, PtS$_2$, a member of group-10 TMDs family, microflakes based SA is produced, following by an analyzation of its Q-switching performance.

3.2 PtS$_2$ saturable absorber fabrication and characterizations

The PtS$_2$ microflakes are fabricated via liquid exfoliation to separate layered

materials from the bulk counterparts as shown in Figure 16. NMP was chosen as solvent for conducting liquid exfoliation due to its great compatibility of surface energy with TMDs materials. 50 mg bulk PtS_2 powder (Alfa Aesar) was added into 250ml NMP solvent followed by probe sonication using SCIENTZ-1200E (Ningbo Scientz Biotechnology Co., Ltd). The sonication was conducted under the power of 1200 W with 20 kHz below 27 °C for 3 h, with an ultrasound probe time of 2 s at an interval of 4 s. The as-prepared PtS_2 microflakes solution was centrifuged in the ambient environment at 1500 rpm for 5 min to precipitate the large bulks that are not sufficiently separated. Then the supernatant liquor was taken for further characterizations. The sample was prepared by drop casting the PtS_2 supernatant solution on the surface of the quartz substrate and then drying in glove box with nitrogen atmosphere to prevent it from oxidization. A 15.0 g of polyvinyl alcohol (PVA) was dissolved in 85 g of NMP to give a 15 wt. % gel-like solution. Then, 0.4 g of this solution was mixed with 2.0 g as-prepared PtS_2 supernatant liquor and stirred for 30 min to produce the SA. The mixture was dried under 60 °C for 48 h in the oven, yielding PtS_2/PVA composite film.
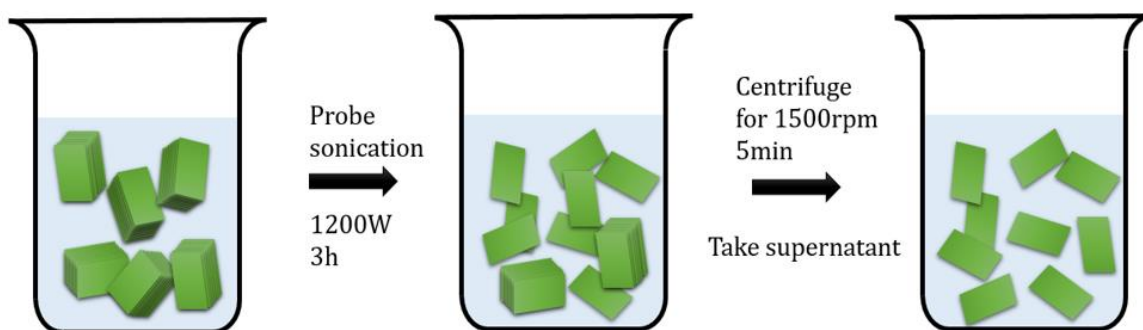
Figure 16 Fabrication of PtS_2 microflakes.

The dominant PtS_2 samples with similar dimensions were observed by field emission scanning electron microscope (FESEM, S-4800, Hitachi – Science & Technology), as shown in Figure 17(a). The statics of size distribution among 170 flakes represents that an average dimension along the short-axis is 1.35 µm roughly and an approximately 2.40 µm size for long-axis, as shown in Figure 17(b) and 9(c), respectively. The atomic force microscopy (AFM, Bruker Nanoscope 8) was carried out to measure the thickness of the exfoliated PtS_2 samples. Topology graph of a typical sample and associated height variations along the marked lines are depicted in Figure 18(a) and 10(b). The lateral dimensions of 3.16 µm for long-axis and 1.59 µm for short-axis agree with the statics of SEM distribution. The thickness was measured to be around 0.35 µm which explains that it is far beyond the nano-regime. Combining the thickness with SEM analysis, those dimensions indicate that the ultrasound energy is not high enough to weaken the Van der Waals forces between each interlayer, resulting in uniform micro-size flakes.

One of the PtS_2 micro-flakes was identified by the scanning transmission electron microscopy (STEM, JEM-2100F) as shown in Figure 19(a). A high resolution of the FETEM image of the micro-flake is shown in Figure 19(b), which illustrates a clear lattice fringe with an interplanar space of 0.303 nm. This is indicating an in-plane lattice constant of α = 0.350 nm, which is very close to the DFT value of 0.358 nm as reported in a recent literature [24].

Chemical compositions were characterized by X-ray photoelectron spectra (XPS, ESCALAB 250Xi, Thermo Fisher Scientific), shown in Figure 20, with achromatic 200W Al Kα as the X-ray source and the resolution of 0.10 eV. XPS spectra of core
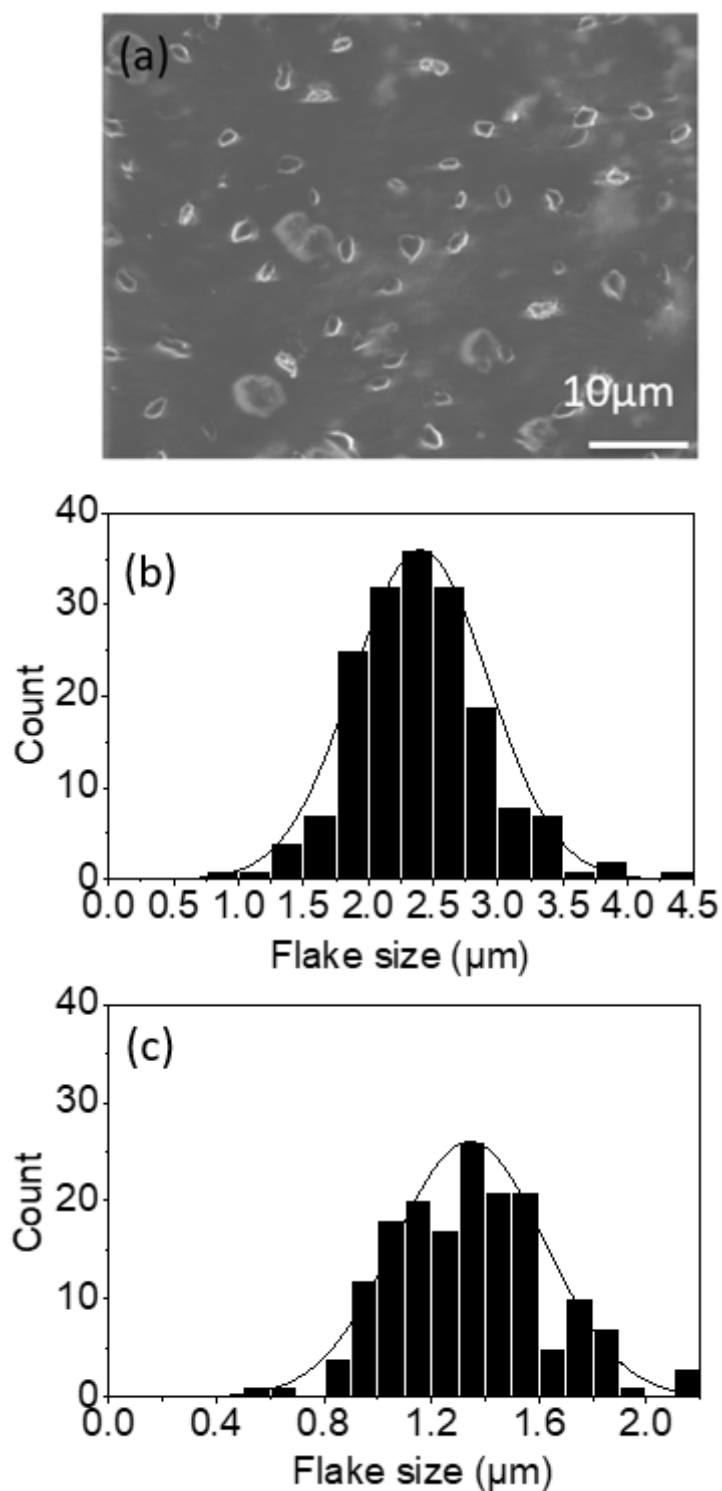
Figure 17 (a) SEM image of PtS$_2$ microflakes; and statics of SEM distribution of 170 flakes along the lateral dimensions for the (b) short axis and (c) long axis.
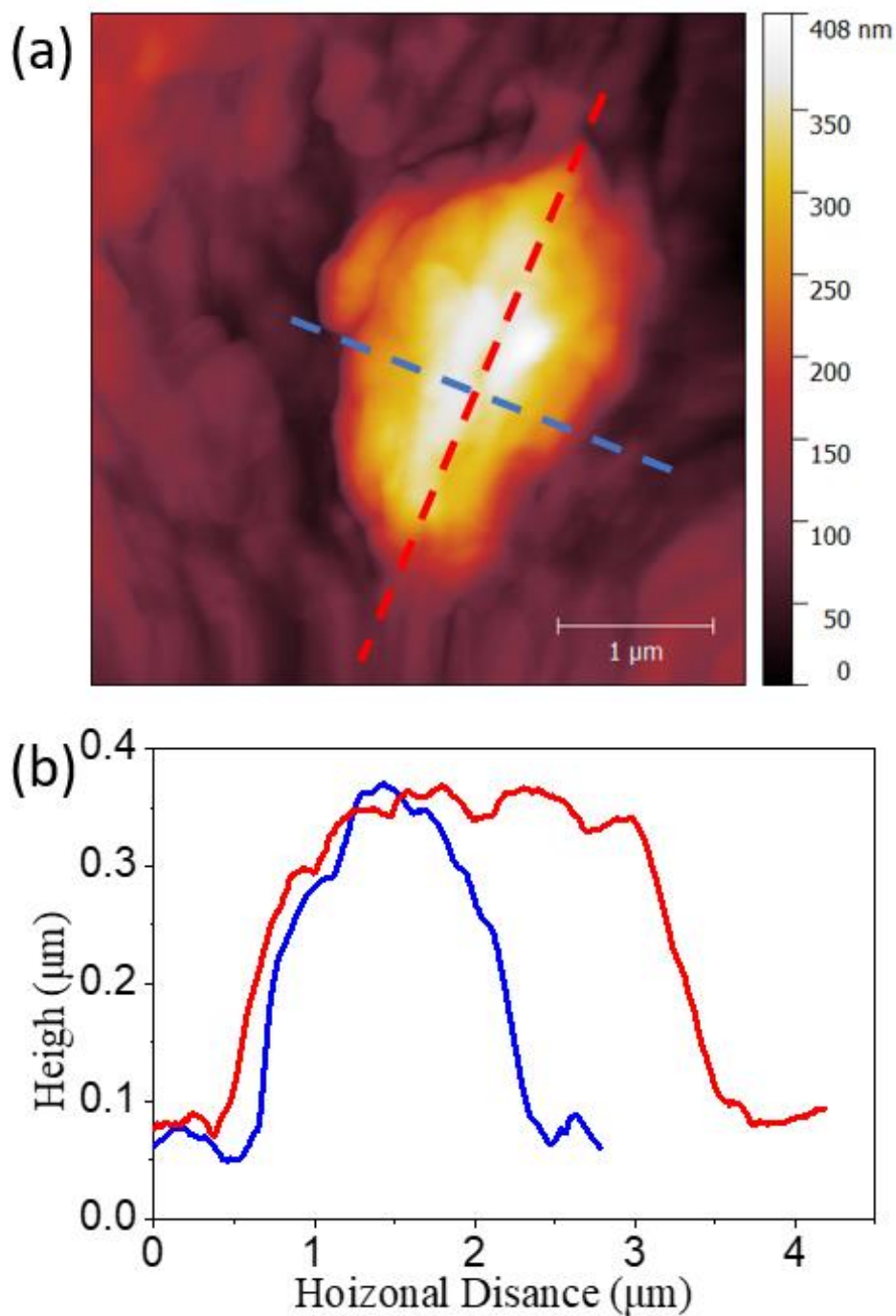
Figure 18 (a) Atomic force microscopy image of the prepared PtS$_2$ microflake on a quartz substrate. (b) The height profile measured along the blue and red lines shown in (a).

level Pt4f region and the core level regions for S2p are depicted in Figure 20(a) and 12(b), respectively. The predominant Pt state is identified to be Pt(II) at 72.58 eV and 75.92 eV. Peaks at 163.73 eV and 165.14 eV correspond to S2p3/2 and S2p1/2, respectively. Atomic percentages for Pt4f, S2p, and C1s are recorded as 15.01%, 26.05%, and 58.93%, respectively. The chalcogen-to-metal ratios are calculated to be 1.74, indicating a partial oxidization occurs on the surface of the sample. Oxidation may also appear during liquid exfoliation when bubbles meet the heated surfaces that are induced by violent vibration caused by sonication. The presence of considerable sulphate series in XPS spectrum of S2p leads to a major contribution of Pt(II) at the localized oxidation of the sample.

3.3 Laser experiment and results discussion

In order to test the nonlinear property of the fabricated PtS_2-SA, an Er-doped fiber laser with ring cavity was constructed. The cavity consists of a 0.7 m long Er-doped single mode fiber (LIEKKI™ Er110-4/125), a polarization-independent isolator, a 10% output coupler, and a polarization controller. The total cavity length is about 11.5 m. The 1 mm x 1 mm size PtS_2-SA was integrated into the cavity by sandwiching between the two FC/APC connectors as shown in Figure 21. The utilization of FC/APC connector instead of FC/PC was to eliminate the parasitic reflection and to maintain the stability of the Q-switched system opseration. A pure PVA thin film with the same thickness as the PtS_2-SA was integrated into the fiber laser system as shown in Figure 21 to serve it as a control experiment. In this setting, various pump power level and the polarization direction were adjusted to confirm that no mode

0.5 μm

$d=0.303n$

2 nm
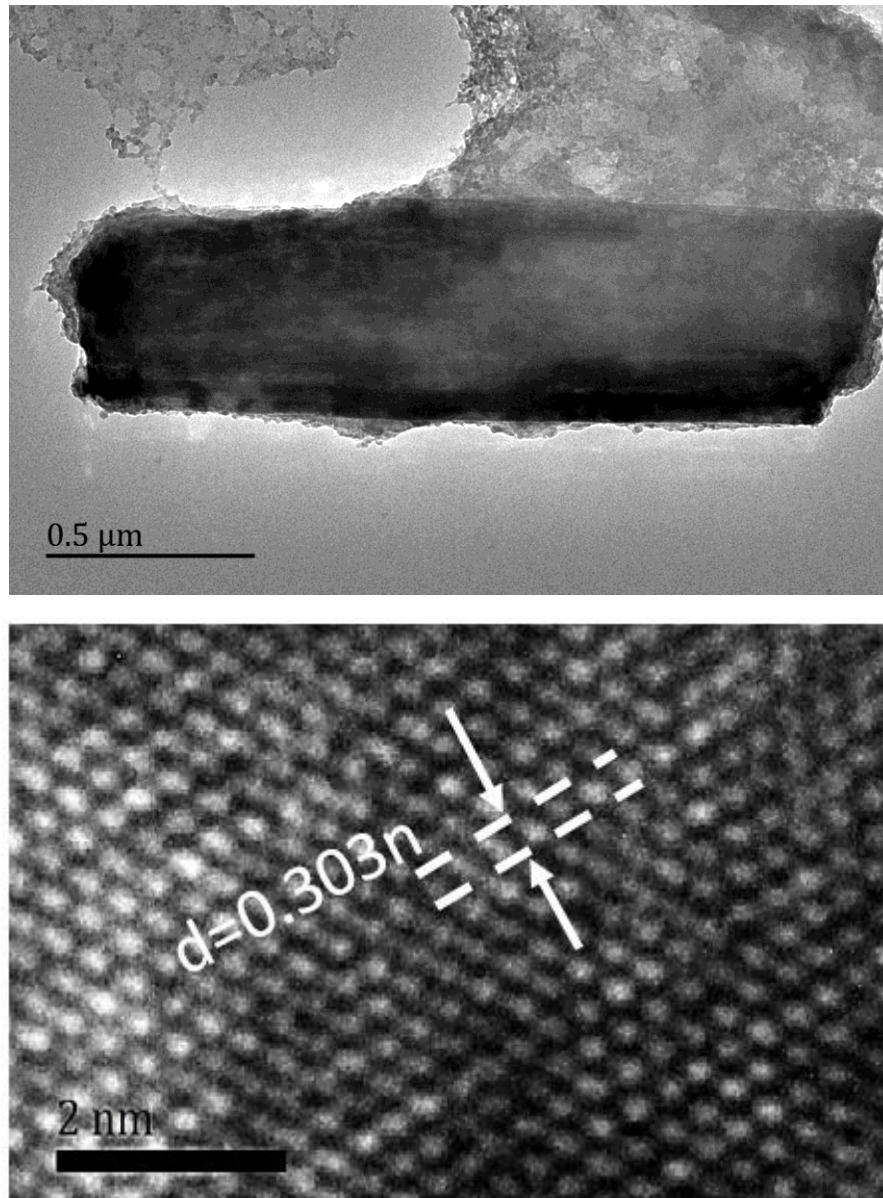
Figure 19 (a) FETEM image of a PtS$_2$ microflake, (b) High resolution TEM image of (a).

locking pulse is observed by using the pure PVA sample.

Then the pure PVA thin film in between the connector junctions was replaced by the fabricated PtS$_2$-SA. In this case, a stable pulse train was detected, when the pump power was scaled beyond 53 mW. The modulation range of the repetition rate and
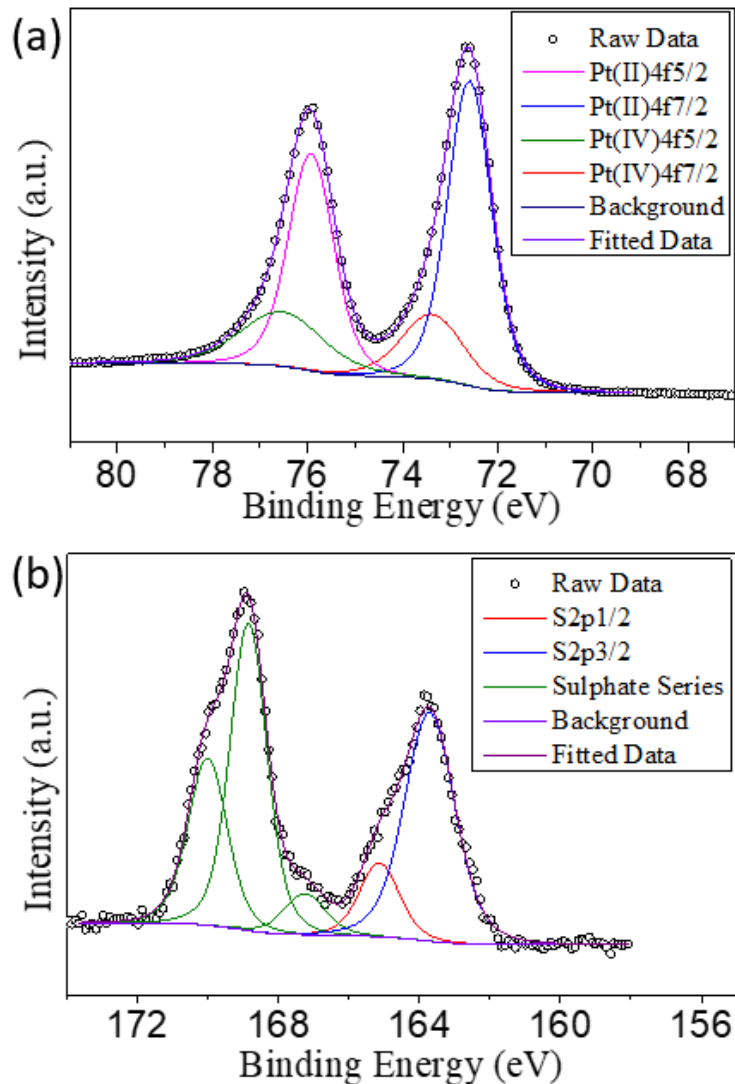
Figure 20 High resolution X-ray photoelectron spectra of the respective chalcogen for (a) PtS$_2$ (Pt4f region) and (b) PtS$_2$ (S2p region).

the full width at half maximum (FWHM) of the pulse duration were observed as 18.1 kHz - 24.6 kHz and 9.6 µs - 4.2 µs, respectively, by changing the pump and the output power as shown in Figure 22(a). The pulse duration can be further minimized by shortening the total cavity length [4] and enhancing the modulation depth of the PtS$_2$-SA.
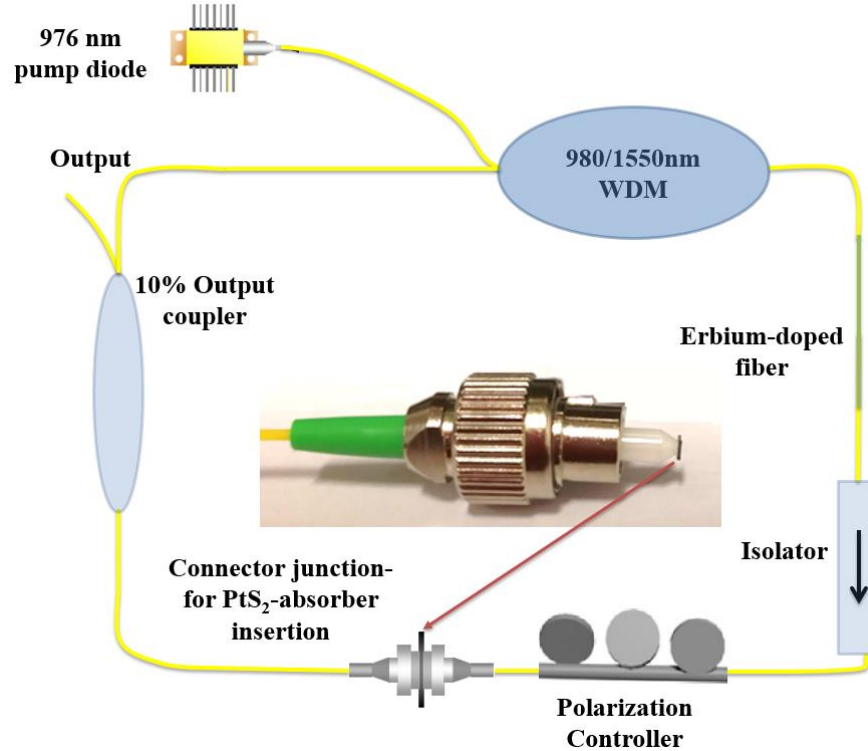
Figure 21 Schematic experimental set-up of the Q-switched Er doped fiber laser ring cavity.

The maximum achieved single pulse energy is 45.6 nJ with respect to 84 mW pumping power. The achieved pulse energy is comparable to those reported in Q-switched Er-doped fiber laser by using other 2D TMDs-SA such as WS_2 (46.3 nJ) [20] and MoS_2 (63.2 nJ) [212]. The corresponding pulse train, single pulse profile, and wavelength spectrum are shown in Figure 22(b)-22(d), respectively. Beyond this pumping power, the Q-switched operation became unstable and eventually vanished. This phenomenon may be due to the oversaturation of the PtS_2 saturable absorber and the instability of laser cavity in the high pump power [213]. A further modification of the cavity setting may further improve the stability of the laser and thus enhance the obtained maximum pulse energy and the peak power.
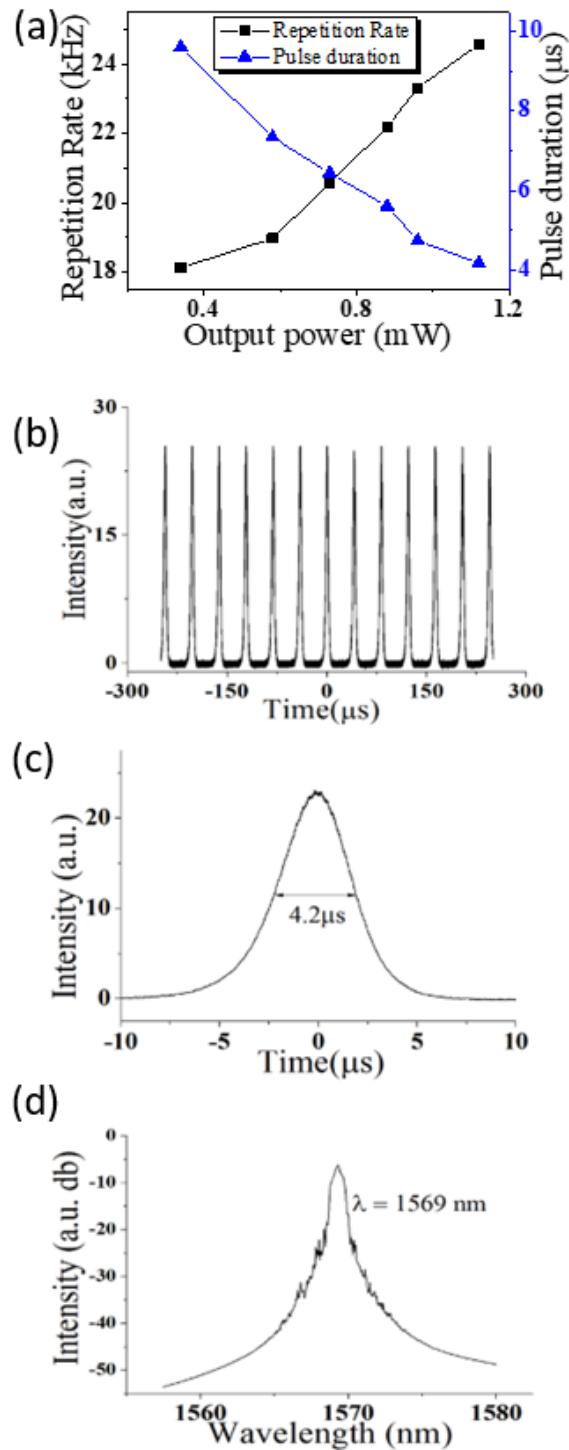
Figure 22 Q-switched laser characteristics: (a) Variation of repetition frequency and pulse duration with respect to different output power. (b) Pulse train, (c) Single pulse profile, and (d) Output spectrum of the output pulse energy of 45.6 nJ.

3.4 Conclusions

In this study, for the first time a Q-switched laser based on PtS_2 microflakes saturable absorber fabricated by low cost ultrasonic liquid exfoliation method was demonstrated. Stable 1569 nm Q-switching pulses were obtained from the laser system. The demonstrated pump power depending on the repetition rate and the pulse duration range are 18.1 to 24.6 kHz and 9.6 to 4.2 µs, respectively, with respect to pump power ranging from 53 mW to 84 mW. The maximum output power is about 1.1 mW. This work proves the potential of newly developed layered PtS_2 microflakes saturable absorber fabricated by low-cost ultrasound techniques for laser Q-switching applications.

Chapter 4 Fabrication of Luminescent PtS$_2$ Quantum Dots

4.1 Introduction

The discovering of Q-switching behavior of PtS$_2$ based SA arouses my interest to investigate other optical performances of this novel material. Photoluminescence (PL) plays a critical role in optical applications in development of displays, imaging, and bio-sensor. The photoluminescence of group-10 TMDs materials are rarely reported at present. Some frontiers admitted that the PL signal of PtS$_2$ monolayer "is too weak to be detected" [27].

Quantum dot (QD) is known with a definition: the materials size reaches to less than twice of its exciton Bohr radius. Due to strong quantum confinement effect and boundary effect, QDs show extremely large transition energy comparing to the layer or bulk counterpart, resulting in distinct enhancement in PL performances. Thanks to this fundamental understand, this work undertakes an enhancement to PtS$_2$'s PL performance by shrinking its size to QDs scale. The QDs are fabricated by a low-cost liquid exfoliation technique. The PL spectra are achieved and studied in association with QDs structures and chemical compositions.

4.2 Experimental Section

4.2.1 Materials Fabrication

PtS$_2$ QDs suspension was fabricated by high intensity ultrasonic liquid exfoliation

followed by dialysis shown in Figure 23. The 50 mg bulk PtS_2 powder (Alfa Aesar) was added into 250 ml of deionized (DI) water. Then the probe sonication (SCIENTZ-1200E, Ningbo Scientz Biotechnology Co., Ltd.) was conducted to the mixture under the power of 1200 W with 20 kHz below 27 °C for 12 hours, while an ultrasound probe time of 2 s at an interval of 4 s was maintained. Afterwards, a sonication bath with 40 kHz for 6 h was applied to the mixture and followed by centrifuging at 8000 rpm for 20 min to eliminate unexfoliated bulky PtS_2. The collected supernatant liquor was subjected to dialysis using a dialysis membrane (cut-off 3.5 kDa) for 24 h. The solution outside the dialysis membrane was taken as the PtS_2 QDs solution kept in ambient environment for several days, 3 months, and 6 months.
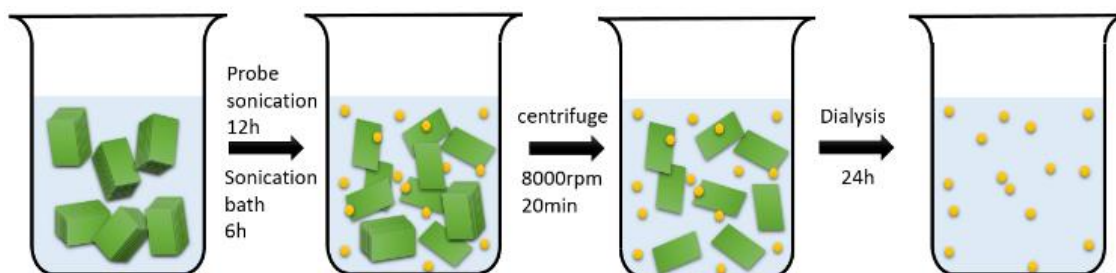
Figure 23 Schematic representation of the synthesis process of PtS_2 QDs.

4.2.2 Characterizations

The PL emission spectra of as-prepared PtS_2 QDs solution were recorded using Edinburgh CD920 on excitation at given wavelength. The measurement is conducted under room temperature by using Xenon lamp as excitation source. Time-Resolved measurements were monitored by HORIBA Fluorolog-3 spectrometer for ultrafast studies and time-correlated single-photon counting (TCSPC) accessory for lifetime determinations. UV-Vis absorption spectroscopy was conducted by Shimadzu UV-

2550. The PtS$_2$ QDs solution was contained in quartz cuvettes for PL and UV-Vis characterizations. The morphology and lattice fringes were observed by Scanning Transmission Electron Microscopy (STEM, Jeol JEM-2100F). The height information of PtS$_2$ QDs was measured by Atomic Force Microscopy (Bruker Nanoscope 8). The AFM sample was prepared by spin-coating the solution on the surface of quartz substrate followed by drying in the ambient laboratory condition. X-ray photoelectron spectroscopy (XPS, ESCALAB 250Xi, Thermo Fisher Scientific) was carried out to reveal the chemical composition with achromatic 200W Al Kα as the X-ray source and the resolution of 0.10 eV. The powder of the raw material was kept in the oven with 60 °C for 3 h for drying before conducting the XPS characterization.

4.3 Results and Discussion

In this work, PtS$_2$ QDs were fabricated by conducting ultrasonic exfoliation in DI water. The electrical energy in the equipment was firstly converted to mechanical energy via piezoelectric effect. When sonication probe introduces, an intense mechanical vibration is generated in liquid. As a consequence of that an acoustic energy is generated in the form of ultrasonic waves. The ultrasonic waves are strong enough to oscillate the liquid, resulting in the circulation of low and high pressure in DI water. In the period of rarefaction, many vacuum bubbles are generated within the mixture of DI water and PtS$_2$ powder attributing to the increase of molecular
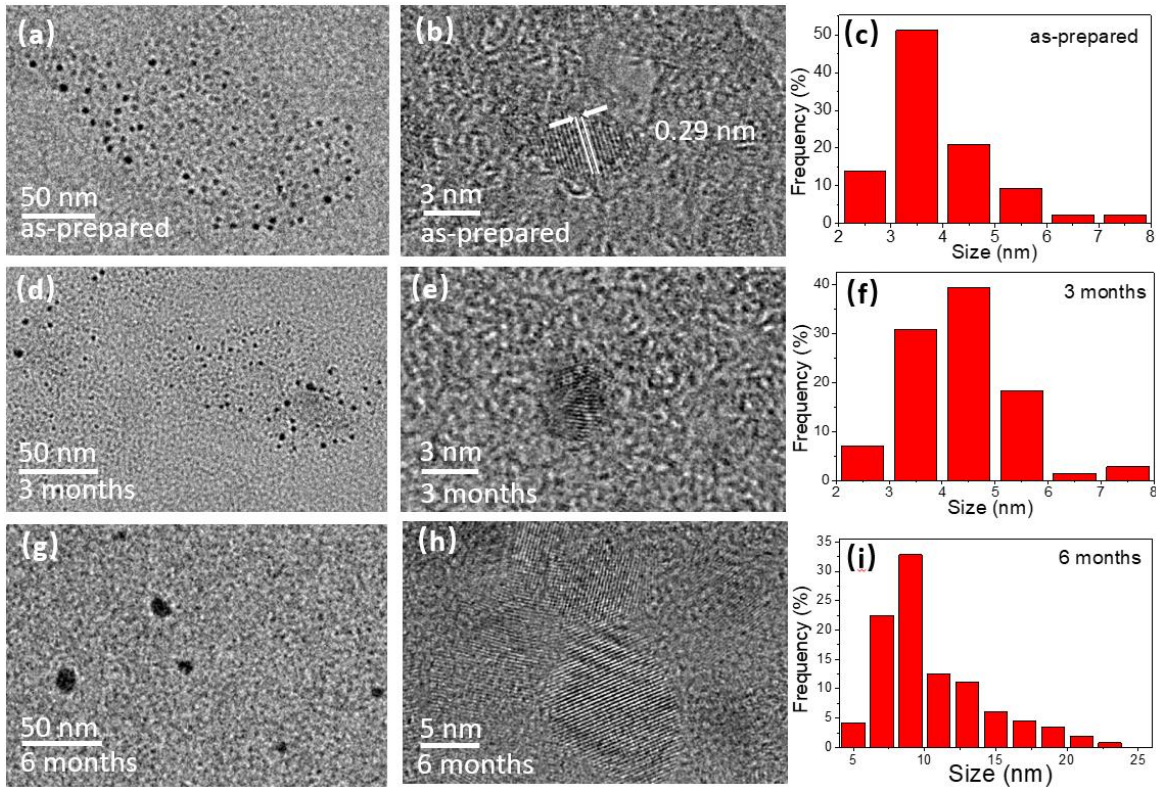
Figure 24 (a) TEM image of as-prepared PtS$_2$ solution; (b) High-resolution TEM image of a typical QD in (a); (c) Size distribution of PtS$_2$ QDs in (a); (d) TEM image of PtS$_2$ solution stored for 3 months; (e) High-resolution TEM image of a typical QD in (d); (f) Size distribution of PtS$_2$ QDs in (d); (g) TEM image of PtS$_2$ solution stored for 6 months; (h) High-resolution TEM image of a typical nanoparticle in (g); (i) Size distribution of PtS$_2$ nanoparticles in (g).

distance. When the rarefaction alternates with compression, those bubbles are intensely collapsed. Localized high temperature, high pressure and wild flow of liquid are induced accompanied by the implosion. This so called cavitation process offers massive kinetic energy to overcome Van der Waals force for decomposing and grinding the PtS$_2$ bulk powder into smaller particles and quantum dots counterpart [214], [215].
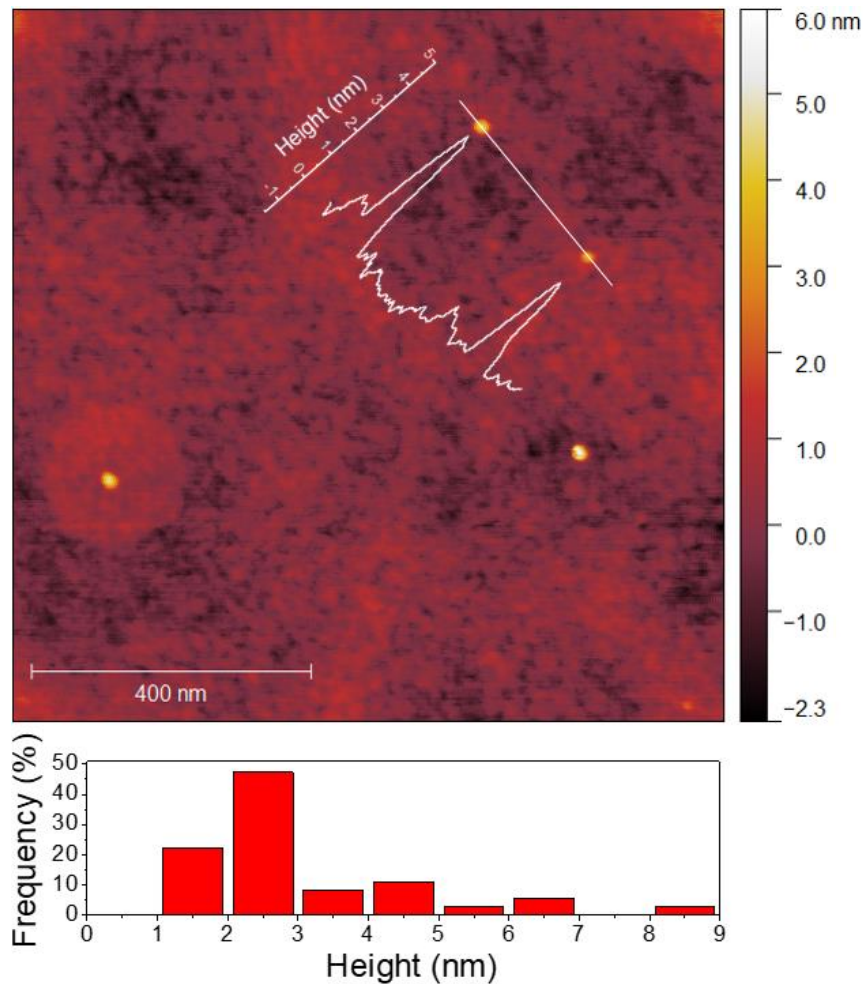
Figure 25 AFM image of as-prepared PtS$_2$ QDs, the height profile along the straight lines (inset), and the statics of height distribution.

The PtS$_2$ QDs are observed by TEM as shown in Figure 24. The as-prepared PtS$_2$ QDs and the statistics of size distribution are depicted in Figure 24(a) and 24(c) demonstrating an average diameter of 3.9 nm obtained by measuring 44 QDs. Figure 24(b) captured by a high-resolution of TEM shows the crystalline characteristic of a typical as-prepared QD with a diameter of 3.74 nm. The sharp lattice fringe with a 0.29 nm of interplanar spacing corresponding to the (001) planes

of PtS$_2$ [26], [27], indicating its single crystalline nature. After 3 months storage under ambient conditions, PtS$_2$ QDs remained the well-dispersive status in DI water as the TEM images shown in Figure 24(d) and 16(e). The average diameter among 43 QDs become 4.3 nm, shown in Figure 24(f), possibly due to PtS$_2$'s poor solubility in water. The significant size increase of PtS$_2$ nanoparticles was observed after 6 months storage as shown in Figure 24(g). By magnifying the scale to high resolution, Figure 24(h) can be obtained displaying several QDs agglomerate into one larger nanoparticle, which is counted as one particle for statistics of size distribution, shown in Figure 24(i). This increase of size may also because of restacking of the exfoliated nanoparticles to thicker ones by the Van der Waals forces. The average size of 44 nanoparticles is about 10.5 nm.

The as-prepared PtS$_2$ QDs were found scattering on the quartz substrate sample by conducting AFM measurement. The 1×1 µm^2 image of the substrate surface, the section analysis (inset), and the thickness analysis are presented in Figure 25. Two sharp signals of PtS$_2$ QDs can be recognized precisely along the section with height of 4.0 nm and 3.4 nm, respectively, suggesting they consist of 8 and 7 layers [27]. The average thickness of PtS$_2$ QDs is obtained to be 2.9 nm by measuring 36 QDs. By comprehensive analysis of size characteristics obtained by AFM and TEM, the intense ultrasonic energy is proved to be capable to weaken the Van der Waals force inside the particles and even break them into the form of nanoscale QDs.

The chemical composition in raw material of PtS$_2$ powder was investigated by XPS measurement, whereas the signal of as-prepared QD sample is too weak to be detected for its insufficient quantity in the solvent. As observed in XPS spectrum in

Figure 26 (a) and 26(b), the chalcogen in PtS_2 can be split peaks into 162.9 eV and 164.2 eV, respectively, arising from the S2p1/2 with lower binding energy and S2p3/2 with higher binding energy in spin-orbit splitting. On the surface of the sample, a part of S^{2-} in PtS_2 is transformed to sulphate series. The peak detected in Figure 26(b) at binding energy of 169.6 eV indicates that the sulphates may exist as forms of HSO_4^{-} or SO_4^{2-} [21,26]. These considerable sulphate series might produce compound such as $PtSO_4$, $Pt(HSO_4)_2 \cdot H_2O$ etc., which significantly contribute to the Pt(II), corresponding to Pt4f7/2 and Pt4f5/2 signals at 72.2 eV and 75.5 eV, respectively, on the surface of PtS_2. The predominant Pt(II) rather than Pt(IV) (at binding energy of Pt4f7/2 = 73.1 eV and Pt4f5/2 = 76.5 eV) and the presence of sulphate series illustrate the phenomenon of partial oxidation on the surface of the sample during the drying process.   The atomic percentages deduced from XPS test were determined to be 15.01% and 26.05% for Pt4f and S2p, respectively, from the integrated areas of their peaks. The stoichiometric ratio of S2p to Pt4f is less than the expected value of 2. This deviation may attribute to the absence of chalcogens due to yielding the sulphate series by cause of oxidization.

The PL spectra of the PtS_2 QDs samples were measured under various excitation wavelengths. Figure 27(a) presents the emission spectra of as-prepared PtS_2 QDs sample. The red-shifts of emission peaks ranging from 395.7 nm to 464.4 nm account for increasing excitation wavelength from 300 nm to 390 nm. This excitation-dependent luminescent property has also been reported on various types of QDs such as carbon QDs [216], [217], alloying inorganic semiconductor QDs [218], [219], and traditional TMDs QDs [39], [40]. The mechanism attribute to the size effect on

the band gap energies of the QDs. Excited by Xenon arc lamp, the smaller QDs with

wider band gap emit at shorter wavelength while the larger QDs with narrow band

gap emit at longer wavelength, indicating the poly-dispersity characteristic of this

PtS$_2$ QDs sample. The excitation wavelength versus the peak position of emission

is illustrated in Figure 27(d). This figure explains that the as-prepared QDs
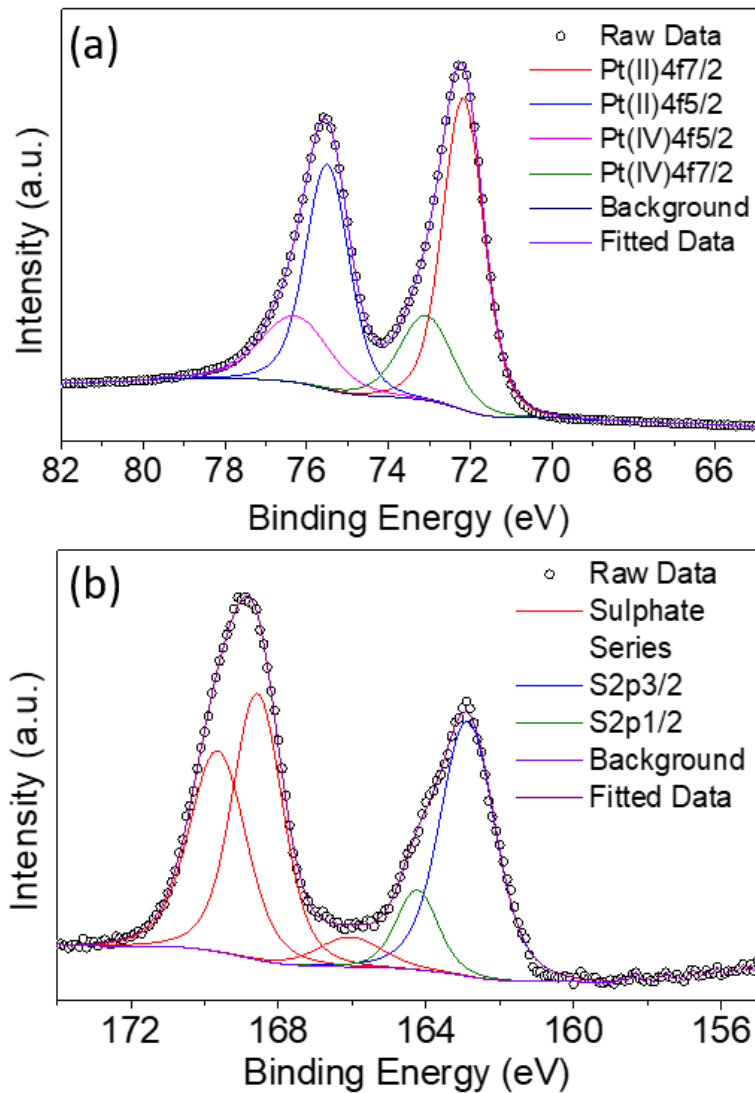
Figure 26 High resolution X-ray photoelectron spectra of PtS$_2$ for (a) Pt4f region and (b)

S2p region.
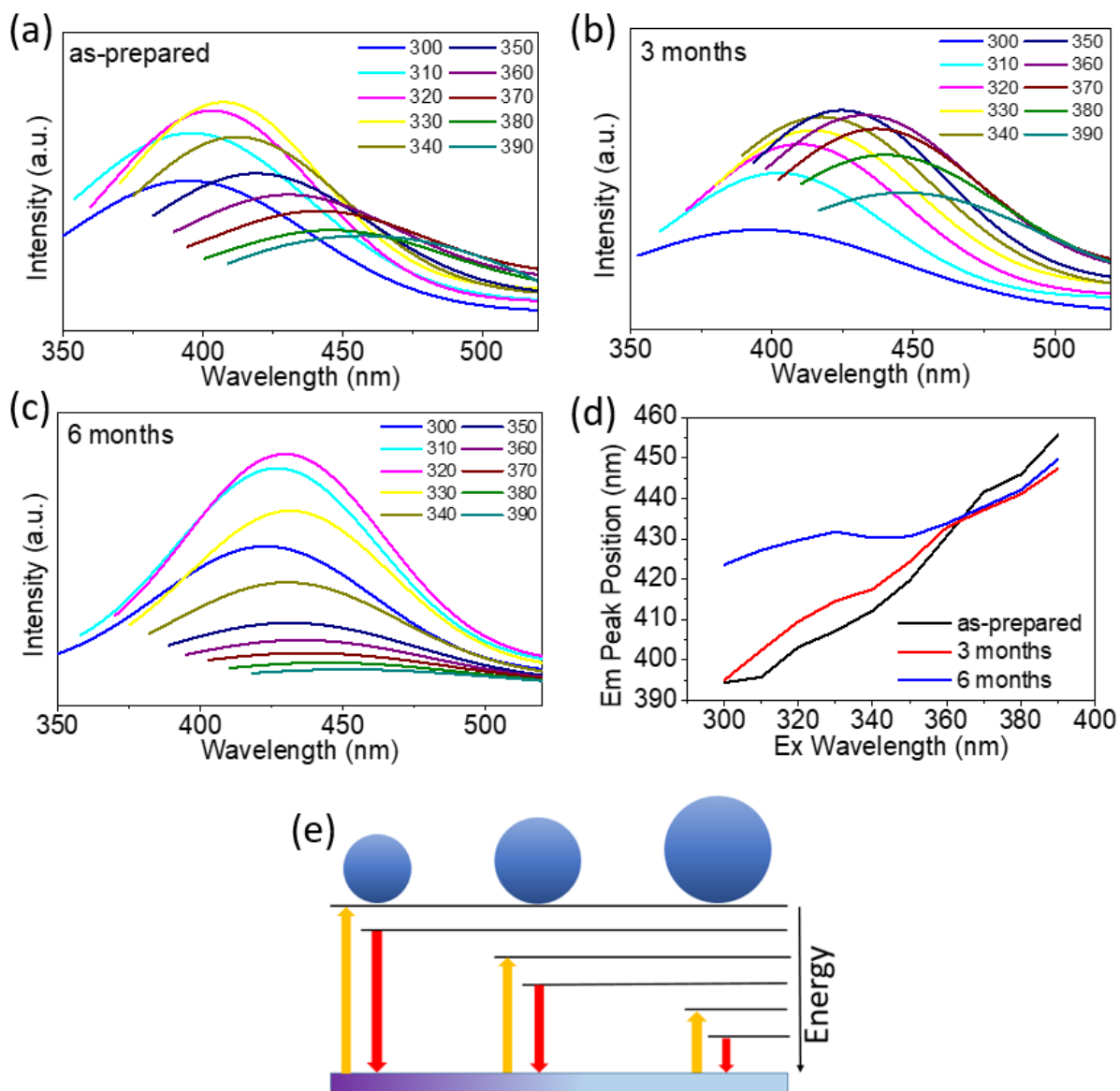
Figure 27 (a) Emission spectra of as-prepared solution; (b) Emission spectra of solution stored for 3 months; (c) emission spectra of solution stored for 6 months; (d) Emission peak positions according to the excitation wavelengths; (e) Diagram of quantum size effect.

suspension exhibits a linear behavior, attributing to the quantum size effect which is schematically explained in Figure 27(e), that the bandgap energy is dependent on the size of QD. The consistency of emission wavelengths provides the evidence of quantum confinement effect. The observed luminescent intensity keeps increasing during the red-shift of excitation wavelength starting from 300 nm and reaches to the maximum signal of 407.2 nm excited at 330 nm. Photoluminescence excitation (PLE) spectrum for the highest emission peak occurring at 407.2 nm wavelength was depicted in Figure 28. The excitation peak appearing at 328.5 nm wavelength can be considered as major contributor to 407.2 nm emission wavelength. The UV-Vis spectrum of PtS_2 QDs solution was scanned and included in Figure 28 as well. The absorbance curve displays an absorption peak at 271.5 nm. The weak absorption trend appears between 311-387 nm might attribute to nanoparticles in larger scales.

This excitation wavelength dependent behavior may also due to various pathways including but not limited to poly-dipersity. Förster resonant energy transfer (FRET), as a result of re-absorption between neighboring QDs, can be responsible for the red-shift of the spectrum [220]. Another scenario would account for the excitation wavelength dependence could be the fickle surface morphology of the quantum dots. After absorption process, the charges will be separated and trapped at surface locations. A recent work reported that the radiative recombination of these charges, governed by radiative rates, differ from various surface structure of quantum dots [221]. The inhomogeneous distribution of absorption spectrum reflected increasing radiative rates and at higher-energy and decreasing radiative rates at lower-energy

in Figure 28, agreeing with the fact in Figure 27 that the PL emissions intensity increases from shorter wavelength and decreases from a certain wavelength to longer wavelength. The energy transfer in functional groups may also alter the emission spectrum [222]. Since the raw materials is pure PtS_2, and the solvent is DI water, the functional groups are assumed to play a minor role to the influence of emission spectrum in this work.

A 0.73 eV stokes shift is observed for 328.5 nm excitation wavelength and the 407.2 nm emission wavelength. Such large value might due to the quantum confinement effect, which leads to interaction between discrete levels of electron and hole. The spatial overlaps for wave functions of electron and hole increase dramatically when the materials sizes decrease to QD scale [223]. Therefore, the fine structure splitting between the lowest active singlet excitonic states and passive triplet states are much larger than its layer or bulk counterpart [223], [224]. Deexcitation, which origins when rapid thermalization takes place from higher active energy states to passive triplet states, results in a red shift of emission spectra. As a consequence, it yields a larger stokes shift. The environment might also take account for the stokes shift. Since water is polar solvent, it can reorient the excited state dipole of quantum dots, which leads to lower energy and red shifts of emission wavelength. This so called solvent relaxation might lead to substantial stokes shifts [200]

As shown in Table 3, the PL Quantum Yield (QY) of PtS_2 QDs was estimated to be 1.28% by comparing the emission peak occurring at 407.21 nm and absorbance of as-prepared sample with the reference 1,8-ANS of known QY (0.0032) [225]. The

1,8-ANS was dissolved in water. Since the solvent of PtS_2 QDs is water as well, the refractive index of the sample and the reference can be considered to be equal, and the value is 1.33. The QY for the PtS_2 QDs sample can be calculated as Equation 1.

$$QY = QY_{ref}\frac{\eta^2}{\eta_{ref}^2}\frac{I}{I_{ref}}\frac{A_{ref}}{A} \tag{1}$$

where QY_{ref} is the quantum yield of the reference compound, η is the refractive index of the solution, I is the integrated emission intensity and A is corresponding to the absorbance of the sample and the reference.

Table 3 Quantum Yield of PtS_2 QDs.

Sample	I	Absorbance	η	QY
1,8-ANS	97.2924	0.87011	1.33	0.0032 [225]
PtS_2 QDs	97.9681	0.21925	1.33	0.0128

The long-term PL stability of PtS_2 QDs are monitored at stage of 3 months and 6 months stored under ambient conditions, shown in Figure 27(b) and 27(c). To illustrate the difference of the emission peak positions of the three samples, emission peak wavelengths are plotted against the excitation wavelengths shown in Figure 27(d). The emission peak was red shifted significantly from 394.4 nm and 395 nm representing for as-prepared sample and 3 months sample, respectively, to 423.6 nm for 6 months sample under 300 nm of excitation wavelength. The 390 nm of excitation wavelength gives emission peaks at 455.7 nm, 447.3 nm, and 449.7 nm
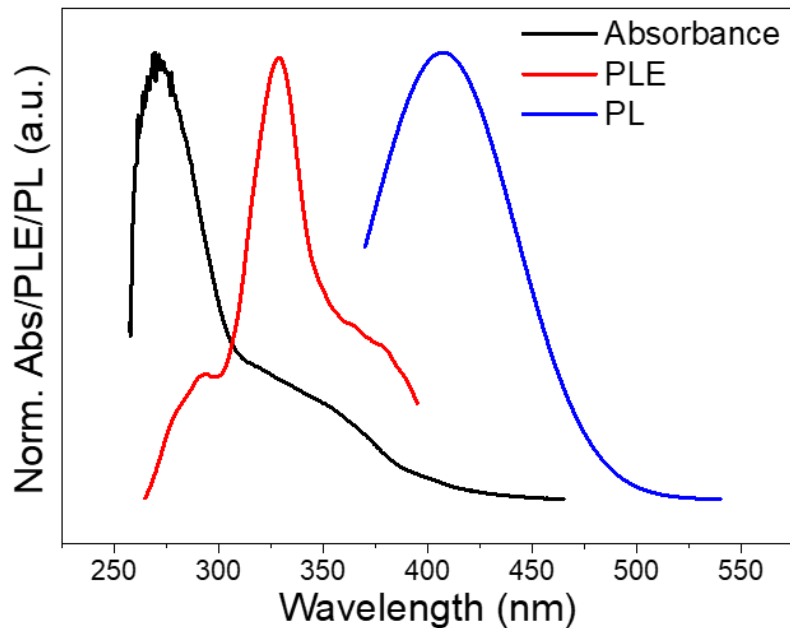
Figure 28 Normalized Absorbance spectrum (black curve), Photoluminescence excitation spectrum (red curve), and Photoluminescence spectrum (blue curve) for the highest emission peak occurring at 407.21 nm of as-prepared sample.

for as-prepared, 3 months, and 6 months sample, respectively. These results indicate 61.3 nm, 52.3 nm, and 26.1 nm emission peak positions shifted for 3 samples mentioned above, respectively, when the excitation wavelength was tuned from 300 nm to 390 nm. The emission peak excited under 300 nm wavelength and smaller range of emission peak shifted for the 6 months sample represent its weaker excitation-dependent property compared with the as-prepared and 3 months samples. These results agree well with the size of nanoparticle shown in Figure 24. The strong excitation-dependent property of 3 months sample shows well-dispersive status of QDs in the solution according to the quantum size effect. The weak excitation-dependent property of 6 months sample indicates that large nano-

particles started to dominate the PL process instead of small QDs. Even though showing weak excitation-dependent property, the sample still exhibit PL signals enduring 6 months exposure to the ambient conditions. This evidence the decent long-term stability of PtS_2's PL nature.

4.4 Conclusions

In summary, the fabrication of PtS_2 QDs suspension via a low-cost liquid exfoliation technique was demonstrated for the first time and the PL signals of PtS_2 QDs were clearly observed. The statistics of QDs illustrates an average dimension of 3.9 nm diameter with 2.9 nm thickness. The as-prepared PtS_2 QDs produce the maximum luminescent emission peak with a wavelength of 407.2 nm under the excitation wavelength of 328.5 nm. The excitation dependent luminescent property and size distribution of QDs confirm the quantum confinement effect. The great long-term stability of PtS_2 QDs may benefits prospective optics application. These findings indicate a promising future for luminescence applications.

Chapter 5 Photoluminescence of Group-10 Transitional Metal Dichalcogenides (PtS$_2$, PdS$_2$, and PdSe$_2$) Quantum Dots

5.1 Introduction

Achieving PL spectra of PtS$_2$ QDs opens a gate for my following study. Many group-10 TMDs materials exhibit layer-dependent tunable band gap, which benefits several advancing applications. For instance, PtSe$_2$ exhibits a tunable band gap from 0 (bulk) to 1.2 eV (monolayer) and performs well in photodetectors [25], [52]; PdS$_2$, shows an indirection band gap from metallic to 1.0 eV when the thickness shrinks from bulk to monolayer, benefiting logical junction [54], [226]; and PdSe$_2$ shows metallic similar to PdS$_2$ for bulk structure, while 1.31 eV for monolayer, leading to promising properties in application of FET and photodetector [55], [227]. Different from the deep understanding of their electrical properties, the optical behaviors, especially PL, still remain obscure yet. The tunable band gap may also benefit their optical properties thanks to quantum confinement effect when shrinking to QDs scales.

Learning from the previous PL study of PtS$_2$ QDs, the yield and dispersity of QDs require improvement. In this work, 3 typical group-10 TMDs, PtS$_2$, PdS$_2$, PdSe$_2$, QDs are fabricated by liquid exfoliation with NMP solvent in order to solve the previous issues. The characterizations of their morphologies, crystal structures, absorptions, and emissions are collected and analyzed for investigating their PL nature.

5.2 Experimental section

5.2.1 Materials Fabrication

In this study, PtS_2, PdS_2, and $PdSe_2$ QDs were fabricated via liquid exfoliation from their bulk powder raw materials. NMP was selected to be the solvent for its compatible surface energy, resulting in stabilizing and preventing TMDs nanoparticles from agglomeration. In the first step of the fabrication process, a 50 mg of PtS_2 raw material (Alfa Aescar) was poured into 250 mL of NMP solution. Next, a probe sonication was applied to the mixture under 250 W power with 20 kHz frequency for about 3 hours long, while 27 °C temperature was maintained throughout the process. In this case, the operation time of ultrasonic probe was set to 2 s at an interval of 4 s. Then, 2/3 of dispersion close to the liquid level was taken and stirred for 6 h under 140 °C. The supernatant liquor was obtained by centrifugation at 2000 rpm for 5 min to separate QDs from bulky raw materials. This QDs as-prepared solution was taken for the experiments and characterizations.

5.2.2 Characterization

The high-resolution images and lattice fringes of as-prepared QDs were observed via Scanning Transmission Electron Microscopy (STEM, Jeol JEM-2100F). The thickness of QDs was scanned under tapping mode with the aid of Atomic Force Microscopy (AFM, Bruker Nanoscope 8). Each of the AFM samples for QDs were prepared via drop casting the as-prepared QDs solution on the surface of quartz substrate followed by drying under 80 °C in the air atmosphere. Chemical

composition of raw materials was detected by X-ray photoelectron spectroscopy (XPS, ESCALAB 250Xi, Thermo Fisher Scientific) with achromatic 200W Al Kα as the X-ray source and the resolution of 0.10 eV. Before conducting the XPS measurement, the powders of raw materials were utilized to eliminate water in the oven under 60 °C for 3 h. The PL measurement was performed with Edinburgh CD920. The emission spectra of QDs solution were monitored on excitation at given wavelength under ambient environment. The excitation source was Xenon lamp. Time-Resolved measurements were monitored by HORIBA Fluorolog-3 spectrometer for ultrafast studies and time-correlated single-photon counting (TCSPC) accessory for lifetime determinations. UV-Vis absorption spectroscopy was recorded by Shimadzu UV-2550.

5.3 Results and discussion

Figure 29 is an illustration of STEM images for PtS_2 PdS_2, and $PdSe_2$ group-10 TMDs materials QDs. The STEM samples were prepared by drop-casting as-prepared PtS_2, PdS_2, and $PdSe_2$ QDs suspensions on holey copper grid, followed by a drying process in the ambient environment under 60 °C for 1 h. The morphologies and scattered distributions of PtS_2, PdS_2, and $PdSe_2$ QDs can be clearly observed from

Figure 29(a), 29(b), and 29(c), respectively. The statics of the corresponding size distributions are depicted in

Figure 29(g), 29(h), and 29(i) for number of 143 PtS_2, 104 PdS_2, and 106 $PdSe_2$ QDs,

respectively, pronouncing a statistical estimation of their average diameters of 4.73, 4.99, and 4.17 nm. High resolution images of PtS_2, PdS_2, and $PdSe_2$ QDs were captured in

Figure 29(d), 29(e), and 29(f), respectively, indicating the high crystallinity of the as-prepared samples. The interplanar spacing of 0.29 nm for PtS_2 QDs as observed in

Figure 29(d) is corresponding to (100) plane [26], [27]. For the PdS_2 QDs with a determined lattice distance of 0.27 nm is corresponding to the (200) plane, which agrees well with a simulated data as recently reported in the literature [226]. Then the $PdSe_2$ QDs shows a 0.27 nm lattice periodicity that matches its (200) crystalline plane [228]. The results imply that the ultrasonic energy is sufficient to separate layered group-10 TMDs materials from the Van der Waals forces and even split them into nanoscales. Thanks to outstanding stability of group-10 TMDs materials, which allows to obtain good crystallinity in the materials. Further investigation on QDs' height profiles and height distributions were conducted via AFM measurement as shown in Figure 30. The QDs were scattered on the quartz substrates by scanning processes. The scan size was set to be 1×1 μm^2 and the observation of QDs was taken place randomly on the substrates. The height variation of PtS_2, PdS_2, and $PdSe_2$ QDs can be clearly distinguished along line profiles as depicted in Figure 30(a), 30(b), 30(c), respectively. The average height of 38 PtS_2 QDs is determined to be 2.82 nm, suggesting 5 to 6 layers' thickness [27], and their height distribution is depicted in Figure 30(d). The statics of 54 PdS_2 QDs are shown in Figure 17(e), indicating an average height of 2.61 nm, which can be considered as 6 to 7 layers

[229]. The height information of 25 observed $PdSe_2$ QDs is recorded in Figure 30(f). The thickness of such QDs are assumed to be 4 to 5 layers referring to 1.99 nm average height [229].
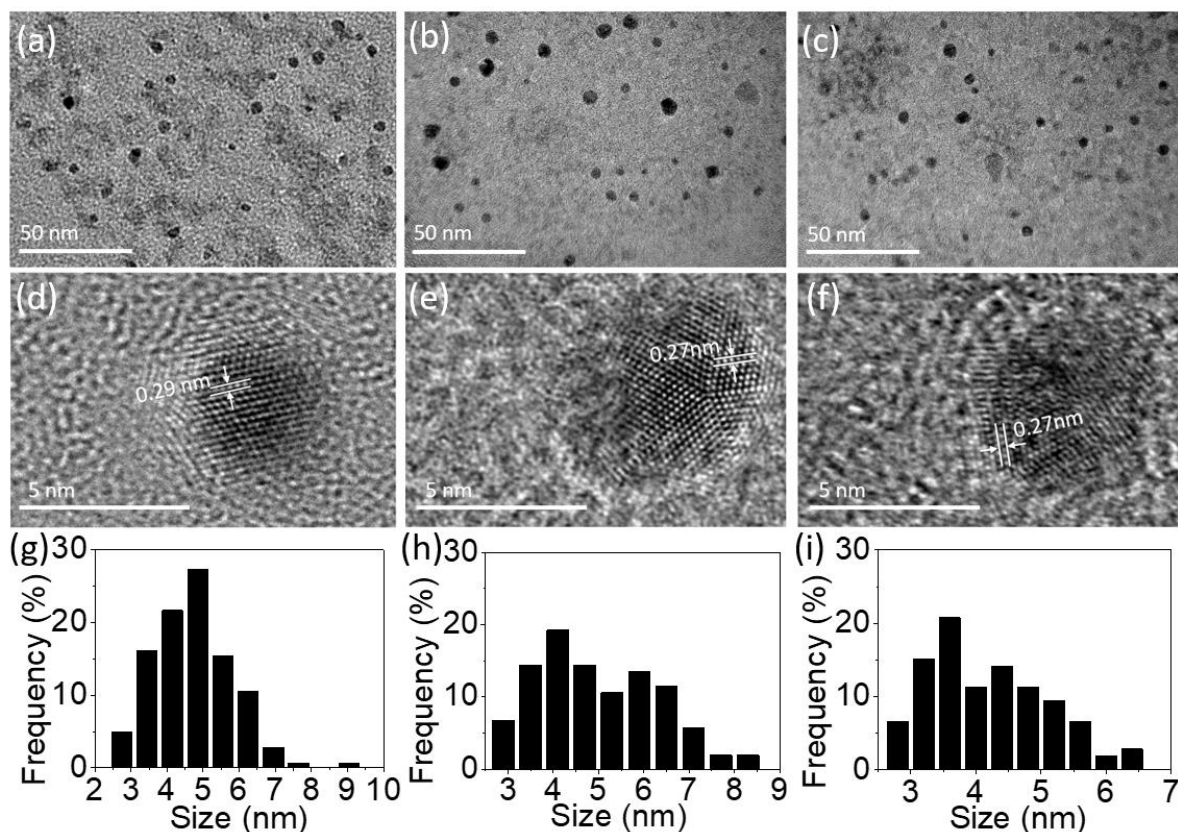
Figure 29 STEM images of (a) PtS_2 QDs solution, (b) PdS_2 QDs solution, and (c) $PdSe_2$ QDs solution; High resolution STEM images of a typical (d) PtS_2 QD, (e) PdS_2 QD, and (f) $PdSe_2$ QD; Size distributions based on multiple images of (g) PtS_2 QDs, (h) PdS_2 QDs, and (i) $PdSe_2$ QDs.

Due to the scarce quantity in the solutions, the signals of QDs were difficult to be detected. Therefore, the XPS measurement was conducted on the raw powder materials counterparts in order to investigate their chemical compositions as shown

in Figure 31. For Pt4f spectra of PtS$_2$, deconvolution of the line shape reveals two doublets, Pt^{2+} and Pt^{4+}, essential to reconstruct Pt signals, as shown in Figure 31(a). Pt^{2+} with level positions of Pt4f7/2 and Pt4f5/2 are fitted at 71.98 eV and 75.38 eV, along with Pt^{4+}4f7/2 and Pt^{4+}4f5/2 fitted at 71.98 eV and 75.38 eV, respectively. S2p deconvolution as shown in Figure 31(b) can be conducted showing one doublets: S2p3/2 at 162.78 eV and S2p1/2 at 164.18 eV. The signal with 168.08 eV binding energy refers to sulphate series constituting HSO^{4-} or SO$_4^{2-}$ [49], [230]. Such considerable intensity of sulphate signal indicates partial oxidation on the surface of the PtS$_2$ raw materials, resulting in Pt^{2+} as predominant doublet. The atomic percentage of Pt and S is determined to be 17.79% and 27.97%. The stoichiometric ratio is obtained as less than 0.5, which may be due to the origination of sulphate series from surface oxidation during drying process. For PdS$_2$, signals of Pd3d5/2 and Pd3d3/2 are shown in Figure 31(c) with binding energies of 336.08 eV and 341.38 eV. The S2p spectra for PdS$_2$ can be divided into two chemical states [231] as shown in Figure 31(d). For the case of PtS$_2$ raw materials, S(I)2p3/2 and S(I)2p1/2 are simulated at 161.08 eV and 163.38 eV, while S(II)2p3/2 and S(II)2p1/2 with 162.28 eV and 164.38 eV exhibit similar to the S2p spectra. The absence of sulphate series in PdS$_2$ is caused may be due to the fact of its distinguished stability. The atomic percentage of Pd and S are found to be 3.08% and 6.96% on the surface, exhibiting a stoichiometric ratio very close to ½ due to probably the absence of oxidation. The level positions of Pd3d5/2 and Pd3d3/2 in PdSe$_2$ with 336.18 eV and 341.48 eV as depicted in Figure 31(e) agree well with the presence of Pd signals in PdS$_2$. The deconvolution of Se element gives rising to Se3d5/2 signal at 54.18 eV

and Se3d3/2 signal at 54.98 eV as shown in Figure 31(f). The atomic percentage of

6.76% and 15.11% for the Pd and Se elements support the idea of air stability as

recently reported in the literature [47].
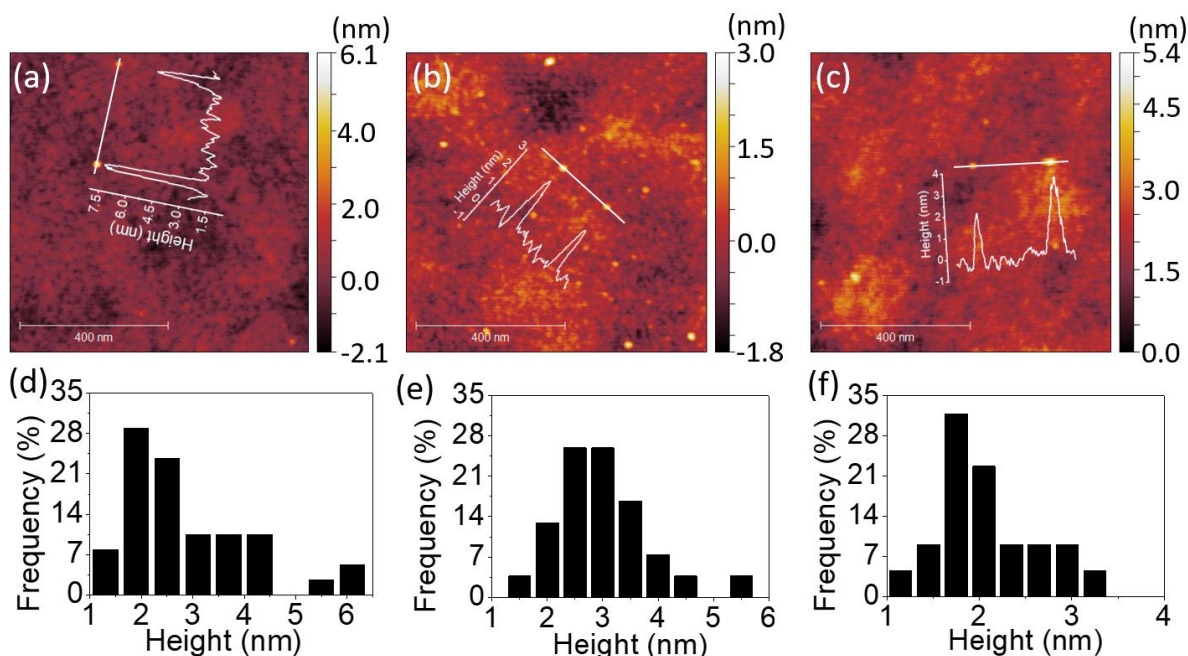
Figure 30 Line profiles and corresponding AFM images of (a) PtS_2 QDs, (b) PdS_2 QDs, and (c) $PdSe_2$ QDs; height distributions based on several images of (d) PtS_2 QDs, (e) PdS_2 QDs, and (f) $PdSe_2$ QDs.

The PL emission spectra of PtS_2, PdS_2, and $PdSe_2$ QDs show excitation wavelength-dependent behaviors, i.e. the wavelength of PL emission peak red-shifts under crescent excitation wavelength, which have been widely reported by several studies on semiconductor QDs [218], [219], traditional TMDs QDs [39], [232], and carbon QDs [217], [233]. Due to quantum size effect, the poly-diversity of QDs sizes give rising to the variation of band gap energies. The larger QDs exhibit lower band gap energies, and vice versa. The PtS_2 QDs sample exhibits PL peak wavelength

ranging from 381.5 to 548 nm while excitation wavelength shifts from 300 nm to 480 nm as shown in Figure 32(a). The maximum emission peak could be found at 468.5 nm for the excitation wavelength of 380 nm. The PL spectra of PdS_2 QDs as shown in Figure 32(b) were observed from 400 nm to 567 nm under the excitation ranging from 320 nm to 480 nm. The highest PL peak is determined to be 491 nm for the excitation wavelength of 400 nm. The PL spectra of $PdSe_2$ are depicted in Figure 32(c), displaying emission peaks ranging 379 nm to 551 nm, while the excitation wavelength was being tuned from 300 nm to 480 nm. The 340 nm excitation wavelength presents a maximum emission peak at 413 nm. It is noteworthy that the sharp peaks occurring at 450 nm for all spectra are possibly due to the presence of NMP solvent, which is excluded from this QDs' PL analysis. The maximum emission peak wavelengths demonstrate a trend of $PdSe_2$ QDs < PtS_2 QDs < PdS_2 QDs, which might be owing to including but not limited to their intrinsic chemical property. This PL emission peak trend also accords with their average sizes determined via STEM characterizations, which may further prove the quantum size effect.

The absorption spectra are depicted in Figure 33 with black lines. The distinct absorption peaks at 307, 330, and 274 nm can be observed in Figure 33(a), 33(b), and 33(c) for the solutions of PtS_2, PdS_2, and $PdSe_2$ QDs, respectively. The maximum emission peaks (in blue lines) for all QDs samples and their corresponding photoluminescence excitation (PLE) spectra (in red line) are also displayed in Figure 33. The maximum emission peak for PtS_2, PdS_2, and $PdSe_2$ QDs samples exhibit at 377, 397.5, 346 nm as shown in Figure 33(a),33(b), and 33(c), respectively. These
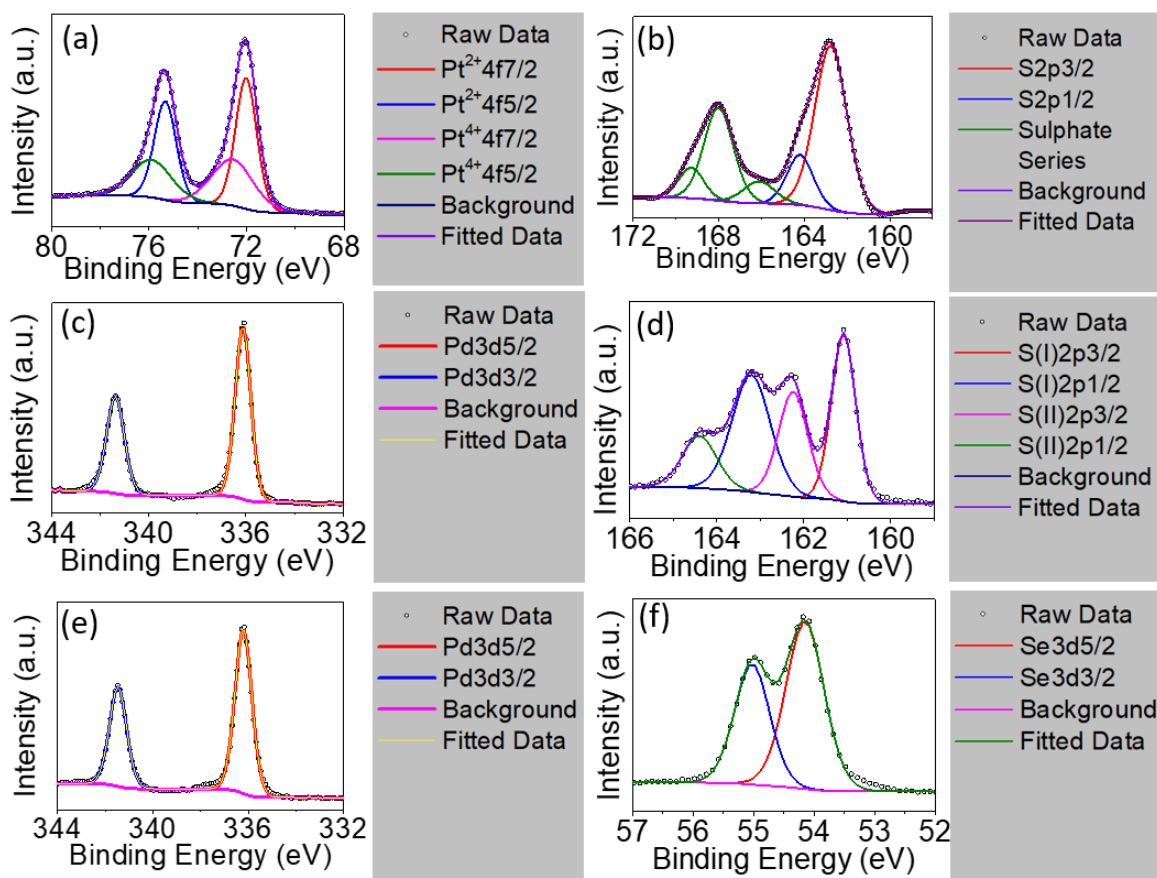
Figure 31 High resolution X-ray photoelectron spectra of PtS$_2$ for (a) Pt4f region and (b) S2p region; PdS$_2$ for (c) Pd3d region and (d) S2p region; PdSe$_2$ for (e) Pd3d region and (f) Se3d region.

PLE peaks agree well with the previous PL emission analysis, implying to 0.64 eV, 0.59 eV, and 0.58 eV stokes shifts for the PtS$_2$, PdS$_2$, and PdSe$_2$, respectively. Such large stokes shifts are caused by the quantum confinement effect when materials size approaches to the atomic scale, resulting in dramatic expansion of spatial overlaps for electron-hole wave functions [234]. The splitting of the lowest singlet fine structure states and highest triplet states grows much larger comparing to their layers or bulky structure [224], [234]. The dark exciton ensues when excitation

Table 4 Quantum yields of PtS$_2$ QDs solutions PdS$_2$ QDs solution, and PdSe$_2$ QDs solution.

	A	I	η	QY	
1,8-ANS	0.60	97.29	1.33	0.32%	[225]
PtS$_2$ QDs	0.39	137.80	1.47	0.78%	This study
PdS$_2$ QDs	0.65	141.24	1.47	0.47%	This study
PdSe$_2$ QDs	0.04	149.43	1.47	8.69%	This study

experiences a rapid thermalization process from active singlet state to passive triplet state, leading to red shift of PL emission spectrum and larger stokes shift. QY of PtS$_2$, PdS$_2$, and PdSe$_2$ QDs are evaluated to be 0.78%, 0.47%, and 8.69%, respectively and tabulated in Table 4, while QY of 0.32% along with absorbance and emission data of 1,8-ANS is used as a reference [225]. The PL QY for as-prepared QDs samples are calculated by Equation 2.

$$QY = QY_{ref} \frac{\eta^2}{\eta_{ref}^2} \frac{I}{I_{ref}} \frac{A_{ref}}{A} \qquad (2)$$

Where, η represents the refractive index of the solvent. The 1,8-ANS is dissolved in water which holds refractive index of 1.33, while the QDs is dissolved in NMP solution which holds a refractive index of 1.47. I and A are referring to the integrated emission intensity and absorbance, respectively for samples and reference compound. Errors may exist in the exceptional large value of PdSe$_2$ QDs solution due to obvious distinction between its integration of I and A and the reference.
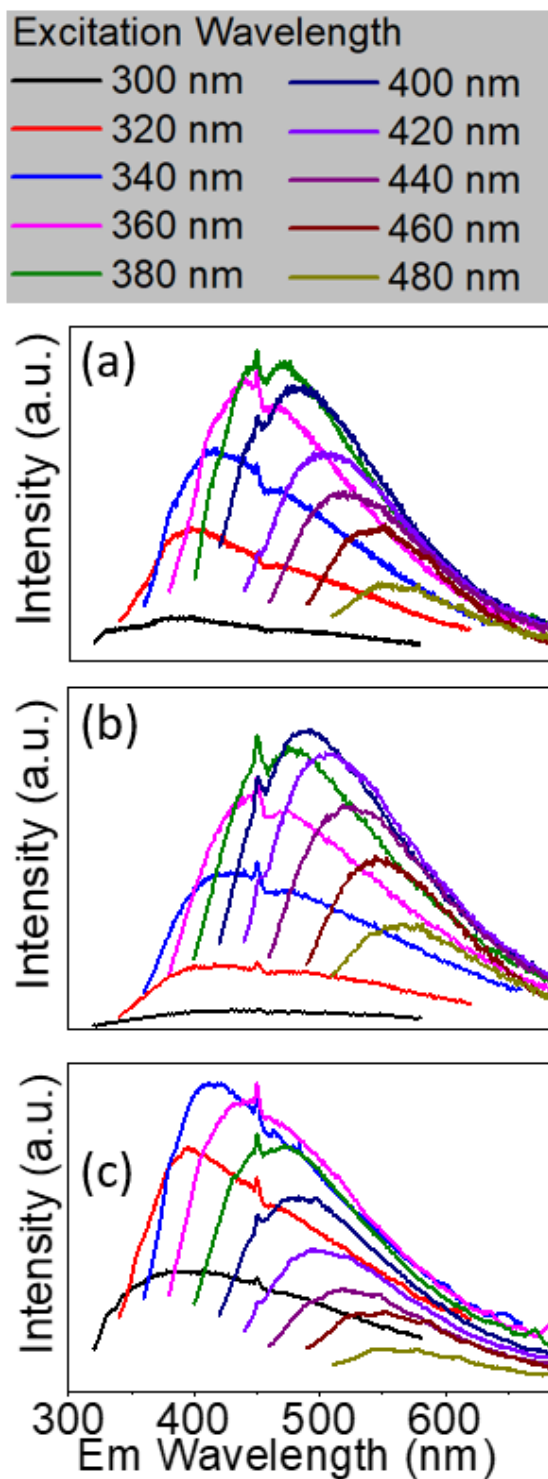
Figure 32 Emission (Em) spectra of (a) PtS_2 QDs solution, (b) PdS_2 QDs solution, and

(c) $PdSe_2$ QDs solution.

In the next step, the time-resolved PL decay measurement is performed at room temperature as depicted in Figure 34, while PtS_2, PdS_2, and $PdSe_2$ QDs samples are excited by 377, 397.5, and 346 nm wavelengths, respectively. The decay lifetime curves of QDs samples are monitored and fitted by dual-exponential function. The function presented in Eq. 3 explains that the decay curve is dominated by two de-excitation processes in the surface states and the core states, corresponding to a long-lived component τ_1 and a short-lived component τ_2 [235], [236]. The average lifetime (τ_{ave}) is estimated by substituting parameters of Eq. 3 into Eq. 4. The fitted values as listed in Table 5 suggest that τ_1 dominates the decay lifetime for all QDs samples, indicating that their core states fulfill essential role in the PL decay kinetics. The Pd based QDs may exhibit prolonged decay lifetimes than the Pt based group-10 TMDs QDs according to τ_{ave}. The better stabilities of PdS_2 and $PdSe_2$ may attribute to this longer decay lifetime.

$$A(t) = a_1 \exp\left(^{-\tau}/\tau_1\right) + a_2 \exp\left(^{-\tau}/\tau_2\right) \tag{3}$$

$$\tau_{ave} = \frac{a_1\tau_1{}^2 + a_2\tau_2{}^2}{a_1\tau_1 + a_2\tau_2} \tag{4}$$

Table 5 Fitted decay lifetimes for PtS_2 QDs solution, PdS_2 QDs solution, and $PdSe_2$ QDs solution

	a_1	τ_1/ns	a_2	τ_2/ns	τ_{ave}/ns
PtS_2 QDs	0.098	1.15	0.902	0.21	0.56
PdS_2 QDs	0.215	6.25	0.786	0.38	5.18
$PdSe_2$ QDs	0.230	3.64	0.770	0.33	2.88
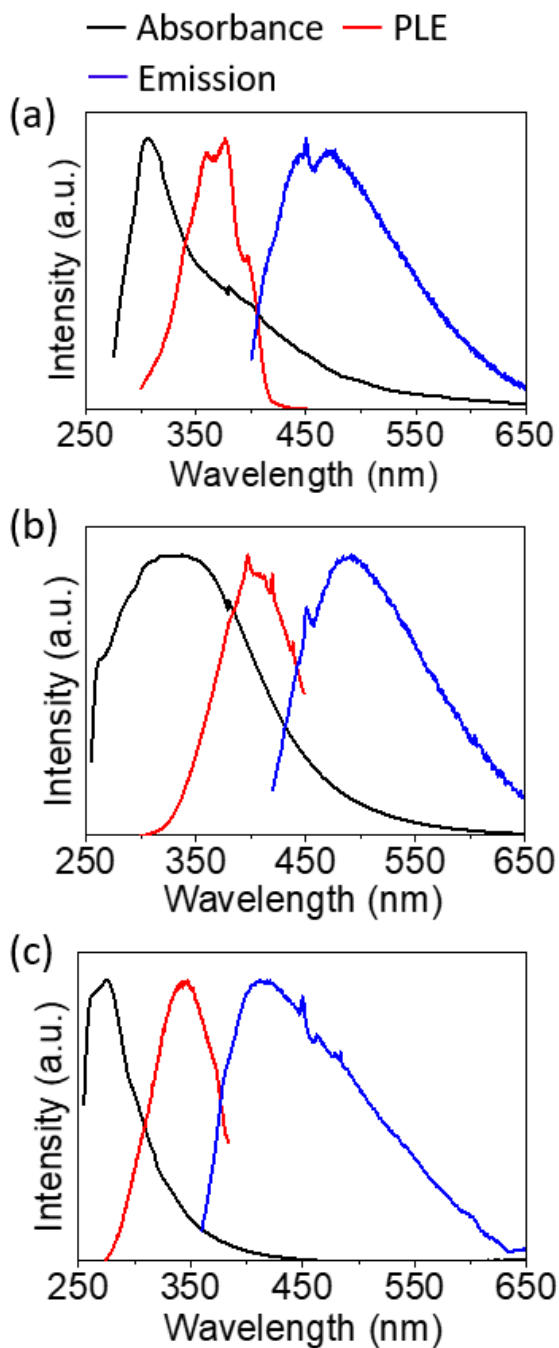
Figure 33 Normalized absorption spectra (black curve), photoluminescence excitation (PLE) spectra (red curve), and the maximum emission spectra (blue curve) of (a) PtS_2 QDs solution, (b) PdS_2 QDs solution, and (c) $PdSe_2$ QDs solution.
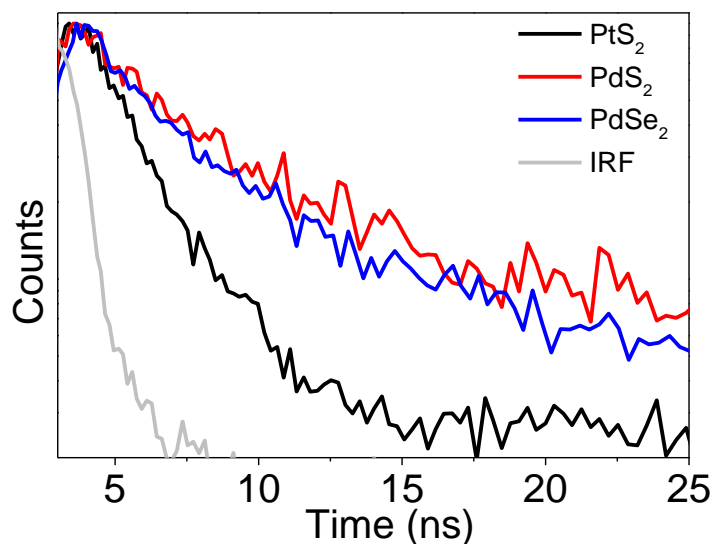
Figure 34 Decay profile of PtS$_2$ QDs solution, PdS$_2$ QDs solution, and PdSe$_2$ QDs solution.

5.4 Conclusions

In this study, 3 typical group-10 TMDs materials QDs were fabricated via solvent exfoliation. The as-prepared PtS$_2$, PdS$_2$, and PdSe$_2$ QDs exhibit average diameters of 4.73 nm, while their average thicknesses were determined as 2.82 nm, 2.61 nm, and 1.99 nm. Very good air stabilities were observed for PdS$_2$ and PdSe$_2$. The optical characteristics for those QDs solutions were monitored, exhibiting excitation wavelength-dependent behavior and large stokes shifts. The PL emission wavelengths might be strongly related to the size of QDs due to quantum size effect. This study is basically a short demonstration of simple synthesis process using solvent exfoliation and several optical performance parameters for three different group-10 TMDs materials of PtS$_2$, PdS$_2$, and PdSe$_2$ QDs. Most importantly, to our knowledge, so far this is the first demonstration of PL behaviors for PdS$_2$, and PdSe$_2$ QDs. We believe that this study with some excellent optical properties of these noble

2D materials should be beneficial for applications related to real time imaging, single molecule detection, light-emitting diode, and bio-sensing in addressing some analytical and biological issues which are currently being encountered in the fields.

Chapter 6 Summary and future works

In this chapter, a summary of this thesis is discussed and future works are presented. The summary includes 3 parts: PtS_2 based SA for Q-switching laser application; PtS_2 QDs fabrication and its photoluminescence behavior; PL performances of 3 typical group-10 TMDs (PtS_2, PdS_2, $PdSe_2$) QDs. The plans for future study is briefly discussed in the end of this thesis.

6.1 Summary

The novel 2D TMDs materials become attractive for saturable absorbers application due to their low-cost, simple, and compact advantages. PtS_2, a member of group-10 TMDs materials, based SA is then developed for the first time in this work via ultrasonic liquid exfoliation. This SA is then composing into laser cavity and a stable 1569 nm Q-switching pulses are achieved. Along with pump power increase from 53 mW to 84 mW, the pulse duration varies from 9.6 to 4.2 µs, and repetition rate increases from 18.1 to 24.6 kHz. The maximum value of output power is 1.1 mW. This work exhibits the Q-switching capability of PtS_2 and shed light upon exploring other optical performances of this material and its group-10 TMDs family.

Inspired by Q-switching laser performances of PtS_2 microflakes, the other optical performances of this materials seem charming for further exploration. Even though the frontiers report no PL signal can be detected in monolayer PtS_2, in my following work, the PL behaviour of PtS_2 is obtained for the first time by shrinking the size to QDs scale via a low-cost liquid exfoliation method. The as-prepared QDs hold an

average dimension of 3.9 nm diameter with 2.9 nm thickness, exhibiting typical excitation dependent PL spectra. Such behaviour verifies the quantum confinement effect of as-prepared PtS_2 QDs. The 328.5 nm excitation wavelength produces the maximum PL emission peak at 407.2 nm wavelength. The observation of promising long-term stability proves PtS_2 QDs' potential in future PL applications.

The discovery of PtS_2 QDs PL signals encourages me to expand my research interests to other group-10 TMDs materials. In this part, PtS_2, PdS_2, and $PdSe_2$ QDs are fabricated and their PL behaviors are presented via comparison to each other. In order to solve the low yield issue in previous work, NMP is chosen as the solvent thanks to its good compatibility with 2D layered TMDs materials. The as-prepared PtS_2, PdS_2, and $PdSe_2$ QDs hold average diameters of 4.73, 4.99, and 4.17 nm, and average thicknesses of 2.82 nm, 2.61 nm, and 1.99 nm, respectively. The XPS analyzation proves good air stability for PdS_2 and $PdSe_2$. The PL spectra of PtS_2, PdS_2, and $PdSe_2$ QDs are achieved, displaying excitation dependent characteristic and the highest emission peaks appear at 468.5, 491, and 413 nm, respectively. The large stokes shifts are also observed in such 3 typical group-10 TMDs QDs. Time-resolved PL decay measurement is also conducted for these QDs samples, illustrating that Pd based group-10 TMDs QDs hold longer decay lifetimes than that of Pt based QDs. In addition, to my best knowledge, this is so far the first reveal of PL performances of PdS_2, and $PdSe_2$ QDs. Even though the research of optical performances of group-10 TMDs materials are still in their initial stages, my study may suggest their potentials that are capable to benefit future optical, photo-voltage,

or bio-medicine applications.

6.2 Future works

Thanks to quantum confinement effect, group-10 TMDs QDs encounter opportunity to show their potentials in future optical, photo-voltage, or bio-medicine applications. Since PtS_2 exhibit the capability of Q-switching lasing, logically further study can be done on other group-10 TMDs materials, such as $PtSe_2$, PdS_2, $PdSe_2$.Even though distinct PL performances are confirmed in PtS_2, PdS_2, and $PdSe_2$ QDs, their up-conversion PL performance still remain obscure. The realistic optical applications of such QDs become attractive. Learning from recent study of bio-imaging using traditional TMDs materials based QDs, the group-10 TMDs QDs may found their possibility in this advancing field. Apart from optical applications, several few-layer group-10 TMDs materials based FETs have been reported with promising performances. The typical tunable band gap of group-10 TMDs may also benefit some electrical applications, such as FETs, and memory devices, it is intriguing to explore the improvement by further shrinking monolayer structure to QDs scale.

References

[1]   J. J. Zayhowski and C. Dill, "Diode-pumped passively Q-switched picosecond microchip lasers," *Opt. Lett.*, vol. 19, no. 18, pp. 1427–1429, 1994.

[2]   A. J. McGrath, J. Munch, G. Smith, and P. Veitch, "Injection-seeded, single-frequency, Q-switched erbium: glass laser for remote sensing," *Appl. Opt.*, vol. 37, no. 24, pp. 5706–5709, 1998.

[3]   D. Xu, Y. Wang, H. Li, J. Yao, and Y. H. Tsang, "104 W high stability green laser generation by using diode laser pumped intracavity frequency-doubling Q-switched composite ceramic Nd: YAG laser," *Opt. Express*, vol. 15, no. 7, pp. 3991–3997, 2007.

[4]   J. J. Degnan, "Optimization of passively Q-switched lasers," *IEEE J. Quantum Electron.*, vol. 31, no. 11, pp. 1890–1901, 1995.

[5]   K. . Yumashev, I. . Denisov, N. . Posnov, N. . Kuleshov, and R. Moncorge, "Excited state absorption and passive Q-switch performance of Co^{2+} doped oxide crystals," *J. Alloys Compd.*, vol. 341, no. 1–2, pp. 366–370, 2002.

[6]   Y. Bai *et al.*, "Passively Q-switched $Nd:YVO_4$ laser with a $Cr4^+:YAG$ crystal saturable absorber," *Appl. Opt.*, vol. 36, no. 12, pp. 2468–2472, 1997.

[7]   C. Y. Tang *et al.*, "Passively Q-switched Nd:YVO4 laser using WS_2 saturable absorber fabricated by radio frequency magnetron sputtering deposition," *J. Light. Technol.*, vol. 35, no. 19, pp. 4120–4124, 2017.

[8]   Z. Luo *et al.*, "Graphene-based passively Q-switched dual-wavelength erbium-doped fiber laser," *Opt. Lett.*, vol. 35, no. 21, pp. 3709–3711, 2010.

[9]   D. Popa, Z. Sun, T. Hasan, F. Torrisi, F. Wang, and A. C. Ferrari, "Graphene Q-switched, tunable fiber laser," *Appl. Phys. Lett.*, vol. 98, no. 7, pp. 73106, 2011.

[10]   J. Q. Zhao *et al.*, "Graphene-oxide-based Q-switched fiber laser with stable five-wavelength operation," *Chinese Phys. Lett.*, vol. 29, no. 11, pp. 114206, 2012.

[11]   J. Zhao *et al.*, "An Ytterbium-doped fiber laser with dark and Q-switched pulse generation using graphene-oxide as saturable absorber," *Opt. Commun.*, vol. 312, pp. 227–232, 2014.

[12]   H. Yu *et al.*, "Sub-100 ns solid-state laser Q-switched with double wall carbon nanotubes," *Opt. Commun.*, vol. 306, pp. 128–130, 2013.

[13]   X. Luo *et al.*, "Large Frequency Change with Thickness in Interlayer Breathing Mode-Significant Interlayer Interactions in Few Layer Black Phosphorus," *Nano Lett.*, vol. 15, no. 6, pp. 3931–3938, 2015.

[14]   J. Kang *et al.*, "Solvent exfoliation of electronic-grade, two-dimensional black phosphorus," *ACS Nano*, vol. 9, no. 4, pp. 3596–3604, 2015.

[15]   C. Chen, W. Yu, T. Liu, S. Cao, and Y. Tsang, "Graphene oxide/WS$_2$/Mg-doped ZnO nanocomposites for solar-light catalytic and anti-bacterial applications," *Sol. Energy Mater. Sol. Cells*, vol. 160, pp. 43–53, 2017.

[16] M. Chhowalla, H. S. Shin, G. Eda, L. J. Li, K. P. Loh, and H. Zhang, "The chemistry of two-dimensional layered transition metal dichalcogenide nanosheets," *Nat. Chem.*, vol. 5, no. 4, pp. 263–275, 2013.

[17] R. I. Woodward *et al.*, "Tunable Q-switched fiber laser based on saturable edge-state absorption in few-layer molybdenum disulfide (MoS_2)," *Opt. Express*, vol. 22, no. 25, pp. 31113–31122, 2014.

[18] and K. P. L. H. Zhang, S. B. Lu, J. Zheng, J. Du, S. C. Wen, D. Y. Tang, "Molybdenum disulfide (MoS_2) as a broadband saturable absorber for ultra-fast photonics," *Opt. Express*, vol. 22, pp. 7249, 2014.

[19] R. I. Woodward *et al.*, "Wideband saturable absorption in few-layer molybdenum diselenide ($MoSe_2$) for Q-switching Yb-, Er- and Tm-doped fiber lasers," *Opt. Express*, vol. 23, no. 15, pp. 20051–20061, 2015.

[20] K. Wu, X. Zhang, J. Wang, X. Li, and J. Chen, "WS_2 as a saturable absorber for ultrafast photonic applications of mode-locked and Q-switched lasers," *Opt. Express*, vol. 23, no. 9, pp. 11453–11461, 2015.

[21] B. Chen, X. Zhang, K. Wu, H. Wang, J. Wang, and J. Chen, "Q-switched fiber laser based on transition metal dichalcogenides MoS_2, $MoSe_2$, WS_2, and WSe_2," *Opt. Express*, vol. 23, no. 20, pp. 26723–26737, 2015.

[22] P. Yan *et al.*, "Microfiber-based WS_2-film saturable absorber for ultra-fast photonics," *Opt. Mater. Express*, vol. 5, no. 3, pp. 479–489, 2015.

[23] Y. Wang *et al.*, "Monolayer $PtSe_2$, a new semiconducting transition-metal-

dichalcogenide, epitaxially grown by direct selenization of Pt," *Nano Lett.*, vol. 15, no. 6, pp. 4013–4018, 2015.

[24] Y. Zhao *et al.*, "High-electron-mobility and air-stable 2D layered PtSe$_2$ FETs," *Adv. Mater.*, vol. 29, no. 5, pp. 1604230, 2017.

[25] L. Zeng *et al.*, "Fast, self-driven, air-stable, and broadband photodetector based on vertically aligned PtSe$_2$/GaAs heterojunction," *Adv. Funct. Mater.*, vol. 28, no. 16, pp. 1705970, 2018.

[26] L. Li, W. Wang, Y. Chai, H. Li, M. Tian, and T. Zhai, "Few-layered PtS$_2$ phototransistor on h-BN with hgh gain," *Adv. Funct. Mater.*, vol. 27, no. 27, pp. 1701011, 2017.

[27] Y. Zhao *et al.*, "Extraordinarily strong interlayer interaction in 2D layered PtS$_2$," *Adv. Mater.*, vol. 28, no. 12, pp. 2399–2407, 2016.

[28] A. AlMutairi, D. Yin, and Y. Yoon, "PtSe$_2$ field-effect transistors: new opportunities for electronic devices," *IEEE Electron Device Lett.*, vol. 39, no. 1, pp. 151–154, 2018.

[29] V. Tran, R. Soklaski, Y. Liang, and L. Yang, "Layer-controlled band gap and anisotropic excitons in few-layer black phosphorus," *Phys. Rev. B*, vol. 89, no. 23, pp. 235319,. 2014.

[30] P. Miró, M. Ghorbani-Asl, and T. Heine, "Two dimensional materials beyond MoS$_2$: noble-transition-metal dichalcogenides," *Angew. Chemie Int. Ed.*, vol. 53, no. 11, pp. 3015–3018, 2014.

[31] J. Koo, Y. I. Jhon, J. Park, J. Lee, Y. M. Jhon, and J. H. Lee, "Near-Infrared saturable absorption of defective bulk-structured WTe_2 for femtosecond laser mode-locking," *Adv. Funct. Mater.*, vol. 26, no. 41, pp. 7454–7461, 2016.

[32] A. K. Geim and K. S. Novoselov, "The rise of graphene," *Nat. Mater.*, vol. 6, pp. 183, 2007.

[33] H. Huang, Xiao; Zeng, Zhiyuan; Zhang, "Metal dichalcogenide nanosheets: preparation, properties and applications," *Chem. Soc. Rev.*, vol. 42, p. 1934, 2013.

[34] Q. H. Wang, K. Kalantar-Zadeh, A. Kis, J. N. Coleman, and M. S. Strano, "Electronics and optoelectronics of two-dimensional transition metal dichalcogenides," *Nat. Nanotechnol.*, vol. 7, pp. 699, 2012.

[35] C. Tan and H. Zhang, "Two-dimensional transition metal dichalcogenide nanosheet-based composites," *Chem. Soc. Rev.*, vol. 44, no. 9, pp. 2713–2731, 2015.

[36] J. N. Coleman *et al.*, "Two-dimensional nanosheets produced by liquid exfoliation of layered materials," *Science*, vol. 331, no. 6017, pp. 568–571, 2011.

[37] L. Lin, Y. Xu, S. Zhang, I. M. Ross, A. C. M. Ong, and D. A. Allwood, "Fabrication of luminescent monolayered tungsten dichalcogenides quantum dots with giant spin-valley coupling," *ACS Nano*, vol. 7, no. 9, pp. 8214–8223, 2013.

[38]   S. Y. Lim, W. Shen, and Z. Gao, "Carbon quantum dots and their applications," *Chem. Soc. Rev.*, vol. 44, no. 1, pp. 362–381, 2015.

[39]   Z. X. Gan *et al.*, "Quantum confinement effects across two-dimensional planes in MoS_2 quantum dots," *Appl. Phys. Lett.*, vol. 106, no. 23, pp. 233113, 2015.

[40]   S. Xu, D. Li, and P. Wu, "One-Pot, facile, and versatile synthesis of monolayer MoS_2/WS_2 quantum dots as bioimaging probes and efficient electrocatalysts for hydrogen evolution reaction," *Adv. Funct. Mater.*, vol. 25, no. 7, pp. 1127–1136, 2015.

[41]   H. Long *et al.*, "Tuning nonlinear optical absorption properties of WS_2 nanosheets," *Nanoscale*, vol. 7, no. 42, pp. 17771–17777, 2015.

[42]   H. Long *et al.*, "The WS_2 quantum dot: preparation, characterization and its optical limiting effect in polymethylmethacrylate," *Nanotechnology*, vol. 27, no. 41, pp. 414005, 2016.

[43]   H. Li *et al.*, "Water-soluble fluorescent carbon quantum dots and photocatalyst design," *Angew. Chemie Int. Ed.*, vol. 49, no. 26, pp. 4430–4434, 2010.

[44]   S. Cao *et al.*, "MnO_x quantum dots decorated reduced graphene oxide/TiO_2 nanohybrids for enhanced activity by a UV pre-catalytic microwave method," *Appl. Catal. B Environ.*, vol. 176–177, pp. 500–512, 2015.

[45]   P. V Kamat, "Quantum dot solar cells. Semiconductor nanocrystals as light garvesters," *J. Phys. Chem. C*, vol. 112, no. 48, pp. 18737–18753, 2008.

[46] L. Cao *et al.*, "Carbon dots for multiphoton bioimaging," *J. Am. Chem. Soc.*, vol. 129, no. 37, pp. 11318–11319, 2007.

[47] A. D. Oyedele *et al.*, "PdSe$_2$: pentagonal two-dimensional layers with high air stability for electronics," *J. Am. Chem. Soc.*, vol. 139, no. 40, pp. 14090–14097, 2017.

[48] M. A. ElGhazali *et al.*, "Pressure-induced superconductivity up to 13.1 K in the pyrite phase of palladium diselenide PdS$_2$," *Phys. Rev. B,* vol. 96, no. 6, pp. 60509, 2017.

[49] X. Chia, A. Adriano, P. Lazar, Z. Sofer, J. Luxa, and M. Pumera, "Layered platinum dichalcogenides (PtS$_2$, PtSe$_2$, and PtTe$_2$) electrocatalysis: monotonic dependence on the chalcogen size," *Adv. Funct. Mater.*, vol. 26, no. 24, pp. 4306–4318, 2016.

[50] L. Tao *et al.*, "Vertically standing PtSe$_2$ film: a saturable absorber for a passively mode-locked Nd:LuVO4 laser," *Photon. Res.*, vol. 6, no. 7, pp. 750–755, 2018.

[51] L. Zeng *et al.*, "Fast, self-Driven, air-stable, and broadband photodetector based on vertically aligned PtSe$_2$/GaAs heterojunction," *Adv. Funct. Mater.*, vol. 28, no. 16, pp. 1705970, 2018.

[52] L. Zeng *et al.*, "Ultrafast and sensitive photodetector based on a PtSe$_2$/silicon nanowire array heterojunction with a multiband spectral response from 200 to 1550 nm," *NPG Asia Mater.*, vol 10, pp 352–362, 2018.

[53] S. Deng, L. Li, and Y. Zhang, "Strain modulated electronic, mechanical, and optical properties of the monolayer PdS_2 , $PdSe_2$, and $PtSe_2$ for tunable devices," *ACS Appl. Nano Mater.*, vol. 1, no. 4, pp. 1932–1939, 2018.

[54] M. Ghorbani-Asl, A. Kuc, P. Miró, and T. Heine, "A single-material logical junction based on 2D crystal PdS_2," *Adv. Mater.*, vol. 28, no. 5, pp. 853–856, 2016.

[55] M. Sun *et al.*, "Few-layer $PdSe_2$ sheets: promising thermoelectric materials driven by high valley convergence," *ACS Omega*, vol. 3, no. 6, pp. 5971–5979, 2018.

[56] W. L. Chow *et al.*, "High mobility 2D palladium diselenide field-effect transistors with tunable ambipolar characteristics," *Adv. Mater.*, vol. 29, no. 21, pp. 1–8, 2017.

[57] L. Zeng *et al.*, "Photodetectors: controlled synthesis of 2D palladium diselenide for sensitive photodetector applications," *Adv. Funct. Mater.*, vol. 29, no. 1, pp. 1970005, 2019.

[58] X. Wang, H. Long, Y. Hong, C. Y. Tang, and H. Yuan, "Fabrication of luminescent PtS_2 quantum dots," *J. Lumin.*, vol. 211, no. March, pp. 227–232, 2019.

[59] H. W. Kroto, J. R. Heath, S. C. O'Brien, R. F. Curl, and R. E. Smalley, "C60: Buckminsterfullerene," *Nature*, vol. 318, no. 6042, pp. 162–163, 1985.

[60] S. Iijima, "Helical microtubules of graphitic carbon," *Nature*, vol. 354, no. 6348,

pp. 56–58, 1991.

[61]   K. S. Novoselov *et al.*, "Electric field effect in atomically thin carbon films," *Science*, vol. 306, no. 5696, pp. 666–669, 2004.

[62]   X. Xu *et al.*, "Electrophoretic analysis and purification of fluorescent single-walled carbon nanotube fragments," *J. Am. Chem. Soc.*, vol. 126, no. 40, pp. 12736–12737, 2004.

[63]   L. Song *et al.*, "Large scale growth and characterization of atomic hexagonal Boron Nitride Layers," *Nano Lett.*, vol. 10, no. 8, pp. 3209–3215, 2010.

[64]   S. Manzeli, D. Ovchinnikov, D. Pasquier, O. V Yazyev, and A. Kis, "2D transition metal dichalcogenides," *Nat. Rev. Mater.*, vol. 2, pp. 17033, 2017.

[65]   K. S. Novoselov *et al.*, "Two-dimensional atomic crystals," *Proc. Natl. Acad. Sci. U. S. A.*, vol. 102, no. 30, pp. 10451–10453, 2005.

[66]   P. W. Sutter, J.-I. Flege, and E. A. Sutter, "Epitaxial graphene on ruthenium," *Nat. Mater.*, vol. 7, pp. 406, 2008.

[67]   T. A. Land, T. Michely, R. J. Behm, J. C. Hemminger, and G. Comsa, "STM investigation of single layer graphite structures produced on Pt(111) by hydrocarbon decomposition," *Surf. Sci.*, vol. 264, no. 3, pp. 261–270, 1992.

[68]   C. Berger *et al.*, "Ultrathin epitaxial graphite: 2D electron gas properties and a Route toward graphene-based nanoelectronics," *J. Phys. Chem. B*, vol. 108, no. 52, pp. 19912–19916, 2004.

[69] J. Sakamoto, J. van Heijst, O. Lukin, and A. D. Schlüter, "Two-dimensional polymers: just a dream of synthetic chemists?," *Angew. Chemie Int. Ed.*, vol. 48, no. 6, pp. 1030–1069, 2009.

[70] R. Hao, W. Qian, L. Zhang, and Y. Hou, "Aqueous dispersions of TCNQ-anion-stabilized graphene sheets," *Chem. Commun.*, no. 48, pp. 6576–6578, 2008.

[71] S. Stankovich *et al.*, "Graphene-based composite materials," *Nature*, vol. 442, no. 7100, pp. 282–286, 2006.

[72] W. Cai *et al.*, "Synthesis and solid-state NMR structural characterization of 13 C-labeled graphite oxide," *Science*, vol. 321, no. 5897, pp. 1815 – 1817, 2008.

[73] A. Lerf, H. He, M. Forster, and J. Klinowski, "Structure of graphite oxide revisited," *J. Phys. Chem. B*, vol. 102, no. 23, pp. 4477–4482, 1998.

[74] D. Li, M. B. Müller, S. Gilje, R. B. Kaner, and G. G. Wallace, "Processable aqueous dispersions of graphene nanosheets," *Nat. Nanotechnol.*, vol. 3, pp. 101, 2008.

[75] X. Wang, L. Zhi, and K. Müllen, "Transparent, conductive graphene electrodes for dye-sensitized solar cells," *Nano Lett.*, vol. 8, no. 1, pp. 323–327, 2008.

[76] G. Eda, G. Fanchini, and M. Chhowalla, "Large-area ultrathin films of reduced graphene oxide as a transparent and flexible electronic material," *Nat. Nanotechnol.*, vol. 3, pp. 270, 2008.

[77] K. F. Mak, C. Lee, J. Hone, J. Shan, and T. F. Heinz, "Atomically thin MoS_2: A

new direct-gap semiconductor," *Phys. Rev. Lett.*, vol. 105, no. 13, pp. 136805, 2010.

[78]   B. Radisavljevic, A. Radenovic, J. Brivio, V. Giacometti, and A. Kis, "Single-layer MoS$_2$ transistors," *Nat. Nanotechnol.*, vol. 6, pp. 147, 2011.

[79]   G. R. Bhimanapati *et al.*, "Recent advances in two-dimensional materials beyond graphene," *ACS Nano*, vol. 9, no. 12, pp. 11509–11539, Dec. 2015.

[80]   R. Lv *et al.*, "Transition metal dichalcogenides and beyond: synthesis, properties, and applications of single- and few-layer nanosheets," *Acc. Chem. Res.*, vol. 48, no. 1, pp. 56–64, 2015.

[81]   Y. Shi, H. Li, and L. J. Li, "Recent advances in controlled synthesis of two-dimensional transition metal dichalcogenides via vapour deposition techniques," *Chem. Soc. Rev.*, vol. 44, no. 9, pp. 2744–2756, 2015.

[82]   D. Voiry, A. Mohite, and M. Chhowalla, "Phase engineering of transition metal dichalcogenides," *Chem. Soc. Rev.*, vol. 44, no. 9, pp. 2702–2712, 2015.

[83]   Y. Yu, C. Li, Y. Liu, L. Su, Y. Zhang, and L. Cao, "Controlled scalable Synthesis of uniform, high-quality monolayer and few-layer MoS$_2$ films," *Sci. Rep.*, vol. 3, pp. 1866, 2013.

[84]   X. Xu, W. Yao, D. Xiao, and T. F. Heinz, "Spin and pseudospins in layered transition metal dichalcogenides," *Nat. Phys.*, vol. 10, pp. 343, 2014.

[85]   Y. Lee *et al.*, "Synthesis of wafer-scale uniform molybdenum disulfide films

with control over the layer number using a gas phase sulfur precursor," *Nanoscale*, vol. 6, no. 5, pp. 2821–2826, 2014.

[86] R. Gatensby *et al.*, "Controlled synthesis of transition metal dichalcogenide thin films for electronic applications," *Appl. Surf. Sci.*, vol. 297, pp. 139–146, 2014.

[87] Y. Jung, J. Shen, Y. Liu, J. M. Woods, Y. Sun, and J. J. Cha, "Metal seed layer thickness-induced transition from vertical to horizontal growth of MoS_2 and WS_2," *Nano Lett.*, vol. 14, no. 12, pp. 6842–6849, 2014.

[88] C. Muratore *et al.*, "Continuous ultra-thin MoS_2 films grown by low-temperature physical vapor deposition," *Appl. Phys. Lett.*, vol. 104, no. 26, p. 261604, 2014.

[89] C. R. Serrao *et al.*, "Highly crystalline MoS_2 thin films grown by pulsed laser deposition," *Appl. Phys. Lett.*, vol. 106, no. 5, pp. 52101, 2015.

[90] P. Browning *et al.*, "Large-area synthesis of WSe_2 from WO3 by selenium–oxygen ion exchange," *2D Mater.*, vol. 2, no. 1, pp. 14003, 2015.

[91] Z. Jin, S. Shin, D. H. Kwon, S.-J. Han, and Y.-S. Min, "Novel chemical route for atomic layer deposition of MoS_2 thin film on SiO_2/Si substrate," *Nanoscale*, vol. 6, no. 23, pp. 14453–14458, 2014.

[92] A. Tarasov *et al.*, "Highly uniform trilayer molybdenum disulfide for wafer-scale device fabrication," *Adv. Funct. Mater.*, vol. 24, no. 40, pp. 6389–6400, 2014.

[93] Y. H. Lee *et al.*, "Synthesis and transfer of single-layer transition metal

disulfides on diverse surfaces," *Nano Lett.*, vol. 13, no. 4, pp. 1852–1857, 2013.

[94] X. Ling *et al.*, "Role of the Seeding Promoter in MoS$_2$ Growth by Chemical Vapor Deposition," *Nano Lett.*, vol. 14, no. 2, pp. 464–472, 2014.

[95] S. Vishwanath *et al.*, "Comprehensive structural and optical characterization of MBE grown MoSe$_2$ on graphite, CaF$_2$ and graphene," *2D Mater.*, vol. 2, no. 2, pp. 24007, 2015.

[96] D. Chiappe *et al.*, "Two-dimensional Si nanosheets with local hexagonal structure on a MoS$_2$ surface," *Adv. Mater.*, vol. 26, no. 13, pp. 2096–2101, 2014.

[97] H. Liu *et al.*, "Dense network of one-dimensional midgap metallic modes in monolayer MoSe$_2$ and their spatial undulations," *Phys. Rev. Lett.*, vol. 113, no. 6, pp. 66105, 2014.

[98] R. Yue *et al.*, "HfSe$_2$ thin films: 2D transition metal dichalcogenides grown by molecular beam epitaxy," *ACS Nano*, vol. 9, no. 1, pp. 474–480, 2015.

[99] H. J. Liu *et al.*, "Molecular-beam epitaxy of monolayer and bilayer WSe$_2$: a scanning tunneling microscopy/spectroscopy study and deduction of exciton binding energy," *2D Mater.*, vol. 2, no. 3, pp. 34004, 2015.

[100] A. T. Barton *et al.*, "Transition metal dichalcogenide and hexagonal boron nitride heterostructures grown by molecular beam epitaxy," *Microelectron. Eng.*, vol. 147, pp. 306–309, 2015.

[101] S. M. Eichfeld *et al.*, "Highly scalable, atomically thin WSe_2 grown via metal–organic chemical vapor deposition," *ACS Nano*, vol. 9, no. 2, pp. 2080–2087, 2015.

[102] K. Kang *et al.*, "High-mobility three-atom-thick semiconducting films with wafer-scale homogeneity," *Nature*, vol. 520, pp. 656, 2015.

[103] V. Kranthi Kumar, S. Dhar, T. H. Choudhury, S. A. Shivashankar, and S. Raghavan, "A predictive approach to CVD of crystalline layers of TMDs: the case of MoS_2," *Nanoscale*, vol. 7, no. 17, pp. 7802–7810, 2015.

[104] D. Kong *et al.*, "Synthesis of MoS_2 and $MoSe_2$ films with vertically aligned layers," *Nano Lett.*, vol. 13, no. 3, pp. 1341–1347, 2013.

[105] Y. Jung, J. Shen, Y. Sun, and J. J. Cha, "Chemically synthesized heterostructures of two-dimensional molybdenum/tungsten-based dichalcogenides with vertically aligned layers," *ACS Nano*, vol. 8, no. 9, pp. 9550–9557, 2014.

[106] H. Liu, K. K. A. Antwi, S. Chua, and D. Chi, "Vapor-phase growth and characterization of $Mo_{1-x}W_xS_2$ ($0 \leq x \leq 1$) atomic layers on 2-inch sapphire substrates," *Nanoscale*, vol. 6, no. 1, pp. 624–629, 2014.

[107] Y. Chen *et al.*, "Tunable band gap photoluminescence from atomically thin transition-metal dichalcogenide alloys," *ACS Nano*, vol. 7, no. 5, pp. 4610–4616, 2013.

[108] V. Klee *et al.*, "Superlinear composition-dependent photocurrent in CVD-

grown monolayer $MoS_{2(1-x)}Se_{2x}$ alloy devices," *Nano Lett.*, vol. 15, no. 4, pp. 2612–2619, 2015.

[109] J. Mann *et al.*, "2-Dimensional transition metal dichalcogenides with tunable direct band gaps: $MoS_{2(1-x)}Se_{2x}$ monolayers," *Adv. Mater.*, vol. 26, no. 9, pp. 1399–1404, 2014.

[110] H. Li *et al.*, "Lateral growth of composition graded atomic layer $MoS_{2(1-x)}Se_{2x}$ nanosheets," *J. Am. Chem. Soc.*, vol. 137, no. 16, pp. 5284–5287, 2015.

[111] I. S. Kim *et al.*, "Influence of stoichiometry on the optical and electrical properties of chemical vapor deposition derived MoS_2," *ACS Nano*, vol. 8, no. 10, pp. 10551–10558, 2014.

[112] V. K. Sangwan *et al.*, "Gate-tunable memristive phenomena mediated by grain boundaries in single-layer MoS_2," *Nat. Nanotechnol.*, vol. 10, pp. 403, 2015.

[113] I. Bilgin *et al.*, "Chemical bapor deposition synthesized atomically thin molybdenum disulfide with optoelectronic-grade crystalline quality," *ACS Nano*, vol. 9, no. 9, pp. 8822–8832, 2015.

[114] M. Mahjouri-Samani *et al.*, "Patterned arrays of lateral heterojunctions within monolayer two-dimensional semiconductors," *Nat. Commun.*, vol. 6, pp. 7749, 2015.

[115] Q. Ma *et al.*, "Postgrowth tuning of the bandgap of single-layer molybdenum disulfide films by sulfur/selenium exchange," *ACS Nano*, vol. 8, no. 5, pp. 4672–4677, 2014.

[116] G. H. Han *et al.*, "Seeded growth of highly crystalline molybdenum disulphide monolayers at controlled locations," *Nat. Commun.*, vol. 6, pp. 6128, 2015.

[117] J. Jeon *et al.*, "Layer-controlled CVD growth of large-area two-dimensional MoS2 films," *Nanoscale*, vol. 7, no. 5, pp. 1688–1695, 2015.

[118] H. J. Chuang *et al.*, "High mobility WSe P- and N-type field-effect transistors contacted by highly doped graphene for low-resistance contacts," *Nano Lett.*, vol. 14, no. 6, pp. 3594–3601, 2014.

[119] S. Chuang *et al.*, "MoS$_2$ P-type transistors and diodes enabled by high work function MoOx contacts," *Nano Lett.*, vol. 14, no. 3, pp. 1337–1342, 2014.

[120] S. Das and J. Appenzeller, "where does the current flow in two-dimensional layered systems?," *Nano Lett.*, vol. 13, no. 7, pp. 3396–3402, 2013.

[121] S. Das, R. Gulotty, A. V Sumant, and A. Roelofs, "All two-dimensional, flexible, transparent, and thinnest thin film transistor," *Nano Lett.*, vol. 14, no. 5, pp. 2861–2866, 2014.

[122] R. Kappera *et al.*, "Phase-engineered low-resistance contacts for ultrathin MoS$_2$ transistors," *Nat. Mater.*, vol. 13, pp. 1128, 2014.

[123] H. Yamaguchi *et al.*, "Spatially resolved photoexcited charge-carrier dynamics in phase-engineered monolayer MoS$_2$," *ACS Nano*, vol. 9, no. 1, pp. 840–849, 2015.

[124] C. Gong, L. Colombo, R. M. Wallace, and K. Cho, "The unusual mechanism

of partial fermi level pinning at metal–MoS_2 interfaces," *Nano Lett.*, vol. 14, no. 4, pp. 1714–1720, 2014.

[125] R. B. Jacobs-Gedrim *et al.*, "Extraordinary photoresponse in two-dimensional in_2se_3 nanosheets," *ACS Nano*, vol. 8, no. 1, pp. 514–521, 2014.

[126] M. Kang *et al.*, "Electrical characterization of multilayer $HfSe_2$ field-effect transistors on SiO_2 substrate," *Appl. Phys. Lett.*, vol. 106, no. 14, pp. 143108, 2015.

[127] D. J. Late *et al.*, "GaS and GaSe ultrathin layer transistors," *Adv. Mater.*, vol. 24, no. 26, pp. 3549–3554, 2012.

[128] H. S. Song *et al.*, "High-performance top-gated monolayer SnS_2 field-effect transistors and their integrated logic circuits," *Nanoscale*, vol. 5, no. 20, pp. 9666–9670, 2013.

[129] D. Akinwande, N. Petrone, and J. Hone, "Two-dimensional flexible nanoelectronics," *Nat. Commun.*, vol. 5, pp. 5678, 2014.

[130] J. Wang *et al.*, "Gate-modulated conductance of few-layer WSe_2 field-effect transistors in the subgap regime: Schottky barrier transistor and subgap impurity states," *Appl. Phys. Lett.*, vol. 106, no. 15, pp. 152104, 2015.

[131] W. Zhou *et al.*, "Intrinsic structural defects in monolayer molybdenum disulfide," *Nano Lett.*, vol. 13, no. 6, pp. 2615–2622, 2013.

[132] S. McDonnell, R. Addou, C. Buie, R. M. Wallace, and C. L. Hinkle, "Defect-

dominated doping and contact resistance in MoS_2," *ACS Nano*, vol. 8, no. 3, pp. 2880–2888, 2014.

[133] S. Tongay *et al.*, "Defects activated photoluminescence in two-dimensional semiconductors: interplay between bound, charged, and free excitons," *Sci. Rep.*, vol. 3, pp. 2657, 2013.

[134] Z. Tan *et al.*, "A small-signal generator based on a multi-layer graphene/molybdenum disulfide heterojunction," *Appl. Phys. Lett.*, vol. 103, no. 26, p. 263506, 2013.

[135] S. Das, M. Dubey, and A. Roelofs, "High gain, low noise, fully complementary logic inverter based on bi-layer WSe_2 field effect transistors," *Appl. Phys. Lett.*, vol. 105, no. 8, pp. 83511, 2014.

[136] N. Huo, S. Yang, Z. Wei, S.-S. Li, J.-B. Xia, and J. Li, "Photoresponsive and gas sensing field-effect transistors based on multilayer WS_2 nanoflakes," *Sci. Rep.*, vol. 4, pp. 5209, 2014.

[137] D. Sarkar, W. Liu, X. Xie, A. C. Anselmo, S. Mitragotri, and K. Banerjee, "MoS_2 field-effect transistor for next-generation label-free biosensors," *ACS Nano*, vol. 8, no. 4, pp. 3992–4003, 2014.

[138] L. Wang, Y. Wang, J. I. Wong, T. Palacios, J. Kong, and H. Y. Yang, "Functionalized MoS_2 nanosheet-based field-effect biosensor for label-free sensitive detection of cancer marker proteins in solution," *Small*, vol. 10, no. 6, pp. 1101–1105, 2014.

[139] A. Pospischil, M. M. Furchi, and T. Mueller, "Solar-energy conversion and light emission in an atomic monolayer p–n diode," *Nat. Nanotechnol.*, vol. 9, pp. 257, 2014.

[140] K. Roy *et al.*, "Graphene–MoS$_2$ hybrid structures for multifunctional photoresponsive memory devices," *Nat. Nanotechnol.*, vol. 8, pp. 826, 2013.

[141] W. J. Yu *et al.*, "Highly efficient gate-tunable photocurrent generation in vertical heterostructures of layered materials," *Nat. Nanotechnol.*, vol. 8, pp. 952, 2013.

[142] B. W. H. Baugher, H. O. H. Churchill, Y. Yang, and P. Jarillo-Herrero, "Optoelectronic devices based on electrically tunable p–n diodes in a monolayer dichalcogenide," *Nat. Nanotechnol.*, vol. 9, pp. 262, 2014.

[143] D. Jariwala *et al.*, "Gate-tunable carbon nanotube–MoS$_2$ heterojunction p-n diode," *Proc. Natl. Acad. Sci.*, vol. 110, no. 45, pp. 18076-18080, 2013.

[144] O. Lopez-Sanchez, D. Lembke, M. Kayci, A. Radenovic, and A. Kis, "Ultrasensitive photodetectors based on monolayer MoS$_2$," *Nat. Nanotechnol.*, vol. 8, pp. 497, 2013.

[145] J. S. Ross *et al.*, "Electrically tunable excitonic light-emitting diodes based on monolayer WSe$_2$ p–n junctions," *Nat. Nanotechnol.*, vol. 9, pp. 268, 2014.

[146] W. Zhang, M. H. Chiu, C. H. Chen, W. Chen, L. J. Li, and A. T. S. Wee, "Role of metal contacts in high-performance phototransistors based on WSe$_2$ monolayers," *ACS Nano*, vol. 8, no. 8, pp. 8653–8661, 2014.

[147] M. S. Jang *et al.*, "Tunable large resonant absorption in a midinfrared graphene Salisbury screen," *Phys. Rev. B*, vol. 90, no. 16, pp. 165409, 2014.

[148] W. Y. Liang, "Optical anisotropy in layer compounds," *J. Phys. C Solid State Phys.*, vol. 6, no. 3, pp. 551–565, 1973.

[149] H. A. Atwater and A. Polman, "Plasmonics for improved photovoltaic devices," *Nat. Mater.*, vol. 9, pp. 205, 2010.

[150] Z. Yu, A. Raman, and S. Fan, "Fundamental limit of nanophotonic light trapping in solar cells," *Proc. Natl. Acad. Sci.*, vol. 107, no. 41, pp. 17491-17496, 2010.

[151] R. R. Grote, S. J. Brown, J. B. Driscoll, R. M. Osgood, and J. A. Schuller, "Morphology-dependent light trapping in thin-film organic solar cells," *Opt. Express*, vol. 21, no. S5, pp. A847--A863, 2013.

[152] J. A. Schuller *et al.*, "Orientation of luminescent excitons in layered nanomaterials," *Nat. Nanotechnol.*, vol. 8, pp. 271, 2013.

[153] G. M. Akselrod *et al.*, "Leveraging nanocavity harmonics for control of optical processes in 2D semiconductors," *Nano Lett.*, vol. 15, no. 5, pp. 3578–3584, 2015.

[154] S. Butun, S. Tongay, and K. Aydin, "Enhanced light emission from large-area monolayer MoS_2 using plasmonic nanodisc arrays," *Nano Lett.*, vol. 15, no. 4, pp. 2700–2704, 2015.

[155] S. Gemming and G. Seifert, "Catalysts on the edge," *Nat. Nanotechnol.*, vol. 2, pp. 21, 2007.

[156] A. KJEKSHUS and F. GRQNVOLD, "High temperature X-ray study of the thermal expansion," *Acta Chem. Scand.*, vol. 13, no. 9, pp. 1767–1774, 1959.

[157] F. Gronvold, H. Haraldsen, and A. Kjekshus, "On the sulfides, selenides and tellurides of platinum," *ACTA Chem. Scand.*, vol. 14, no. 9, pp. 1879–1893, 1960.

[158] J. A. Wilson and A. D. Yoffe, "The transition metal dichalcogenides discussion and interpretation of the observed optical, electrical and structural properties," *Adv. Phys.*, vol. 18, no. 73, pp. 193–335, 1969.

[159] D. Dai, H.-J. Koo, M.-H. Whangbo, C. Soulard, X. Rocquefelte, and S. Jobic, "Trends in the structure and bonding in the layered platinum dioxide and dichalcogenides PtQ_2 (Q=O, S, Se, Te)," *J. Solid State Chem.*, vol. 173, no. 1, pp. 114–121, 2003.

[160] G. Y. Guo and W. Y. Liang, "The electronic structures of platinum dichalcogenides: PtS_2, $PtSe_2$ and $PtTe_2$," *J. Phys. C Solid State Phys.*, vol. 19, no. 7, pp. 995–1008, 1986.

[161] S. Soled, A. Wold, and O. Gorochov, "Crystal growth and characterization of several platinum sulfoselenides," *Mater. Res. Bull.*, vol. 11, no. 8, pp. 927–932, 1976.

[162] P. Miró, M. Ghorbani-Asl, and T. Heine, "Two dimensional materials beyond

MoS$_2$: noble-transition‑metal dichalcogenides," *Angew. Chemie Int. Ed.*, vol. 53, no. 11, pp. 3015–3018, 2014.

[163] W. Zhang, Z. Huang, W. Zhang, and Y. Li, "Two-dimensional semiconductors with possible high room temperature mobility," *Nano Res.*, vol. 7, no. 12, pp. 1731–1737, 2014.

[164] X. Wang *et al.*, "Laser Q-switching with PtS$_2$ microflakes saturable absorber," *Opt. Express*, vol. 26, no. 10, pp. 13055–13060, 2018.

[165] W. C. W. Chan and S. Nie, "Quantum dot bioconjugates for ultrasensitive nonisotopic detection," *Science*, vol. 281, no. 5385, pp. 2016-2018, 1998.

[166] X. Michalet *et al.*, "Quantum dots for live cells, in vivo imaging, and diagnostics," *Science*, vol. 307, no. 5709, pp. 538-544, 2005.

[167] J. Wang, S. Sun, F. Peng, L. Cao, and L. Sun, "Efficient one-pot synthesis of highly photoluminescent alkyl-functionalised silicon nanocrystals," *Chem. Commun.*, vol. 47, no. 17, pp. 4941–4943, 2011.

[168] F. Li, J. Wang, S. Sun, H. Wang, Z. Tang, and G. Nie, "Facile synthesis of pH-sensitive germanium nanocrystals with high quantum yield for intracellular acidic compartment imaging," *Small*, vol. 11, no. 16, pp. 1954–1961, 2015.

[169] C. Ding, C. Zhang, X. Yin, X. Cao, M. Cai, and Y. Xian, "Near-infrared fluorescent Ag$_2$S nanodot-based signal amplification for efficient detection of circulating tumor cells," *Anal. Chem.*, vol. 90, no. 11, pp. 6702–6709, 2018.

[170] B. L. Li *et al.*, "Emerging 0D transition-metal dichalcogenides for sensors, biomedicine, and clean energy," *Small*, vol. 13, no. 31, pp. 1700527, 2017.

[171] X. Wang, G. Sun, N. Li, and P. Chen, "Quantum dots derived from two-dimensional materials and their applications for catalysis and energy," *Chem. Soc. Rev.*, vol. 45, no. 8, pp. 2239–2262, 2016.

[172] N. S. Arul and V. D. Nithya, "Molybdenum disulfide quantum dots: synthesis and applications," *RSC Adv.*, vol. 6, no. 70, pp. 65670–65682, 2016.

[173] T. Wang *et al.*, "Enhanced electrocatalytic activity for hydrogen evolution reaction from self-assembled monodispersed molybdenum sulfide nanoparticles on an Au electrode," *Energy Environ. Sci.*, vol. 6, no. 2, pp. 625–633, 2013.

[174] D. Gopalakrishnan, D. Damien, and M. M. Shaijumon, "MoS_2 quantum dot-interspersed exfoliated MoS_2 nanosheets," *ACS Nano*, vol. 8, no. 5, pp. 5297–5303, 2014.

[175] H. Dong *et al.*, "Fluorescent MoS2 Quantum Dots: Ultrasonic Preparation, Up-Conversion and Down-Conversion Bioimaging, and Photodynamic Therapy," *ACS Appl. Mater. Interfaces*, vol. 8, no. 5, pp. 3107–3114, 2016.

[176] S. Pal, K. K. Tadi, P. M. Sudeep, S. Radhakrishnan, and T. N. Narayanan, "Temperature assisted shear exfoliation of layered crystals for the large-scale synthesis of catalytically active luminescent quantum dots," *Mater. Chem. Front.*, vol. 1, no. 2, pp. 319–325, 2017.

[177] S. Zhang, J. Li, and E. Wang, "Ultrafine transition metal dichalcogenide nanodots prepared by polyvinylpyrrolidone-assisted liquid phase exfoliation," *J. Mater. Chem. B*, vol. 5, no. 14, pp. 2609–2615, 2017.

[178] K. Zhou, Y. Zhang, Z. Xia, and W. Wei, "As-prepared MoS_2 quantum dot as a facile fluorescent probe for long-term tracing of live cells," *Nanotechnology*, vol. 27, no. 27, pp. 275101, 2016.

[179] X. Zhao, X. Ma, J. Sun, D. Li, and X. Yang, "Enhanced catalytic activities of surfactant-assisted exfoliated WS_2 nanodots for hydrogen evolution," *ACS Nano*, vol. 10, no. 2, pp. 2159–2166, 2016.

[180] C.-Y. Luan, S. Xie, C. Ma, S. Wang, Y. Kong, and M. Xu, "Elucidation of luminescent mechanisms of size-controllable $MoSe_2$ quantum dots," *Appl. Phys. Lett.*, vol. 111, no. 7, pp. 73105, 2017.

[181] J. Y. Wu, X. Y. Zhang, X. D. Ma, Y. P. Qiu, and T. Zhang, "High quantum-yield luminescent MoS_2 quantum dots with variable light emission created via direct ultrasonic exfoliation of MoS_2 nanosheets," *RSC Adv.*, vol. 5, no. 115, pp. 95178–95182, 2015.

[182] L. Lin, Y. Xu, S. Zhang, I. M. Ross, A. C. M. Ong, and D. A. Allwood, "Fabrication of luminescent monolayered tungsten dichalcogenides quantum dots with giant spin-valley coupling," *ACS Nano*, vol. 7, no. 9, pp. 8214–8223, 2013.

[183] M. O. Valappil, A. Anil, M. Shaijumon, V. K. Pillai, and S. Alwarappan, "A

single-step electrochemical synthesis of luminescent WS$_2$ quantum dots," *Chem. – A Eur. J.*, vol. 23, no. 38, pp. 9144–9148, 2017.

[184] H. Jin *et al.*, "Colloidal Single-Layer Quantum Dots with Lateral Confinement Effects on 2D Exciton," *J. Am. Chem. Soc.*, vol. 138, no. 40, pp. 13253–13259, 2016.

[185] S. Zhang, X. Jia, and E. Wang, "Facile synthesis of optical pH-sensitive molybdenum disulfide quantum dots," *Nanoscale*, vol. 8, no. 33, pp. 15152–15157, 2016.

[186] W. Dai *et al.*, "Tunable Fabrication of molybdenum disulfide quantum dots for intracellular microRNA detection and multiphoton bioimaging," *Small*, vol. 11, no. 33, pp. 4158–4164, 2015.

[187] B. L. Li, L. X. Chen, H. L. Zou, J. L. Lei, H. Q. Luo, and N. B. Li, "Electrochemically induced Fenton reaction of few-layer MoS$_2$ nanosheets: preparation of luminescent quantum dots via a transition of nanoporous morphology," *Nanoscale*, vol. 6, no. 16, pp. 9831–9838, 2014.

[188] Z. Chen *et al.*, "Fast preparation of ultrafine monolayered transition-metal dichalcogenide quantum dots using electrochemical shock for explosive detection," *Chem. Commun.*, vol. 52, no. 76, pp. 11442–11445, 2016.

[189] Y. Yan, C. Zhang, W. Gu, C. Ding, X. Li, and Y. Xian, "Facile synthesis of water-soluble WS$_2$ quantum dots for turn-on fluorescent measurement of lipoic acid," *J. Phys. Chem. C*, vol. 120, no. 22, pp. 12170–12177, 2016.

[190] R. M. Clark *et al.*, "Two-step synthesis of luminescent MoS_2–ZnS hybrid quantum dots," *Nanoscale*, vol. 7, no. 40, pp. 16763–16772, 2015.

[191] J. Ali, G. U. Siddiqui, K. H. Choi, Y. Jang, and K. Lee, "Fabrication of blue luminescent MoS_2 quantum dots by wet grinding assisted co-solvent sonication," *J. Lumin.*, vol. 169, pp. 342–347, 2016.

[192] X. Wang, Q. Wu, K. Jiang, C. Wang, and C. Zhang, "One-step synthesis of water-soluble and highly fluorescent MoS_2 quantum dots for detection of hydrogen peroxide and glucose," *Sensors Actuators B Chem.*, vol. 252, pp. 183–190, 2017.

[193] W. Sun *et al.*, "Size-controlled MoS_2 nanodots supported on reduced graphene oxide for hydrogen evolution reaction and sodium-ion batteries," *Nano Res.*, vol. 10, no. 7, pp. 2210–2222, 2017.

[194] H. Lin, C. Wang, J. Wu, Z. Xu, Y. Huang, and C. Zhang, "Colloidal synthesis of MoS_2 quantum dots: size-dependent tunable photoluminescence and bioimaging," *New J. Chem.*, vol. 39, no. 11, pp. 8492–8497, 2015.

[195] B. Li *et al.*, "Preparation of monolayer MoS_2 quantum dots using temporally shaped femtosecond laser ablation of bulk MoS_2 targets in water," *Sci. Rep.*, vol. 7, no. 1, p. 11182, 2017.

[196] S. P. Caigas *et al.*, "Origins of excitation-wavelength-dependent photoluminescence in WS_2 quantum dots," *Appl. Phys. Lett.*, vol. 112, no. 9, pp. 92106, 2018.

[197] H. D. Ha, D. J. Han, J. S. Choi, M. Park, and T. S. Seo, "dual role of blue luminescent MoS$_2$ quantum dots in fluorescence resonance energy transfer phenomenon," *Small*, vol. 10, no. 19, pp. 3858–3862, 2014.

[198] G. G. D. Han *et al.*, "Photoluminescent arrays of nanopatterned monolayer MoS$_2$," *Adv. Funct. Mater.*, vol. 27, no. 45, pp. 1703688, 2017.

[199] H. Abramczyk, *Introduction to laser spectroscopy*. Elsevier, 2005.

[200] J. R. Lakowicz, "Introduction to fluorescence BT-principles of fluorescence spectroscopy," J. R. Lakowicz, Ed. Boston, MA: Springer US, 1999, pp. 1–23.

[201] S. G. Gabriel, "On the change of refrangibility of light," *Philos. Trans. R. Soc. London*, vol. 142, pp. 463–562, 1852.

[202] X. Cao *et al.*, "Transition metal dichalcogenide quantum dots: Synthesis, photoluminescence and biological applications," *J. Mater. Chem. B*, vol. 6, no. 48, pp. 8011–8036, 2018.

[203] Z. X. Gan *et al.*, "Quantum confinement effects across two-dimensional planes in MoS$_2$ quantum dots," *Appl. Phys. Lett.*, vol. 106, no. 23, pp. 233113, 2015.

[204] D. Gopalakrishnan *et al.*, "Electrochemical synthesis of luminescent MoS$_2$ quantum dots," *Chem. Commun.*, vol. 51, no. 29, pp. 6293–6296, 2015.

[205] H. Jin *et al.*, "Effects of direct solvent-quantum dot interaction on the optical properties of colloidal monolayer WS$_2$ quantum dots," *Nano Lett.*, vol. 17, no. 12, pp. 7471–7477, 2017.

[206] Y. Wang and Y. Ni, "Molybdenum disulfide quantum dots as a photoluminescence sensing platform for 2,4,6-trinitrophenol detection," *Anal. Chem.*, vol. 86, no. 15, pp. 7463–7470, 2014.

[207] Y. Wang *et al.*, "Cryo-mediated exfoliation and fracturing of layered materials into 2D quantum dots," *Sci. Adv.*, vol. 3, no. 12, pp. e1701500, 2017.

[208] C. Zhu *et al.*, "Defect-laden $MoSe_2$ quantum dots made by turbulent shear mixing as enhanced electrocatalysts," *Small*, vol. 13, no. 27, pp. 1700565, 2017.

[209] C. Sweet, A. Pramanik, S. Jones, and P. C. Ray, "Two-photon fluorescent molybdenum disulfide dots for targeted prostate cancer imaging in the biological II window," *ACS Omega*, vol. 2, no. 5, pp. 1826–1835, 2017.

[210] M.-J. Kim *et al.*, "2H-WS_2 quantum dots produced by modulating the dimension and phase of 1T-nanosheets for antibody-free optical sensing of neurotransmitters," *ACS Appl. Mater. Interfaces*, vol. 9, no. 14, pp. 12316–12323, 2017.

[211] H. Zhu, H. Zhang, and Y. Xia, "Planar is better: monodisperse three-layered MoS_2 quantum dots as fluorescent reporters for 2,4,6-trinitrotoluene sensing in environmental water and luggage cases," *Anal. Chem.*, vol. 90, no. 6, pp. 3942–3949, 2018.

[212] Z. Luo *et al.*, "1-, 1.5-, and 2-µm fiber lasers Q-switched by a broadband few-layer MoS_2 saturable absorber," *J. Light. Technol.*, vol. 32, no. 24, pp. 4679–

4686, 2014.

[213] Y. Chen *et al.*, "Mechanically exfoliated black phosphorus as a new saturable absorber for both Q-switching and mode-locking laser operation," *Opt. Express*, vol. 23, no. 10, pp. 12823–12833, 2015.

[214] K. S. Suslick, N. C. Eddingsaas, D. J. Flannigan, S. D. Hopkins, and H. Xu, "Extreme conditions during multibubble cavitation: Sonoluminescence as a spectroscopic probe," *Ultrason. Sonochem.*, vol. 18, no. 4, pp. 842—846, 2011.

[215] V. Štengl and J. Henych, "Strongly luminescent monolayered MoS_2 prepared by effective ultrasound exfoliation," *Nanoscale*, vol. 5, no. 8, pp. 3387–3394, 2013.

[216] M. Hassan, E. Haque, K. R. Reddy, A. I. Minett, J. Chen, and V. G. Gomes, "Edge-enriched graphene quantum dots for enhanced photo-luminescence and supercapacitance," *Nanoscale*, vol. 6, no. 20, pp. 11988–11994, 2014.

[217] X. Li, H. Wang, Y. Shimizu, A. Pyatenko, K. Kawaguchi, and N. Koshizaki, "Preparation of carbon quantum dots with tunable photoluminescence by rapid laser passivation in ordinary organic solvents," *Chem. Commun.*, vol. 47, no. 3, pp. 932–934, 2011.

[218] A. M. Smith and S. Nie, "Chemical analysis and cellular imaging with quantum dots," *Analyst*, vol. 129, no. 8, pp. 672–677, 2004.

[219] X. L. Wu, J. Y. Fan, T. Qiu, X. Yang, G. G. Siu, and P. K. Chu, "Experimental evidence for the quantum confinement effect in 3C-SiC nanocrystallites," *Phys.*

Rev. Lett., vol. 94, no. 2, pp. 26102, 2005.

[220] Y. Y. Wang, X. Xiang, R. Yan, Y. Liu, and F. L. Jiang, "Förster resonance energy transfer from quantum dots to Rhodamine B as mediated by a cationic surfactant: a thermodynamic perspective," *J. Phys. Chem. C*, vol. 122, no. 2, pp. 1148–1157, 2018.

[221] G. E. Lecroy *et al.*, "Characteristic Excitation Wavelength Dependence of Fluorescence Emissions in Carbon 'quantum' Dots," *J. Phys. Chem. C*, vol. 121, no. 50, pp. 28180–28186, 2017.

[222] S. H. Jin, D. H. Kim, G. H. Jun, S. H. Hong, and S. Jeon, "Tuning the Photoluminescence of Graphene Quantum Dots through the Charge Transfer Effect of Functional Groups," *ACS Nano*, vol. 7, no. 2, pp. 1239–1245, 2013.

[223] W. Sukkabot, "Stokes shift and fine structure splitting in composition-tunable $Zn_xCd_{1-x}Se$ nanocrystals: Atomistic tight-binding theory," *Phys. B Condens. Matter*, vol. 506, pp. 192–197, 2017.

[224] J. Pérez-Conde, A. K. Bhattacharjee, M. Chamarro, P. Lavallard, V. D. Petrikov, and A. A. Lipovskii, "Photoluminescence Stokes shift and exciton fine structure in CdTe nanocrystals," *Phys. Rev. B - Condens. Matter Mater. Phys.*, vol. 64, no. 11, pp. 113303, 2001.

[225] D. C. Turner and L. Brand, "Quantitative estimation of protein binding site polarity. Fluorescence of N-arylaminonaphthalenesulfonates," *Biochemistry*, vol. 7, no. 10, pp. 3381–3390, 1968.

[226] S. Deng, L. Li, and Y. Zhang, "Strain modulated electronic, mechanical, and optical properties of the monolayer PdS_2, $PdSe_2$, and $PtSe_2$ for tunable devices," *ACS Appl. Nano Mater.*, vol. 1, no. 4, pp. 1932–1939, 2018.

[227] W. L. Chow *et al.*, "High mobility 2D palladium diselenide field-effect transistors with tunable ambipolar characteristics," *Adv. Mater.*, vol. 29, no. 21, pp. 1602969, 2017.

[228] J. Lin, S. Zuluaga, P. Yu, Z. Liu, S. T. Pantelides, and K. Suenaga, "Novel Pd_2Se_3 two-dimensional phase driven by interlayer fusion in layered $PdSe_2$," *Phys. Rev. Lett.*, vol. 119, no. 1, pp. 16101, 2017.

[229] A. Hamidani, B. Bennecer, and K. Zanat, "Structural and electronic properties of the pseudo-binary compounds PdX_2 (X=P, S and Se)," *J. Phys. Chem. Solids*, vol. 71, no. 1, pp. 42–46, 2010.

[230] A. A. Audi and P. M. A. Sherwood, "X-ray photoelectron spectroscopic studies of sulfates and bisulfates interpreted by Xα and band structure calculations," *Surf. Interface Anal.*, vol. 29, no. 4, pp. 265–275, 2000.

[231] G. Dodero *et al.*, "l-Cysteine chemisorption on gold: an XPS and STM study," *Colloids Surfaces A Physicochem. Eng. Asp.*, vol. 175, no. 1–2, pp. 121–128, 2000.

[232] S. Xu, D. Li, and P. Wu, "One-pot, facile, and versatile synthesis of monolayer MoS_2/WS_2 quantum dots as bioimaging probes and efficient electrocatalysts for hydrogen evolution reaction," *Adv. Funct. Mater.*, vol. 25, no. 7, pp. 1127–

1136, 2015.

[233] M. Hassan, E. Haque, K. R. Reddy, A. I. Minett, J. Chen, and V. G. Gomes, "Edge-enriched graphene quantum dots for enhanced photo-luminescence and supercapacitance," *Nanoscale*, vol. 6, pp. 11988–11994, 2014.

[234] W. Sukkabot, "Stokes shift and fine structure splitting in composition-tunable $Zn_xCd_{1-x}Se$ nanocrystals: Atomistic tight-binding theory," *Phys. B Condens. Matter*, vol. 506, pp. 192–197, 2017.

[235] Y. M. Long *et al.*, "Shifting and non-shifting fluorescence emitted by carbon nanodots," *J. Mater. Chem.*, vol. 22, no. 13, pp. 5917–5920, 2012.

[236] Y. Zhang *et al.*, "Multicolour nitrogen-doped carbon dots: tunable photoluminescence and sandwich fluorescent glass-based light-emitting diodes," *Nanoscale*, vol. 9, no. 45, pp. 17849–17858, 2017.